Arches, nonlinear?

Investigating the geometrically nonlinear behaviour of arches in 2D

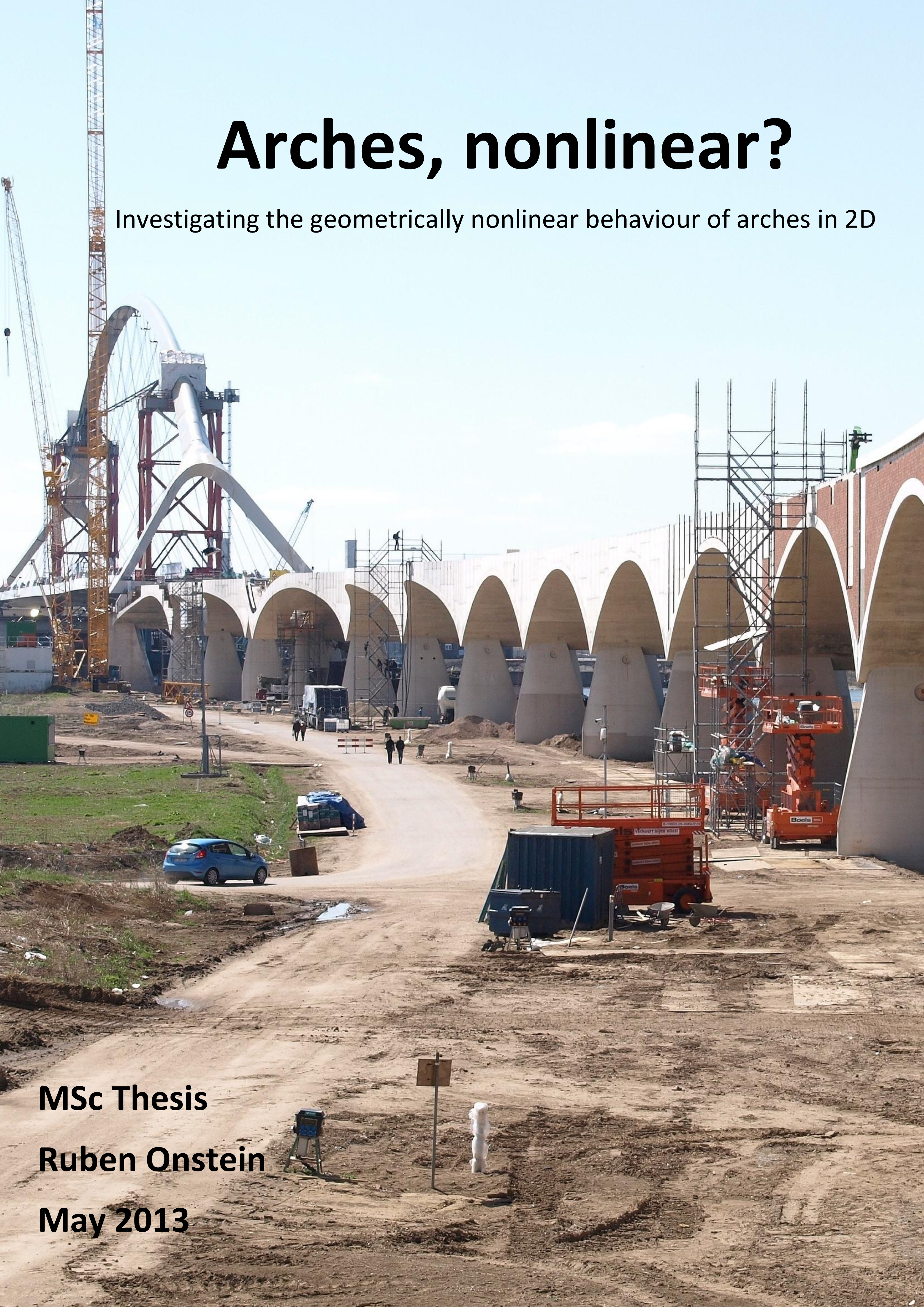

MSc Thesis

Ruben Onstein

May 2013

Cover illustration: Nijmegen City bridge (source: BAM Infraconsult bv)

Arches, nonlinear?

Investigating the geometrically nonlinear behaviour of arches in 2D.

Thesis submitted to Delft University of Technology for the degree of Master of Science.

May 2013

Author:
ing. R.C.P. (Ruben) Onstein
E-mail: rubenonstein@gmail.com

Delft University of Technology

Faculty:	Civil Engineering and Geosciences
Department:	Structural Engineering
Section:	Concrete Structures

Master's thesis committee

Chairman

Prof.dr.ir. J.G.Rots	TU Delft – Structural Mechanics

Committee members

Dr.ir. P.C.J. Hoogenboom	TU Delft – Structural Mechanics
Dr.ir. M.A.N. Hendriks	TU Delft – Structural Mechanics
Dr.ir. C. van der Veen	TU Delft – Concrete Structures
T. Wolvekamp MSc	BAM Infraconsult bv

Secretary

Ir. L.J.M. Houben	TU Delft – Road and railway engineering

Contents – general overview

Part 0 – Extended Summary

Part 1 – Introduction and Orientation

Part 2 – Single arch analysis

Part 3 – Multiple arch analysis

Part 4 – Introduction to physical nonlinearity and 3D effects

Acknowledgement

This report comprises the results of my Master's Thesis research at Delft University of Technology. It is a theoretical answer to the practical design question, considering the magnification of bending moments due to second order effects in arch bridges. This topic provided the opportunity to develop more insight into structural behavior of arches and to develop the necessary skills when using software in engineering.

I would like to thank my graduation committee, Jan Rots, Cor van der Veen, Pierre Hoogenboom and Max Hendriks for their guidance and feedback while discussing my ideas and results

Furthermore, I would like to thank the colleagues at BAM Infraconsult for giving me the opportunity to do the research, for their extensive support and their enthousiasm.

Ruben Onstein

Gouda, May 2013

Part 0: Extended summary

Contents – Part 0: Extended Summary

1. Introduction to Part 0

1.1 Background

The city of Nijmegen is located at the banks of the river Waal. Heavy traffic on the old Waal bridge (arch bridge, completed in 1936) and the urban road network requires a second river crossing. Based on the architectural look of the bridge, the design competition was won by the consortium. A succession of concrete arches with masonry cladding on the parapets were chosen for the approach bridge, to unite the new bridge with the shape of the existing bridge and with the cities Roman history. Concrete arches are applied in many bridges. Nevertheless, piers supporting the arches and robust end supports to confine these arches is a unique solution. When analysing other concrete arch bridges, either the arches are confined directly by the foundation or tensile ties are applied.

The structural verification of the succession of the flexibly supported, slender arches, raised questions on the nonlinear structural behaviour. The axial forces reach values up to 35% of the Euler buckling load and the flexibility of the support leads to high bending moments. In the structural design, the bending moment magnification due to geometrically nonlinear behaviour is based on the design of columns. The well-known engineering formula for geometrically nonlinear behaviour $n/(n-1)$ is combined with stability analysis and structural analysis. As the ratio of the Euler buckling load and the design load is $n \approx 3$, the engineering formula yields a magnification factor of 1.5 on the bending moments to account for the geometrically nonlinear behaviour. Using this factor, a nonlinear analysis can be left out, which saves time in the design process, but it ignores the true geometrical nonlinearity, the equilibrium of the deformed structure.

Figure 1: Side view to Northern approach bridge

1.2 Thesis outline

The main objective of the thesis is to provide insight in the theory and analysis of the geometrically nonlinear behaviour of arched structures. The objective splits into two parts. On one hand there is the checking of the design assumption, on the other hand it should guide future design of similar structures.

The research is carried out within the framework of the Nijmegen city bridge. Loads, soil properties and geometry of the city bridge design are heavily used as backbone of the practical part of the investigation.

1.2.1 Research questions

The scope of the investigation is determined by the research questions:

- *What are the theoretical backgrounds of the geometrically nonlinear behaviour of arched structures?*

- *How do the internal forces change, when geometrically nonlinear behaviour is accounted for in the analysis of arched structures?*

- *Is there a link between Euler buckling and geometrically nonlinear behaviour in arched structures?*

- *How to deal with the geometrically nonlinear behaviour of arched structures in practice?*

1.3 Parts

The research is carried out and reported in four separate parts, upholding their individual characters and representing the chronology of the research process. Together, the parts provide the answers to the research questions.

1.3.1 Part 1 – Literature and buckling

In the first part the orientation phase of the investigation is reported. Obviously, the approach bridge design has been studied, but the main part of the orientation phase consisted of literature study, in which buckling stability was considered. Since in engineering, stability and geometrical nonlinearity are closely related via the $n/(n-1)$ factor, studying buckling seemed a good starting point. The theory was extended with a sensitivity analysis to investigate the influence of the different parameters to the Euler buckling capacity of arches.

1.3.2 Part 2 – Single arch analysis

As buckling theory did not provide answers to the geometrically nonlinear question in arch analysis, structural behaviour of arches was studied. The differential equation for arch structures provided insight into the linear and nonlinear analysis. In the derivation of the differential equation the effect of the deformations on the arch shape is neglected $(w \ll z)$ and the thrust is assumed to be constant $(\Delta H = 0)$, leading to the linear behaviour.

$$EI \cdot \frac{d^4 w}{dx^4} + H \cdot \frac{d^2 z}{dx^2} = q(x)$$

The differential equation including the nonlinear effect reads:

$$EI \cdot \frac{d^4 w}{dx^4} + (H + \Delta H) \cdot \frac{d^2 (z + w)}{dx^2} = q(x)$$

These differential equations are analysed for different loads, different support conditions and geometrical imperfections are included. However, originally, the differential equations described models for arches with rigid supports in which only vertical deformations are considered. Horizontal deformations u are not incorporated in the differential equation. Horizontal support translation is added in the determination of the horizontal thrust:

$$u = \int_0^l \frac{dz}{dx} \cdot \frac{dw}{dx} dx = \frac{Hl}{EA} + \frac{H}{k_{support}}$$

For low support stiffness, the model does not lead to reliable results. All results are compared with finite element analyses. Additionally, the Euler buckling loads are determined in the finite element models and the corresponding magnification factors are compared to the geometrically nonlinear analyses. The second part finishes with an investigation of different arch geometries. The geometrically nonlinear analysis is performed for different spans and different rise to span factors.

1.3.3 Part 3 – Multiple arches

A succession of arches is fundamentally different from a single arch in the way the confinement is secured. In a single arch the horizontal thrust is exited after arch deformation. In a succession, arches are mutually supported in horizontal direction by adjacent arches. Horizontal translation of intermediate spans are small compared to single arches with equivalent support stiffness, although towards the end spans the degree of confinement decreases.

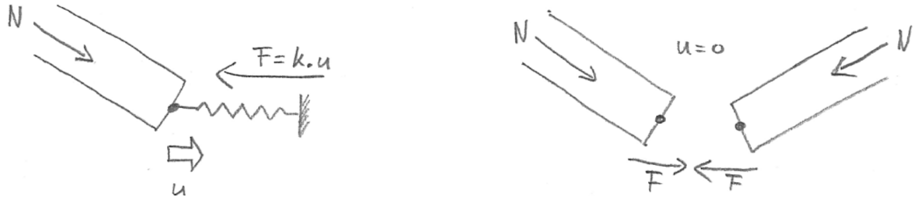

Figure 2: Principal difference in confinement, single arch (l) and multiple arches (r)

In the multiple arch models, first the influence of the adjacent spans is investigated. The supports are modelled by their spring stiffness. In the following investigation, the arch models are extended with the actual substructure, to determine the effect of the support flexibility more accurate.

1.3.4 Part 4 – Further investigation

Physically nonlinear behaviour and the transverse load distribution could not be investigated in this thesis thoroughly due to time constraints. However, a brief introduction for future research is provided in this part. The influence of cracking at the supports is investigated by reducing the Young's modulus of the material. Fictitious Young's moduli are derived with M-N-κ diagrams.

The transverse load distribution can only be investigated with a three dimensional model. Point supports or line supports and transverse prestressing determine the transverse load distribution. A single arch is modelled and the effect of the support condition and the prestress is displayed.

The *appendices* are added to this report on cd-rom.

2. Results and Conclusions

2.1 Single arch

The theoretical background of the engineering formula $n/(n-1)$ shows that the formula provides the exact magnification in only few cases. Nevertheless, for columns it is a good approximation. In arches there are two fundamental differences. Often the lowest buckling load corresponds to a buckling mode that is not affine with the deformations. Furthermore, the external loading that causes the internal normal forces is different for arches, when compared to columns.

Comparing the differential equations for linear and geometrically nonlinear analysis of arches, an imaginary second order load is represented by the term $H \cdot w''$. When judging analysis results, this second derivative of the deformations can be visualised by $w'' = \kappa = -M/EI$. In Figure 3, this is displayed. Easily can be seen that the bending moment magnification factor is not constant along the arch, as the bending moment distributions have different shapes.

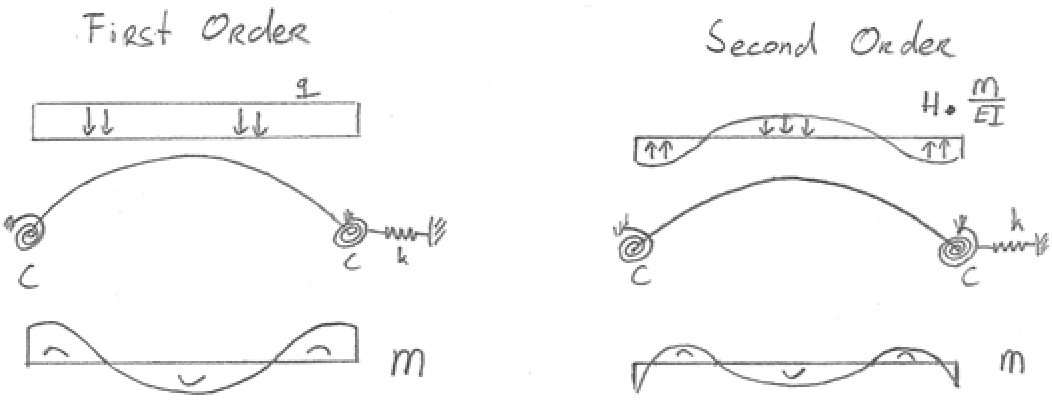

Figure 3: Visualisation second order load

Checking the bending moment magnification computed via geometrically nonlinear analysis with the magnification factor provided by stability analysis, the affine buckling mode results in a better approximation compared to the non-affine mode, but the approximation remains poor, especially for lower stiffnesses.

Additionally, in second order theory, the influence of geometrical imperfections should be taken into account. An amplitude for the imperfection is provided and it should be applied to the lowest horizontal and lowest vertical buckling modes. It is allowed to model the buckling modes by sine waves. The geometrical imperfection leads to higher bending moments in linear analysis, due to the deviation with respect to the thrust line and to slightly higher bending moment magnification.

Although different internal forces are found in linear and nonlinear analysis with and without geometrical imperfections, the bending moments are highly sensitive to the bending stiffness EI. The linear perfect model versus the nonlinear imperfect model will vary by a factor 1.2 to 1.8, while the bending moments for the lowest and highest realistic Young's modulus vary a factor 3.

2.2 Multiple arches

In structures consisting of a succession of flexible supported arches, the end spans behaves like the flexible supported single arch, due to the moderate confinement. The intermediate spans resemble the rigid supported single arch, as the displacement at the supports is low. However, the shape of the bending moment distribution is similar, the values are different. In arched structures, a small displacement at the support cannot be neglected.

The end spans will yield the highest bending moments. Due to the low confinement, bending moments are high in linear analysis. Moreover, a large share of the horizontal thrust H is excited in the end span and deformations are high, leading to high second order bending moments.

For a succession of arches it is hard to find an affine buckling mode, since partial buckling, buckling of a single or a small number of arches, is generally governing. Application of the engineering formula $n/(n-1)$ is misleading due to the large number of buckling modes and the previously described poor agreement with the true nonlinear behaviour.

Two geometrical imperfections are investigated by manually drawing the imperfect shape. The anti-symmetrical (two half sine waves) imperfection is combined with a tandem axle loading at $0.25\ L$ and the symmetrical (three half sine waves) imperfection is combined with the tandem axle loading at mid span. The second combination causes the highest bending moments and the highest bending moment magnification.

3. Recommendations for design

The imaginary second order loading, as a function of the reverse bending moment distribution, provides the better tool to judge the geometrically nonlinear behaviour of arches. Other than in column design, there is only a poor relation with the Euler buckling capacity in nonlinear arch behaviour. Along the arch, different magnification factors will be found, as first order and second order bending moments have different distributions. With the second order load supposition, these different distributions for first order and second order bending moments can be explained.

However, structural behaviour of arches relies heavily on stiffnesses. Bending stiffness, axial stiffness, the stiffness provided by the substructure and surrounding soil and the arch geometry together determine the deformed shape and the internal forces. Higher bending stiffness will result in higher bending moments, while higher translational support stiffness lead to higher normal forces and lower bending moments.
For higher stiffness in general, deformations will be smaller and the geometrically nonlinear effect will be smaller too.

Nevertheless, the bending stiffness and the horizontal confinement are the decisive parameters in arch design, even geometrical nonlinearity has less crucial influence. The fictitious Young's modulus that can be taken into account can vary largely, since the fictitious uncracked stiffness can reach values of $E_f > 40{,}000\ \mathrm{N/mm^2}$ and the cracked cross-section at the ultimate bending moment capacity and including creep effects can result in $E_f \approx 5{,}000\ \mathrm{N/mm^2}$. It is advisable to investigate the fictitious Young's modulus in detail during design and to apply different fictitious stiffnesses in the cracked and uncracked zones of the arch. Although not investigated in this thesis, a more extensive soil stiffness analysis is worth considering in case higher soil stiffness is to be expected.

In geometrically nonlinear analysis, an imperfection should be modelled to incorporate the effects of execution tolerances and material non-homogeneity. The imperfection results in high bending moments due to the high normal forces. For these imperfections, the buckling modes should be adapted. It is allowed to model the imperfection by sine waves. When modelling the imperfection manually by adapting the nodal coordinates, its effect is accounted for in linear and nonlinear analysis and the engineer keeps control over the model. In Scia Engineer it is not possible to include an imperfection based on a buckling mode in linear analysis.

When including the imperfection manually, there are two options. A geometrically nonlinear analysis or an approximation via linear analysis and the magnification factor via the affine buckling mode. In both approaches, the number of load cases should be reduced, as for both nonlinear and stability analysis an analysis run is required for each load combination. The stability analysis is little faster, but less accurate.

When using Scia Engineer for nonlinear analysis, solver settings are important. The program is equipped with several solvers, of which the "Timoshenko" solver is not capable of handling variations in normal forces during nonlinear analysis, which should not be used in nonlinear arch analysis. Furthermore, the applied elements are straight, even when selecting curved shapes during the geometry input, requiring a small mesh size when evaluating arches. So when analysing arches, it is recommended to investigate stiffnesses.

Part 1: Introduction and Orientation

Contents - part 1: Introduction and Orientation

4. List of symbols

A	Area
a	Amplitude
b	Width
C	Rotational spring stiffness
c	Concrete
d	Design value
$d/dx,'$	Derivative
E	Young's modulus, Exposure (all loading)
E_f	Fictitious Young's modulus
F	Point load
f	Rise
f_{cd}	Concrete compressive strength
f_{yd}	Yield strength reinforcement
G	Permanent load
H	Horizontal thrust
h	Horizontal thrust – second order effect only, height
I	Moment of inertia
k	Translational spring stiffness
L, l	Span
M	Bending moment
m	Bending moment – second order effect only
m	Mean value
N	Normal force
n	Critical load factor: q_E/q
P	Distributed (area) load, prestress
Q	Variable load
q	Distributed (line) load
q_E	Euler buckling load
R	Radius, resistance
s	Arch length, steel
T	Temperature
t	thickness
u	Deformation in x-direction
V	Shear force
W, w	Deformation in z-direction
x, y, z	Axis system
z	Arch axis
α	Angle, factor
γ	Partial safety factor
Δ	(small) difference
ε	Strain
θ	Angle
κ	Curvature
ν	Poisson factor
ρ	Reinforcement ratio
φ	Rotation
ψ	Load combination factor

5. Design City Bridge Nijmegen

Creating a new river crossing by means of a bridge has always a huge impact on the urban development. Therefore most cities will opt for a so called 'landmark' in which the bridge not only will meet technical standards. It will fulfill an important step in the urban planning of the surrounding area. The Nijmegen City Bridge is no exception. Ambitions are high and the municipality laid down a number of benchmarks, which should guide the design of the bridge.

- Visibility and amenity of the rivers landscape
- Cohesion in the current image and the future image of the urban area
- Artwork which represents the state of the art in architectural and technical potential
- Residential quality, both on top and under the bridge

For the main span, a steel mono-arch bow string is applied. A series of concrete arches shape the approach bridges. Visibility of the landscape is secured by the combination of a span of 42.5 m and only two piers at the grid lines. The arched shapes, together with the masonry lining on the parapets, refer to the city's Roman history and to the other traffic bridge that crosses the river.

In Figure 4 the architectural design is shown.

Figure 4: Architectural Design [VisAB]

5.1.1 Approach bridge

The characteristic dimensions of the arched structure are:

Span:	$L = 42.5\text{ m}$	Thickness at crown:	$t_c = 500\text{ mm}$
Width:	$b = 25\text{ m}$	Thickness at heel:	$t_h = 1{,}500\text{ mm}$
Radius:	$R = 42.14\text{ m}$	$R/t_c \approx 84$	
Rise:	$f = 5.75\text{ m}$	$f/l = 0.135$	

Figure 5: Plan view of the bridge

Figure 6: Side view of the bridge [VisAR]

Both the Northern ($703\ \mathrm{m}$) and Southern ($275\ \mathrm{m}$) approach bridges (Figure 5 and Figure 6) are so called integral structures, in which there are no expansion joints and all piers and arches are monolithically connected. Only at the interface between the approach bridges and the main span, expansion joints are applied. It is advantageous only using two expansion joints, since these joints have to be replaced several times during the lifetime of a bridge. However, horizontal confinement is essential for membrane action. The main piers at the river banks and the abutments located at the dikes, should provide this confinement. Not using expansion joints and confining the structure, will lead to high stresses due to imposed deformation, caused by shrinkage, creep and temperature differences. Analysis showed that part of the imposed deformation also causes vertical deformation. The residual part of the imposed deformation is restrained and leads to stresses.

The arches are reinforced with mild steel only, no prestress is applied in the longitudinal direction. In transverse direction prestress is applied in the integrated cross beams to span the pier to pier distance and to compensate the high tensile stress as a result of the concentrated shape of the supports. The cross beams are integrated in the design by thickening the concrete arches at the supports to 1,500 mm.

The spandrel volume is filled with foamed concrete. On top of the fill, the pavement consisting of mixed aggregates and asphalt is placed. The bridge accommodates five traffic lanes and a separate area for pedestrians and cyclists, requiring together a width of $25\ \mathrm{m}$.

The horizontal road alignment of the approach bridge consists of two curved parts with radii of $900\ \mathrm{m}$ and $2000\ \mathrm{m}$. To minimize the disturbance in the flow profile of the river, the piers are placed parallel to the direction of the water flow. The skew angle is accounted for in the arch geometry. Since the skew angle varies between $77°$ and $90°$, there is no need to account for the torsion effects in the analysis (threshold value: $70°$). The bridge is founded on cast-in-situ piles.

6. Design of the approach bridge

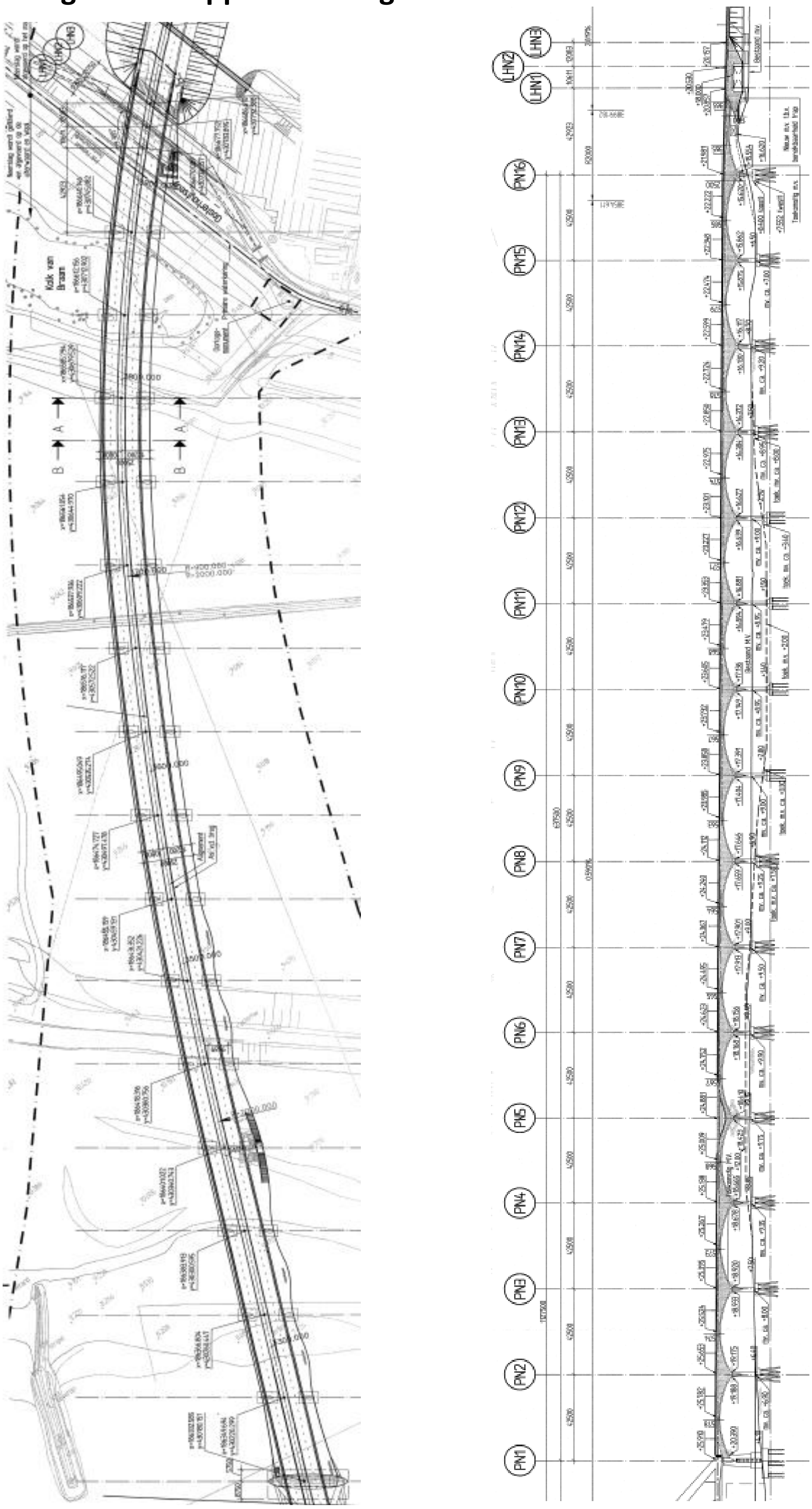

Figure 7: Top view (left) and side view (right) of approach bridge North

7. Loads

In the design of the approach bridge, a large amount of load cases are analysed. The same loads should be applied in this investigation to have a good correspondence. Nevertheless, some simplifications are applied to minimize the load cases and combinations, to have a workable research problem. The remaining load set contains the characteristic loads that are exerted on the bridge, such as permanent loads and traffic load. Exceptional load cases, e.g. maintenance trucks are not considered.

The second reason to reduce the load combinations is the fact that in nonlinear analysis the superposition principle is not valid. This has a major impact on the analysis methods. In linear analysis all load cases are analysed separately and to obtain the results, the force distributions of each load case are summed according to the defined load combinations. In nonlinear analysis each load combination has to be dealt with solely. Next to that, nonlinear analysis requires more time, since load is applied incrementally and solutions are calculated iteratively for each load increment. For nonlinear analysis, the number of load combinations should therefore be reduced to a small number of governing combinations, in order to have a solvable problem in terms of required time and capacity of the computer.

The shown loads are based on the design of BAM Infraconsult bv. All background information and extended calculation can be found in the document: *"DO - Berekeningsrapport aanbrug Noord PN1 t/m PN16", Document ID: "SN-2.1.1.4-C-TM-RA-2238".* In this report only an overview is given. All tables and figures in this chapter are copied out of this document.

7.1 Self-weight and dead loads

Loading due to self-weight is calculated by the structural analysis software, based on the material densities. For the analytical model, the self-weight is determined via the cross-section $(0.5 \cdot 25\ m^2)$, leading to a line load of $312.5\ kN/m^1$.

Reinforced concrete:	$\gamma_G = 25\ \mathrm{kN/m^3}$
Plain concrete	$\gamma_G = 24\ \mathrm{kN/m^3}$
Steel	$\gamma_G = 78.5\ \mathrm{kN/m^3}$

7.1.1 Pavement

The road pavement consists of a base layer (mixed aggregates, $\gamma_G = 19\ \mathrm{kN/m^3}$, variable thickness) and a $135\ \mathrm{mm}$ asphalt layer ($\gamma_G = 24\ \mathrm{kN/m^3}$). Due to the variable thickness of the base layer, the load varies over the width of the bridge.

2D model: line load $233\ \mathrm{kN/m}$

3D model:

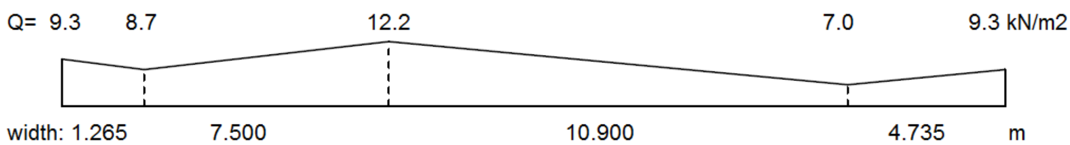

7.1.2 Barrier

Barriers will be placed to separate the traffic from the footpath (east side) and the inspection path (west side). The weight of the barrier is $7\ \mathrm{kN/m}$. On top of the barrier a windscreen will be placed, ($2\ \mathrm{kN/m}$). Leading to two line loads $q_G = 9\ \mathrm{kN/m}$.

7.1.3 Parapets

A concrete wall, finished with masonry, cap stones and a handrail comprise the parapets. The concrete wall has a thickness of $300\ \mathrm{mm}$. For the masonry ($t = 50\ \mathrm{mm}$) a weight $\gamma_G = 19\ \mathrm{kN/m^3}$ is assumed. The cap stones and the handrail weigh $2.97\ \mathrm{kN/m}$. Due to the variable height of the parapets, the loading is non-uniform. The concrete wall has a height of $1.166\ \mathrm{m}$ with respect to the top level of the pavement.

Table 1: Dead weight (single) parapet

x [m]	h [m]	h_{extra} [m]	h_{tot} [m]	q [kN/m]
0.0000	5.457	1.166	6.623	**58.9**
2.1250	4.511	1.166	5.677	**50.9**
4.2500	3.561	1.166	4.727	**42.9**
6.3750	2.698	1.166	3.864	**35.6**
8.5000	1.965	1.166	3.131	**29.4**
10.6250	1.353	1.166	2.519	**24.3**

x [m]	h [m]	h_{extra} [m]	h_{tot} [m]	q [kN/m]
12.7500	0.861	1.166	2.027	**20.1**
14.8750	0.482	1.166	1.648	**16.9**
17.0000	0.214	1.166	1.380	**14.6**
19.1250	0.054	1.166	1.220	**13.3**
21.2500	0.000	1.166	1.166	**12.8**

7.1.4 Pipes

Ten pipes are required for the functioning of the bridge, each weighing $1.25\ kN/m$. In the 2D model, a line load of $12.5\ \mathrm{kN/m}$ is applied. In the 3D model, the load is divided over two lines, one line $8.75\ \mathrm{kN/m}$ (east side) and the other line $3.75\ \mathrm{kN/m}$ (west side).

7.1.5 Foamed concrete

On top of the arches, there is a spandrel fill of foamed concrete. The chosen material has a density of $450\ \mathrm{kg/m^3}$. For the upper $0.5\ \mathrm{m}$, a mixture with a higher density of $1{,}000\ \mathrm{kg/m^3}$ is applied. Due to the porous micro structure, water saturation of the spandrel fill was investigated. The permeability of the foamed concrete appeared to be sufficiently low to neglect this phenomenon.

Table 2: Dead weight foamed concrete

x [m]	h [m]	3D model p [kN/m2]	2D model q [kN/m]
0.0000	5.457	**27.8**	**694.6**
2.1250	4.511	**23.1**	**576.4**
4.2500	3.561	**18.3**	**457.6**
6.3750	2.698	**14.0**	**349.8**
8.5000	1.965	**10.3**	**258.1**
10.6250	1.353	**7.3**	**181.6**

x [m]	h [m]	3D model p [kN/m2]	2D model q [kN/m]
12.7500	0.861	**4.8**	**120.1**
14.8750	0.482	**2.9**	**72.3**
17.0000	0.214	**1.3**	**32.1**
19.1250	0.054	**0.3**	**8.1**
21.2500	0.000	**0.0**	**0.0**

7.2 Shrinkage and creep

Due to shrinkage, additional stresses occur in the arch structure. Autogenous and drying shrinkage are taken into account via a fictitious temperature load. Calculations are based on NEN-EN 1992-1-1:2005 Appendix B1.

Table 3: creep factor $\varphi(t, t_0)$ and shrinkage ε_{cs}

C35/45	RH 80%	t: 36500 days, t_0: 28 days, t_s: 3 days					
h	b	h_0	φ_0	**$\varphi(t,t_0)$**	ε_{ca}	ε_{cd}	**ε_{cs}**
[m]	[m]	[m]	[-]	**[-]**	[-]	[-]	**[-]**
0.5	25	0.46	1.575	**1.558**	0.000063	0.000172	**0.000238**
1	25	0.962	1.669	**1.656**	0.000063	0.000176	**0.000234**

7.2.1 Shrinkage and creep combined

Since drying shrinkage is a slow process, its effects may be reduced due to creep. With a creep factor of $\varphi = 1.558$, the reduction factor is $\frac{1-e^{\varphi}}{\varphi} = 0.51$.

$\varepsilon'_{cd;\infty} = 0.51 \cdot 17.2 \cdot 10^{-5} = 8.8 \cdot 10^{-5}$
$\varepsilon'_{ca;\infty} = 6.3 \cdot 10^{-5}$

The fictitious temperature load is in case $h = 0.5$ m:

$$\Delta T = \frac{\varepsilon'_{cs;\infty}}{\alpha} = \frac{-(8.8 + 6.3) \cdot 10^{-5}}{10 \cdot 10^{-6}} = -15.1 \text{ °C}$$

Parts of the structure with a higher thickness are less sensitive to drying shrinkage. For $h = 1.0$ m the fictitious load is $\Delta T = -14.9$ °C. To apply the fictitious temperature load for $h = 0.5$ m to the entire structure is thus a conservative approach.

7.3 Prestressing load

The integrated crossbeams are prestressed to accommodate for the high tensile stresses which occur due to the concentrated supports in transverse direction. The positioning of the prestress leads to an upward load in the middle third (8.33 m) of the span.

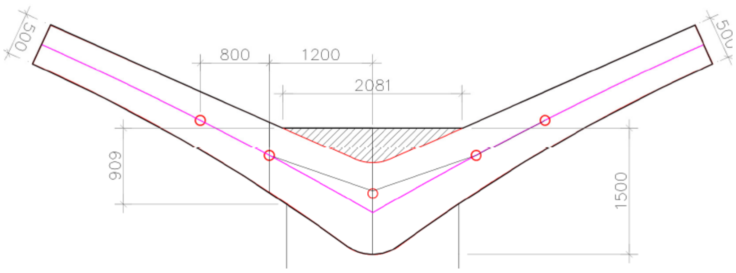

Figure 8: Cross-section prestressed integrated beam

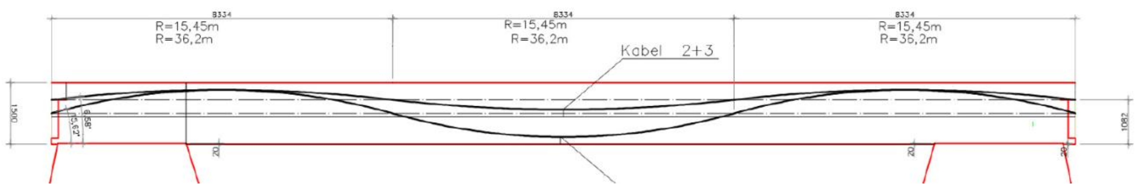

Figure 9: Side view prestress cables integrated beam

The loads due to prestressing are displayed in Table 4. Only the results are shown. Designing the prestressing system is not part of the research.

Table 4: Prestress loads

	Middle cable	Side cable
Distributed upward	$365.7\ \mathrm{kN/m^1}$	$156.1\ \mathrm{kN/m^1}$
Distributed downward	$365.7\ \mathrm{kN/m^1}$	$156.1\ \mathrm{kN/m^1}$
Concentrated load anchor vertical	$1522\ \mathrm{kN}$	$647\ \mathrm{kN}$
Concentrated load anchor horizontal	$5650\ \mathrm{kN}$	$5650\ \mathrm{kN}$

However, the prestress loads on the cross beams can only be modelled in three-dimensional models. In two-dimensional models the transverse direction is neglected.

7.4 Temperature load

Loading due to temperature differences can be divided daily and annual fluctuations. According to Eurocode EN 1991-1-5, temperature differences can be split up in a mean part (ΔT_N), a gradient (ΔT_M) and a nonlinear part (eigen temperatures, ΔT_E).

7.4.1 Annual temperature differences

The annual temperature variation causes expansion or contraction. No gradient or nonlinear temperature load occur, since it is a slow process. Note that the integral character of the structure causes bending moments when expanding or contracting due to compatibility conditions (e.g. restrained rotations).

The prescribed values, which are based on a design lifetime of 50 years ($p = 0.02$), are recalculated for the design lifetime of 100 years ($p = 0.01$) and bridge type.
$T_{e,max} = +33°\mathrm{C}$
$T_{e,min} = -19.5°\mathrm{C}$
$T_0 = 10°\mathrm{C}$

Annual temperature difference, which should be taken into account:
$\Delta T_{N+} = +23°\mathrm{C}$
$\Delta T_{N-} = -29.5°\mathrm{C}$

7.4.2 Daily temperature differences

Daily temperature differences lead to expansion or contraction and a gradient (linear approach). Two load cases should be considered, heating (solar radiation) and cooling (release of heat via radiation) of the bridge deck. The prescribed value may be reduced with a factor k_{sur}, which is equal to 0.6 for the heating of the bridge deck. Both heating and cooling are defined as temperature variation at the top edge of the bridge, with a linear decrease to the bottom edge (intrados of the arch).

$\Delta T_{M\ heat} = +9°\mathrm{C}$
$\Delta T_{M\ cooling} = -8°\mathrm{C}$

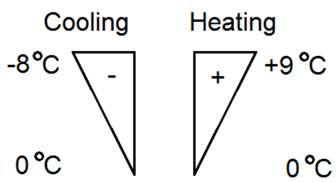

Figure 10: Daily temperature

7.4.3 Nonlinear temperature distribution

Nonlinear temperature load causes eigen stresses, next to the previously described linear approach. Since the fill (minimum $335\ \mathrm{mm}$) insulates the top edge (extrados) of the arch, the nonlinear part is neglected. Since it does not lead to deformations of the structure, it has no influence on the bending moment magnification.

7.4.4 Combining temperature loads

The loading should be combined in two ways:

$\Delta T_M + 0.35\,\Delta T_N$ and $0.75\,\Delta T_M + \Delta T_N$

Since the annual temperature load is much higher, only the second combination is applied. Leading to combination factors of $0.75 \cdot 1.5 = 1.125$ and $0.75 \cdot 0.9 = 0.68$.

7.5 Traffic load

Eurocode EN 1992-2 defines four load models, which should be taken into account in design. Load model 2 is used for design checks of local phenomena and is omitted in the research. Load model 3 is not applicable in the project. Arches are sensitive to asymmetrical loading and traffic load should be investigated on half spans too.

7.5.1 Load model 1 (UDL & Tandem System)

In this model, the bridges topside is divided in theoretical lanes, loaded with a uniformly distributed load and tandem axle systems (Table 5). The bridge has a width of $17.8\ \mathrm{m}$ in between the barriers, leading to 5 theoretical lanes ($3\ \mathrm{m}$ wide) and a remainder of $2.8\ \mathrm{m}$. The lanes should be applied in the most unfavourable configurations for the bridge. Lane 1 is placed in three positions, the middle, maximum East and maximum West. There is a magnification factor α_k which might be applied when higher loads are to be expected. The city council decided that on all loads in LM1, $\alpha_k = 1.0$.

Table 5: Traffic loads in Load Model 1

Lane	Tandem axle system	Uniformly Distributed Load
1	$Q_{1k} = 300\ \mathrm{kN/axle}$	$p_{1k} = 9\ \ \mathrm{kN/m^2}$
2	$Q_{2k} = 200\ \mathrm{kN/axle}$	$p_{2k} = 2.5\ \mathrm{kN/m^2}$
3	$Q_{3k} = 100\ \mathrm{kN/axle}$	$p_{3k} = 2.5\ \mathrm{kN/m^2}$
4, 5 & remaining	-	$p_{ik} = 2.5\ \mathrm{kN/m^2}$

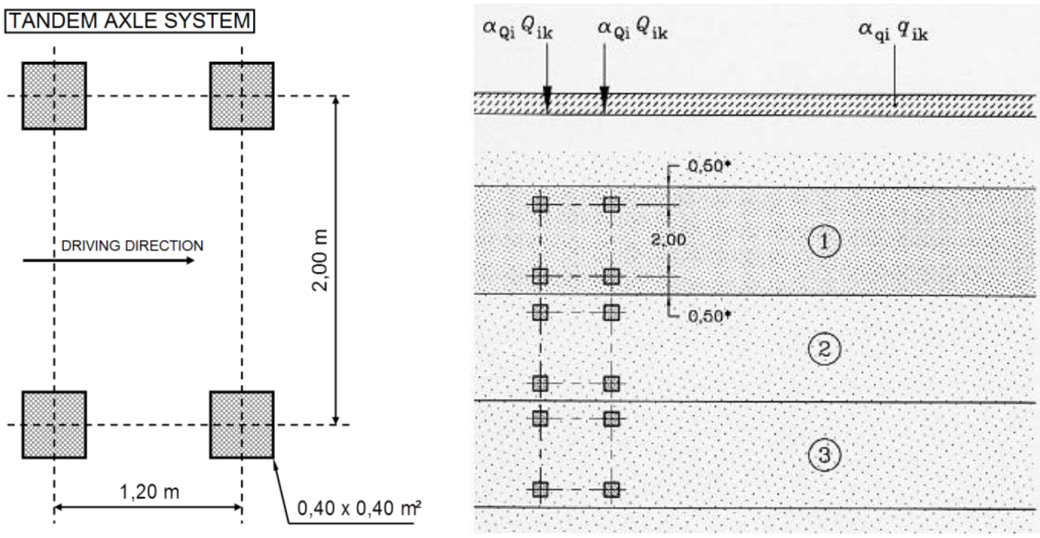

Figure 11: Geometry tandem axle load and distribution on multiple lanes (LM1)

The foamed concrete fill spreads the concentrated wheel loads, Figure 12. The corresponding angle is assumed to be $60°$. In the concrete arch, spreading of $45°$ is assumed. At midspan the thickness reaches its smallest value, leading to a loaded area $A = 1.287^2 = 1.66\ \mathrm{m}^2$. Thus in the 3D model, wheel loads are applied of $91\ \mathrm{kN/m^2}$ (lane 1), $60\ \mathrm{kN/m^2}$ (lane 2) and $30\ \mathrm{kN/m^2}$ (lane 3).

The 2D model will be loaded by a line load, $q_k = 3 \cdot 9 + (17.8 - 3) \cdot 2.5 = 64\ \mathrm{kN/m}$ and point loads, $2 \cdot 600\ \mathrm{kN}$.

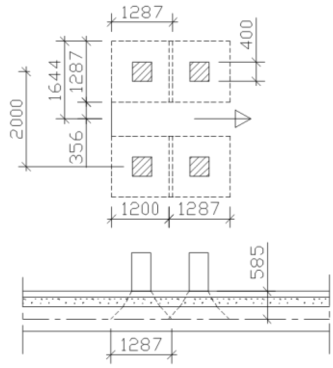

Figure 12: Wheel load spreading

7.5.2 Load model 4 (Crowd)

A crowd which loads the entire bridge should be taken into account.
$q_k = 2 + \frac{120}{L_{sj}+30} = 3.66\ \mathrm{kN/m^2}$ in which $L_{sj} = 42.5\ \mathrm{m}$.

In the 2D model, a line load is applied $q_k = 3.66 \cdot \big(25 - 2(0.355 + 0{,}6)\big) = 84.5\ \mathrm{kN/m}$

7.5.3 Braking load

60% of the vertical tandem axle load and 10% of the uniformly distributed vertical load, as used in lane 1 of load model 1, should be applied in horizontal direction. For the complete approach bridge this leads to a breaking force of $2196\ \mathrm{kN}$. The maximum value that should be taken into account is $900\ \mathrm{kN}$.

7.5.4 Sidewalk and cycle track

A uniformly distributed load should be applied of $5\ \mathrm{kN/m^2}$. When combined with load model 1, a value of $3\ \mathrm{kN/m^2}$ may be used. The cycle track has a width of $4.40\ \mathrm{m}$.

7.6 Support settlements

Due to different foundation stiffness's, the support do not subside evenly. Besides this unexpected settlement of the foundation may arise.

According to geotechnical investigations differential settlements up to $30\ \mathrm{mm}$ may arise. $20\ \mathrm{mm}$ settlement should be accounted for after completion of the bridge. Support settlement is a slow process as well and might be reduced to 54% due to aforementioned creep effects. Thus a support settlement of $10\ \mathrm{mm}$ in longitudinal direction is applied.

In the 3D model, a differential settlement of $10\ \mathrm{mm}$ in transverse direction is taken into account.

Since SCIA Engineer (structural analysis - FEM software) is not able to define a support settlement on a flexible support, the settlement is modelled as a load on the foundation. It's value is determined by trial-and-error until the desired deformation is reached.

7.7 Other loads

In design, several load cases should be investigated, next to the previously mentioned loads. In this research, only the governing loading is regarded. Loads that are not regarded, since their influence is of minor importance for the geometrically nonlinear analysis:

Main span

The main span loads the first pier of the approach bridge.

Stairs

In the approach bridge, stairs are designed for pedestrians to be able to reach the wetlands easily. There is only one pier equipped with stairs for each approach bridge.

Soil

Loading of the bridge due to the weight of soil consists of two mechanisms. The first mechanism is the weight of the soil on top of the pier foundation and the horizontal soil pressure. Next to that, when the surrounding area settles and the bridge does not, the soil adheres to the foundation. It thus mainly leads to a loading of the foundation.

Wind

For bridges with constant height a wind load of $1.32\ \mathrm{kN/m^2}$ should be applied. For the arches, it only leads to a small in-plane loading in transverse direction.

Fire

Fire under the bridge might lead to heating of the structure and eventually to spalling of concrete. Since the approach bridge crosses wetlands, it is unlikely that vehicles will load the bridge by fire.

Water flow and ice

Both water flow and ice load will lead to a loading on the piers. The ice load in longitudinal direction of the approach bridge might affect the behaviour of the arches.

Rain and snow

Loading due to snow need not be combined with traffic load and is thus not governing. Rainwater load may lead to high loads when it accumulates. Since the pavement has a slope, water will be drained sufficiently.

Maintenance truck

For inspection and maintenance purposes, a boom truck (32 ton) on the main road or on the footpath should be taken into account, together with traffic loading in load model 1.

Construction Planning

Since it is impossible to build the bridge in one stage, several static systems occur during construction. During building, the loading is applied in steps (e.g. pumping the foamed concrete backfill), which might lead to the governing loading situation.

Execution of Road Engineering Works

The most unfavourable loading pattern during maintenance of the pavement, is complete removal of the pavement on two half spans and maintenance equipment on the adjacent halves of the arch span. The load may be considered separately form the traffic load.

Fatigue Load

A number of truck types and their occurrence are prescribed in codes. In design, the resistance against this loading should be investigated. It does not affect second order calculations.

Ship collision

There is a possibility that ships run into the structure. For the first pier, several load cases are determined. The governing two load cases are the load parallel to the bridge axis ($54.8\ \mathrm{MN}$) and the load with an angle of $45°$ to this axis ($33.5\ \mathrm{MN}$ parallel and $16.8\ \mathrm{MN}$ normal to the bridge axis).

The secondary channel crosses the approach bridge. Ship collision is possible on the piers as well as on the superstructure. For the piers a load of $13.8\ \mathrm{MN}$ parallel and $6.9\ \mathrm{MN}$ normal or a load of $19\ \mathrm{MN}$ normal to the bridge axis are taken into account. For collision to the superstructure, a load of $1\ \mathrm{MN}$ is applied over a width of $1\ \mathrm{m}$ ($5\ \mathrm{m}$ from the centre of the pier).

Earthquake

Seismic activity in the Netherlands is rare and earthquake acceleration is rather small ($0.5\ \mathrm{m/s^2}$).

7.8 Load combinations

The load cases are merged into load groups. In the design, 36 principal combinations (for ultimate limit state and serviceability limit state) are formed out of these load groups, leading to a large number of load combinations that are investigated.

As stated before, this investigation focusses on the structural nonlinear behaviour of the arches. Therefore only few governing combinations will be regarded.

For the load combinations Eurocode EN 1990 is applied.

7.8.1 Serviceability limit state

To limit the number of load combinations, only the characteristic combination is regarded in serviceability limit state, since no combination factor is applied on the first variable load case. In the frequent and quasi-static combinations, this combination factor is applied.

The considered combination is described by:

$$E_d = E\left\{\sum_{j\geq 1} G_{kj} + P_k + Q_{k1} \text{ "}+\text{" } \sum_{i>1} \psi_{0\mathrm{i}} \cdot Q_{ki}\right\}$$

7.8.2 Ultimate Limit State

In ultimate limit state, the STR limit state is investigated in this thesis. STR deals with the failure and excessive deformations of structures:

$E_d \leq R_d$

In which:

$$E_d = E\left\{\sum_{j\geq 1} \gamma_{Gj} \cdot G_{kj} + \gamma_P \cdot P_k + \gamma_{Q1} \cdot Q_{k1} \text{ "}+\text{" } \sum_{i>1} \gamma_{Qi} \cdot \psi_{0\mathrm{i}} \cdot Q_{ki}\right\}$$

The partial load factors and combination factors are applied according to NEN-EN-1990/A1:2005/NB:2009. These coefficients have been changed in the currently valid code NEN-EN-1990+A1+A1/ C2:2011/NB:2011. Since the design has been carried out according to the 2009 standard, the values from this 2009 standard have been applied.

Table 6: Partial load factors

Permanent load		
$\gamma_{G,sup}$	=	1.35
$\gamma_{G,set}$	=	1.2
$\gamma_{P,fav}$	=	1.0
$\gamma_{P,unfav}$	=	1.2
Variable load		
$\gamma_{Q,traffic}$	=	1.35
γ_{Q}	=	1.5

Table 7: Combination factors

Combination		
$\psi_{0,\text{tandem system}}$	=	0.75
$\psi_{0,\text{traffic braking}}$	=	0.5
$\psi_{0,\text{temperature}}$	=	0.6
$\omega_{M,\text{daily temperature}}$	=	0.75

Table 8: Load combinations ULS

Load cases						gr1a			gr4		Temperature		
Name	Definition	ULS1	ULS2	ULS3	ULS4	ULS5	ULS6	ULS7	ULS8	ULS9	ULS10	ULS11	ULS12
		$\psi_0\,\gamma$	$\psi_0\,\gamma$	$\psi_0\,\gamma$	$\psi_0\,\gamma$	$\psi_0\,\gamma$	$\psi_0\,\gamma$	$\psi_0\,\gamma$	$\psi_0\,\gamma$	$\psi_0\,\gamma$	$\psi_0\,\gamma$	$\psi_0\,\gamma$	$\psi_0\,\gamma$
Permanent load													
LC01	Selfweight	1.35	1.35	1.35	1.35	1.35	1.35	1.35	1.35	1.35	1.35	1.35	1.35
LC02	DL: Foamed concrete	1.35	1.35	1.35	1.35	1.35	1.35	1.35	1.35	1.35	1.35	1.35	1.35
LC03	DL: Pavement	1.35	1.35	1.35	1.35	1.35	1.35	1.35	1.35	1.35	1.35	1.35	1.35
LC04	DL: Parapets	1.35	1.35	1.35	1.35	1.35	1.35	1.35	1.35	1.35	1.35	1.35	1.35
LC05	DL: Barriers	1.35	1.35	1.35	1.35	1.35	1.35	1.35	1.35	1.35	1.35	1.35	1.35
Shrinkage													
LC10	Shrinkage -15	1	1	1	1	1	1	1	1	1	1	1	1
Support settlement longitudinal													
LC800	Settlement axis 1	1.2	1.2	1.2	1.2	1.2	1.2	1.2	1.2	1.2	1.2	1.2	1.2
...	...												
LC811	Settlement axis 12	1.2	1.2	1.2	1.2	1.2	1.2	1.2	1.2	1.2	1.2	1.2	1.2
Support settlement transverse													
LC850	Settlement axis 2 (East)	1.2	1.2	1.2	1.2	1.2	1.2	1.2	1.2	1.2	1.2	1.2	1.2
...	...												
LC860	Settlement axis 12 (East)	1.2	1.2	1.2	1.2	1.2	1.2	1.2	1.2	1.2	1.2	1.2	1.2
LC870	Settlement axis 2 (West)	1.2	1.2	1.2	1.2	1.2	1.2	1.2	1.2	1.2	1.2	1.2	1.2
...	...												
LC880	Settlement axis 12 (West)	1.2	1.2	1.2	1.2	1.2	1.2	1.2	1.2	1.2	1.2	1.2	1.2
Temperature (ψ_0 = 0.6 ω_M = 0.75)													
LC25	Annual temp. decrease -29.5C			0.9	0.9	0.9	0.9	0.9	0.9	1.5	1.5	1.5	1.5
LC26	Annual temp. increase +23C			0.9	0.9	0.9	0.9	0.9	0.9	1.5	1.5	1.5	1.5
LC27	Daily temp. decrease -8C			0.68	0.68	0.68	0.68	0.68	0.68	1.125	1.125	1.125	1.125
LC28	Daily temp. increase +9C			0.68	0.68	0.68	0.68	0.68	0.68	1.125	1.125	1.125	1.125
Braking (ψ_0 = 0.5)													
LC30	Brake -4.5 kN/m (N-->S)			0.75	0.75	0.75	0.75	0.75		0.75	0.75	0.75	
LC31	Brake +4.5 kN/m (S-->N)			0.75	0.75	0.75	0.75	0.75		0.75	0.75	0.75	
LC32	Brake -4.5 kN/m (N-->S)			0.75	0.75	0.75	0.75	0.75		0.75	0.75	0.75	
LC33	Brake +4.5 kN/m (S-->N)			0.75	0.75	0.75	0.75	0.75		0.75	0.75	0.75	
LC34	Brake -4.5 kN/m (N-->S)			0.75	0.75	0.75	0.75	0.75		0.75	0.75	0.75	
LC35	Brake +4.5 kN/m (S-->N)			0.75	0.75	0.75	0.75	0.75		0.75	0.75	0.75	
UDL_Crowd (ψ_0 = 0.4)													
LC50	UDL_Crowd_span_1a								1.35				0.54
...	...								...				...
LC73	UDL_Crowd_span_12b								1.35				0.54
UDL_Edge1 (ψ_0 = 0.4)													
LC90	UDL_span 1a_Edge1			1.35						0.54			
...	...			...						...			
LC113	UDL_span 12b_Edge1			1.35						0.54			
UDL_Middle (ψ_0 = 0.4)													
LC130	UDL_span 1a_Middle				1.35						0.54		
...	...				...						...		
LC153	UDL_span 12b_Middle				1.35						0.54		
UDL_Edge2 (ψ_0 = 0.4)													
LC170	UDL_span 1a_Edge2					1.35	0.54	0.54				0.54	
...	...					...	...	...				...	
LC193	UDL_span 12b_Edge2					1.35	0.54	0.54				0.54	

Load cases						gr1a			gr4		Temperature		
Name	Definition	ULS1	ULS2	ULS3	ULS4	ULS5	ULS6	ULS7	ULS8	ULS9	ULS10	ULS11	ULS12
		$\psi_0\gamma$	$\psi_0\gamma$	$\psi_0\gamma$	$\psi_0\gamma$	$\psi_0\gamma$	$\psi_0\gamma$	$\psi_0\gamma$	$\psi_0\gamma$	$\psi_0\gamma$	$\psi_0\gamma$	$\psi_0\gamma$	$\psi_0\gamma$
UDL_Ped (ψ_0 = 0.4)													
LC200	UDL_span 1a_Edge2			0.54	0.54	0.54	1.35			0.54	0.54	0.54	
...	...			...	...	...	...			...	...	...	
LC223	UDL_span 12b_Edge2			0.54	0.54	0.54	1.35			0.54	0.54	0.54	
TS_Edge1 (ψ_0 = 0.75)													
LC300	TS_span1_Edge1_0.0L			1.35						1.01			
...	...			...						...			
LC347	TS_span12_Edge1_0.75L			1.35						1.01			
TS_Middle (ψ_0 = 0.75)													
LC400	TS_span1_Middle_0.0L				1.35						1.01		
...	...				...						...		
LC447	TS_span12_Middle_0.75L				1.35						1.01		
TS_Edge2 (ψ_0 = 0.75)													
LC500	TS_span1_Edge2_0.0L					1.35	1.01	1.01	1.01			1.01	
...	...					...	...	...	...			...	
LC547	TS_span12_Edge2_0.75L					1.35	1.01	1.01	1.01			1.01	

Serviceability limit state leads to a similar set of load combinations.

7.9 Load groups

To identify the nature of the loading, the load is applied via load groups. This way, distinction can be made between 'standard' and 'exclusive' load groups. In standard load groups, several load cases can occur simultaneous, whilst exclusive load groups imply that only a single load in the group should be applied in the load combination.

Table 9: Load group type (variable loads)

Load group	Type	Load group	Type
Support settlement	Exclusive	UDL_Middle	Standard
Annual temperature	Exclusive	UDL_Edge2	Standard
Daily temperature	Exclusive	TS_Edge1	Exclusive
Braking	Exclusive	TS_Middle	Exclusive
UDL_Crowd	Standard	TS_Edge2	Exclusive
UDL_Edge1	Standard		

7.10 Characteristic load combination

To obtain representative results for the city bridge design in the analytical calculations, characteristic load combinations are used, containing:

- Self-weight $\rightarrow q_{sw} = 312.5 \text{ kN/m}$
- Fill and parapets $\rightarrow q_{fill}(x) = 12 + 1.642 \cdot (x - 0.5l)^2 \text{ kN/m}$
- Pavement $\rightarrow q_{pave} = 233 + 2 \cdot 9 \text{ kN/m}$
- Traffic load $\rightarrow q_{traffic} = 64 + 4.40 \cdot 3 \text{ kN/m}$
- Tandem axis $\rightarrow F_{traffic} = 2 \cdot 600 \text{ kN}$

All distributed loads (q) summed and using partial safety factors ($\gamma_G = \gamma_Q = 1.35$) :

$$q_{Ed,SLS}(x) = 652.7 + 1.642 \cdot (x - 0.5l)^2$$
$$q_{Ed,ULS}(x) = 881.2 + 2.217 \cdot (x - 0.5l)^2$$

7.11 Foundation

7.11.1 Soil

In the geotechnical inquiry, a longitudinal soil profile was drawn, based on several cone penetration tests. Part of the profile is shown in Figure 13. A large part of the local soil consists of sand (indicated by white and yellow areas) with a top layer clay (the green areas).

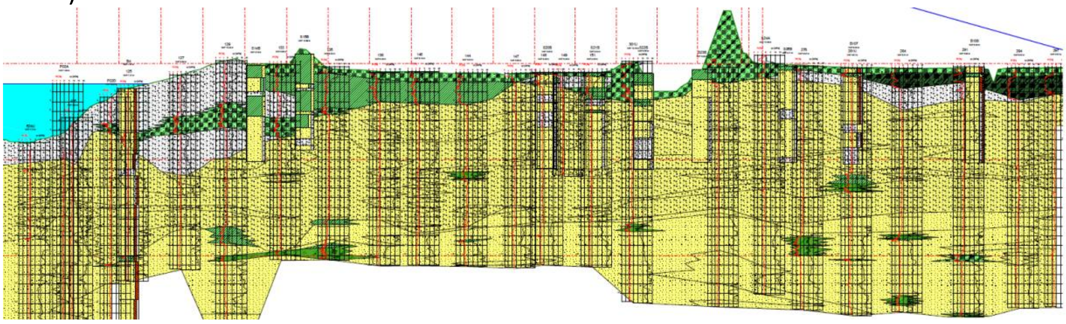

Figure 13: Longitudinal soil profile [GeoDR]

7.11.2 Pile systems

Two cast-in-situ pile systems are used:

- Vibro Pile 556/610
  Driven cast-in-situ pile, in which the steel tube will be pulled out while vibrating it, leading to an extra compaction of the soil and concrete.
- Casing Bore Pile $\emptyset 1{,}800\ \mathrm{mm}$ at main pier and $\emptyset 1{,}500\ \mathrm{mm}$ at the side channel
  Drilled pile with steel casing and concrete fill.

The casing bore piles are applied at the main pier due to the high loading of the main span. At the future secondary channel, also casing bore piles are used. Here a much deeper foundation level should be reached, compared with the adjacent spans. For all other foundations, the vibro pile system is chosen.

7.11.3 Foundation plan

The vibro pile is used in a $3 \cdot 6$ array, with skew angle 8:1. For the drilled piles, an array of $2 \cdot 3$ is applied, without skew angle. Each pier consists of two columns and each column has its own footing. For the main pier, drilled piles in a $3 \cdot 9$ array are applied.

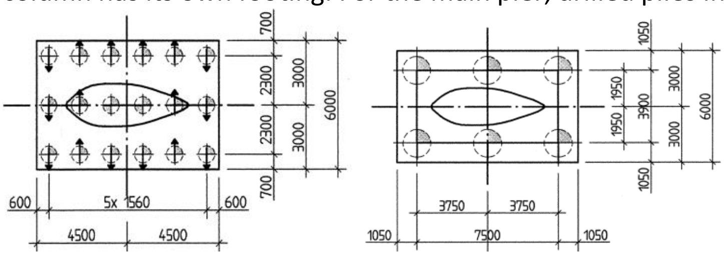

Figure 14: Characteristic column footing with vibro piles (left) and drilled piles (right)

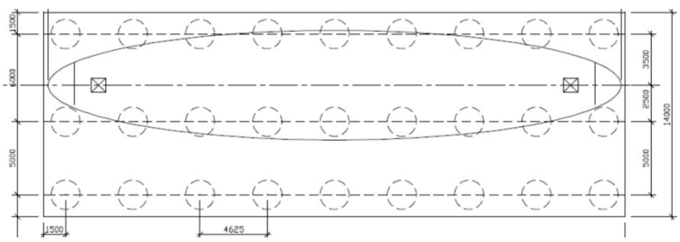

Figure 15: Foundation main pier

7.11.4 Soil stiffness

The soil stiffness and the reaction forces are modelled with flexible supports in all directions. The stiffnesses are determined by a geotechnical analysis. Since soil is an inhomogeneous material and testing is limited, the uncertainty should be accounted for. CUR recommendations advice a bandwidth which can be obtained by multiplying the characteristic values with factors $1/\sqrt{2}$ and $\sqrt{2}$. Now two structural analyses should be performed using the upper and lower value.

The horizontal confinement of the arches is one of the most important parameters in the design of the superstructure and a higher horizontal soil stiffness is beneficial for the load transfer. Nevertheless, the determination of the soil stiffness is not a topic in this thesis. The thesis focusses on the design verification by the structural engineer, in which the foundation stiffness is a boundary condition. However, the horizontal stiffness will be regarded as parameter to investigate its influence with respect to the second order effect in the superstructure.

7.12 Arched structure

The arches have a constant radius of curvature (~ 42.14 m) and a thickness of 500 mm, which increases to $1{,}500$ mm at the support over a length of 4.78 m The rise of the arch's centreline is 5.75 m. For the arches, concrete C35/45 with a decreased Young's modulus is used.

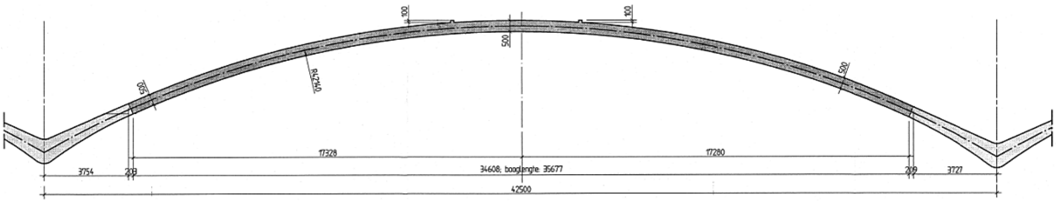

Figure 16: Arch geometry

7.12.1 Model

In the two dimensional model, the arches are modelled with curved beam elements ($500 \cdot 25{,}000$ mm). The discontinuous shape of the piers and the loading that increases towards the supports, lead to tensile stresses between the piers. This area adheres to the structure like a hammock. The material stiffness decreases when tensile stresses occur. This is modelled via decreasing the width of the elements. Besides that, to model the distributed loads correctly, including the self-weight, the extra span length due to the skew angle should be taken into account.

In the three dimensional model shell elements are used. Shell elements provide sufficient information to design the structure and it requires much less computer capacity and computation time, compared with volume elements.

7.12.2 Transverse beams

The arches are supported directly by the piers, so strictly speaking there are no transverse beams. However, the arch's thickness increases at the supports and to compensate the tensile forces, transverse prestress is applied at the supports. Together this creates an internal beam (Figure 17), which is used to phase the construction.

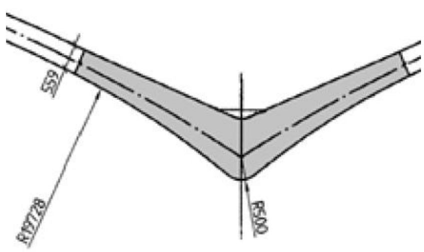

Figure 17: 'Hidden' prestressed transverse beam

7.13 Piers and footing

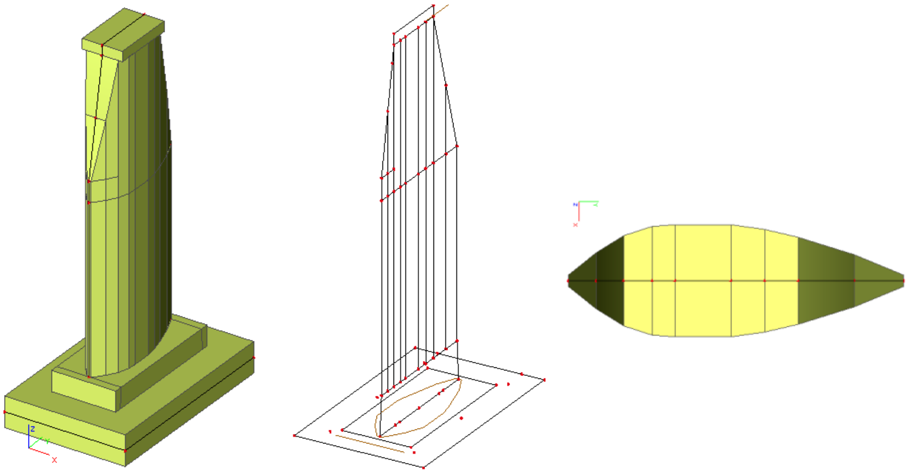

Figure 18: Pier with footing, visualization (left), FE model and cross-section (right)

The piers have a wing-like shaped cross-section as can be seen in Figure 18. Typical dimensions are 6×2 m at the base and 3×2 m at the top.

The footing is $9 \times 6 \times 1.5$ m in case the vibro piles are used. The drilled pile foundations have a footing of $9.6 \times 6 \times 1.5$ m with a concrete plinth of $3.9 \times 7.5 \times 1$ m.

The height of the piers is different for each set of piers, since not all foundation levels are equal (different at the secondary channel) and due to the vertical alignment of the bridge, the top sides of the piers have different levels as well. In the two-dimensional model, the piers are modelled as straight beam elements, split up into five elements with different cross-sectional properties. The footings are modelled as straight beams.

In the three-dimensional model, shell elements are used for the piers, including the variation in thickness. Plate elements (only bending) are used for the footings. For the piers concrete C35/45 and for the footings concrete C28/35 is used.

8. Buckling and magnification factors

Normal forces in structures will cause bending moments due to deviations from the perfect shape, that might be caused by for example execution tolerances, material inhomogeneity and deformations due to loading. These deviations can be modelled by an initial deformed shape. This initial deformation will increase due to the normal force and this will lead to bending moments.

To determine the magnitude of the effect, a geometrically nonlinear analysis should be performed. In several basic cases, this will result in the magnification factor $n/(n-1)$, in which n represents the critical load factor, the ratio between the buckling capacity and the acting load. For other cases, different magnification factors will be found, but the magnification factor $n/(n-1)$ appears to be a good estimation.

8.1 Buckling of rigid bar

The definition of stability of equilibrium is sufficient to derive the buckling load of rigid bars.

The equilibrium of forces is called stable in case after a small perturbation the system tends to return to its original equilibrium position. [Har07, translated]

When considering a rigid bar supported by a translational spring and loaded by a normal force (Figure 19), there is a drifting force caused by the load and a counteracting force that is provoked in the spring. Three different cases can be considered:

$drifting\ force - counteracting\ force < 0$	stable equilibrium
$drifting\ force - counteracting\ force > 0$	labile equilibrium
$drifting\ force - counteracting\ force = 0$	neutral equilibrium

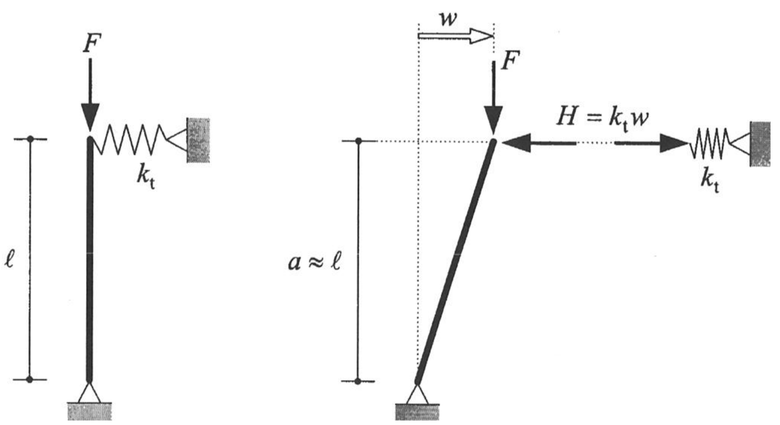

Figure 19: Buckling model rigid bar [Har07]

The buckling load is the boundary between stable and labile equilibrium. To calculate this load, the neutral equilibrium should be considered. For the rigid bar it will lead to:

$$F \cdot w - k_t \cdot l \cdot w = 0$$

$$F_{buc} = k_t \cdot l$$

8.2 Euler buckling

Leonhard Euler derived the formula to calculate the buckling load of a flexible, perfectly straight and homogenous beam (Figure 20).

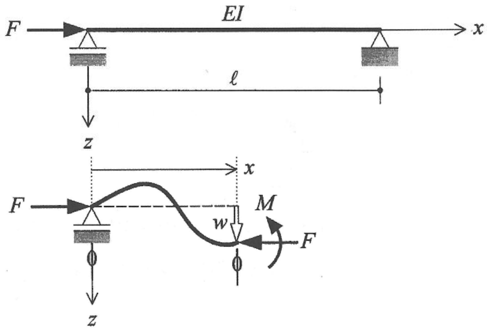

Figure 20: Euler buckling model flexible beam [Har07]

The equilibrium of the drifting and counteracting forces lead to:
$F \cdot w - M = 0$

The bending moment is replaced by $M = -EI\, w''$.
$EI\, w'' + F \cdot w = 0$

In this differential equation, two boundary conditions are required:
$w = 0 \; at \; x = 0 \; and \; x = l$

Introducing $\alpha = \sqrt{\frac{F}{EI}}$ will result in $w'' + \alpha^2 w = 0$

Using the trial solution $w = e^{tx}$, then the characteristic equation is obtained:
$t^2 + \alpha^2 = 0 \; \rightarrow t_{1,2} = \pm \alpha i$

Substituting the result and using Euler's formula $(e^{ix} = \cos x + i \sin x)$
$w = C_1 e^{\alpha x i} + C_2 e^{-\alpha x i} = C_1 \cos(\alpha x) + C_2 \sin(\alpha x)$

The boundary conditions lead to: $C_1 = 0$. To have a nontrivial solution $C_2 \neq 0$. The last condition can be fulfilled by requiring $\sin(\alpha l) = 0$. Which is true for
$\alpha_n = \frac{n\,\pi}{l} \quad in\, which \quad n = 1, 2, \ldots$

$$\sqrt{\frac{F_n}{EI}} = \frac{n\,\pi}{l} \;\rightarrow F_n = n^2 \cdot \frac{\pi^2 EI}{l^2} \quad (n = 1, 2, \ldots) \;\rightarrow F_{buc} = \frac{\pi^2 EI}{l^2}$$

8.2.1 Eigen value analysis

All possible buckling loads F_n are eigenvalues of the differential equation (homogenous boundary value problem): $EI\, w'' + F \cdot w = 0$, since all values F_n will lead to nontrivial solutions. The corresponding buckling shapes $w_n = C_{2,n} \sin(\alpha_n x)$ are called the eigenfunctions.

When discretizing the problem, as is done in finite element analysis, the same strategy can be applied. The eigenvalues of the stiffness matrix should be calculated and analogously the buckling modes are represented by the eigenvectors.

8.3 Derivation magnification factor

When including an initial deformation, the magnification of the deformation can be determined in a geometrically nonlinear analysis.

8.3.1 Rigid bar

When modelling an initial imperfection w_0 and assuming a second order deformation w, then the equilibrium of bending moments will result in:

$$F\,w = k_t\,l\,(w - w_0) = F_{buc}(w - w_0)$$

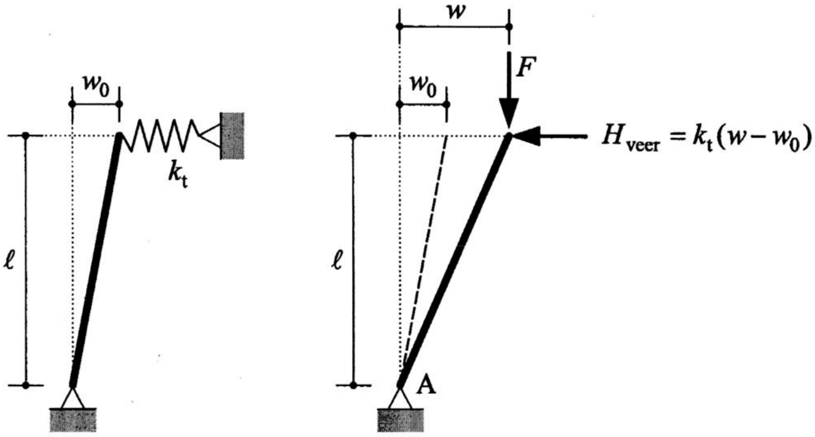

Figure 21: Rigid bar with imperfection [Har07]

As stated in paragraph 8.1, the buckling load is given by $F_{buc} = k_t l$. When introducing $n = F_{buc}/F$, the equilibrium can be rewritten to:

$$w\,(F - F_{buc}) = -F_{buc}\,w_0$$

$$w = \frac{-F_{buc}}{-F_{buc} + F} w_0 = \frac{\frac{F_{buc}}{F}}{\frac{Fbuc}{F} - 1} w_0 = \frac{n}{n-1} w_0$$

8.3.2 Flexible bar – sine shaped imperfection

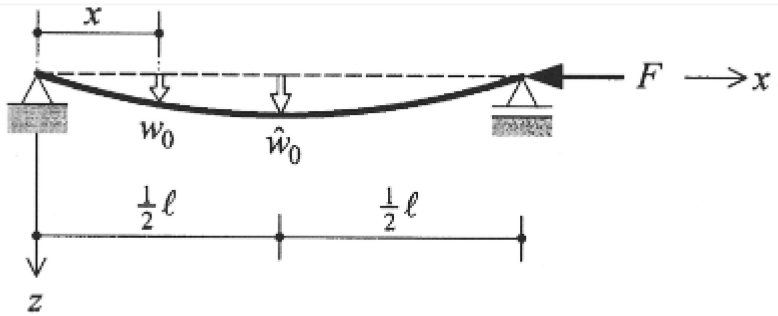

Figure 22: Flexible bar with imperfection [Har07]

When assuming a sine shaped imperfection $w_0(x) = \widetilde{w}_0 \sin\left(\frac{\pi x}{l}\right)$ (Figure 22) on a flexible bar, the normal force will cause bending moments in the bar. Due to these bending moments, the deformation increases, which causes higher bending moments.

Assuming that equilibrium is found at a deformation w, the differential equation reads:

$EI(w - w_0)'''' + Fw'' = q = 0$

Introduction $\alpha^2 = \frac{F}{EI}$ and $\beta = \frac{\pi}{l}$, the differential equation is:

$w'''' + \alpha^2 w'' = w_0'''' = \beta^4\, \widetilde{w}_0 \sin(\beta x)$

The boundary conditions are $w = 0$ and $M = 0$ at $x = 0$ and $x = l$
A particular solution to the differential equation is $w_p(x) = \widetilde{w} \sin(\beta x)$. This solution meets the boundary conditions and no homogenous solution has to be considered, since all integration constants will appear to be equal to zero.

Substitution of the solution in the differential equation will lead to the deformation $\widetilde{w}$:
$\beta^4 \widetilde{w} \sin(\beta x) - \alpha^2 \beta^2 \widetilde{w} \sin(\beta x) = \beta^4\, \widetilde{w}_0 \sin(\beta x)$

$$\frac{\beta^2}{\alpha^2} = \frac{\left(\frac{\pi}{l}\right)^2}{\frac{F}{Ei}} = \frac{\left(\frac{\pi^2 EI}{l^2}\right)}{F} = \frac{F_{buc}}{F} = n$$

$$\widetilde{w}(\beta^4 - \alpha^2\beta^2) = \beta^4\, \widetilde{w}_0 \quad \rightarrow \quad \widetilde{w} = \frac{\beta^2}{\beta^2 - \alpha^2}\widetilde{w}_0 = \frac{\frac{\beta^2}{\alpha^2}}{\frac{\beta^2}{\alpha^2} - 1}\widetilde{w}_0 = \frac{n}{n-1}\widetilde{w}_0$$

8.3.3 Flexible bar with parabolic imperfection

In case the imperfection of the bar (Figure 22) is assumed to have a parabolic shape $w_0(x) = \widetilde{w}_0 \frac{4}{l^2}(lx - x^2)$, the same differential equation and boundary condition can be considered. The solution reads [Har07]:

$$w(x) = \frac{8}{(\alpha l)^2}\left[\frac{\cos\left(\frac{\alpha l}{2} - \alpha x\right)}{\cos\left(\frac{\alpha l}{2}\right)} - 1\right]\widetilde{w}_0 \qquad \alpha = \sqrt{\frac{F}{EI}}$$

The maximum deformation at $x = l/2$ is given by:

$$w\left(\frac{l}{2}\right) = \frac{8}{(\alpha l)^2}\left[\frac{1 - \cos\left(\frac{\alpha l}{2}\right)}{\cos\left(\frac{\alpha l}{2}\right)}\right]\widetilde{w}_0$$

In this case, the magnification is not equal to $n/(n-1)$. However, when plotting both graphs, it can be concluded that the differences are small.

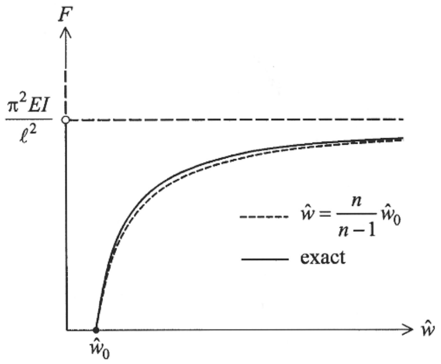

Figure 23: Magnification of deformations - exact and approximation [Har07]

8.3.4 Flexible bar with transverse load

In case the flexible bar is perfectly straight and homogenous, a load is applied in transverse direction, bending moments develop to transfer the load, which result in a deformation. This deformation will increase due to normal force.

Considering a two hinged bar with a point load P at midspan and normal force F. The deflection of the bar due to the point load P can be calculated with the standard engineer formula:

$$\widetilde{w}_0 = \frac{Pl^3}{48EI}$$

Solving the differential equation will yield the deformation [Har07]:

$$w = \frac{Pl}{4F}\left[\frac{\sin{(\alpha x)}}{\frac{\alpha l}{2}\cos\left(\frac{\alpha l}{2}\right)} - \frac{x}{\frac{l}{2}}\right]$$

Substituting $x = l/2$:

$$w\left(\frac{l}{2}\right) = \frac{3}{\left(\frac{\alpha l}{2}\right)^2}\left[\frac{\tan\left(\frac{\alpha l}{2}\right)}{\left(\frac{\alpha l}{2}\right)} - 1\right]\frac{Pl^3}{48EI} = \frac{3}{\left(\frac{\alpha l}{2}\right)^2}\left[\frac{\tan\left(\frac{\alpha l}{2}\right)}{\left(\frac{\alpha l}{2}\right)} - 1\right]\widetilde{w}_0$$

Again, there is no mathematical relation with the $n/n-1$ formula. However, in case the normal force $F \leq 0.9\ F_{buc}$, the differences appear to be smaller than 1.3% [Har07].

To estimate the bending moment in the bar, there are two possibilities, in which the second equation is a better representation of the model.

$$M = \frac{n}{n-1}\,M_0 \quad and \quad M = M_0 + F\frac{n}{n-1}w_0$$

The magnification factor is exact for the sine shaped initial deformation. For all shapes of the initial deformations that are smaller than the sine shape, but with an equal amplitude, the factor $n/n-1$ overestimates the geometrically nonlinear effect and is thus a conservative but safe approach.

8.3.5 Difference for arched structures

The most important difference between the geometrically nonlinear behavior of arches and compression members like columns is the loading. In columns the normal force is an external load on the system, independent from transverse loads and deformations. In arches the transverse load causes the normal force and deformations of the member. The normal force in arched structures cannot be considered separately from the transverse loading and the deformations.

8.4 Arch buckling

The main advantage of arches and shells is the possibility of spanning large areas with relatively slender cross-sections, since loads are transferred mainly via compression. These normal forces may reach values up to $1/3 \cdot F_{buc}$. Arches may buckle in-plane or out-of-plane. The out-of-plane buckling is not governing for the city bridge design, due to its width of 25 m. Therefore only in-plane buckling will be considered.

8.4.1 In-plane buckling circular arch

The in-plane buckling of arches is analytically solvable for few specific cases only, for example the radially loaded circular arch, which is discussed by Timoshenko in [Tim61]. The geometry of the arch and loading, will lead to normal forces only ($N = qR$).

Solving the differential equation will result in the critical load q.

$$\frac{d^2w}{d\theta^2} + w = -\frac{qR^3w}{EI}$$

Introducing $k^2 = 1 + \frac{qR^3}{EI}$ and boundary conditions: $w = 0 \; at \; \theta = 0 \; and \; \theta = 2\alpha$

$$\frac{d^2w}{d\theta^2} + k^2w = 0$$

$$w = A\sin(k\theta) + B\cos(k\theta)$$
$$w(0) = A\sin(0) + B\cos(0) = 0 \quad \rightarrow B = 0$$
$$w(2\alpha) = A\sin(2\alpha k) = 0 \qquad \rightarrow \sin(2\alpha k) = 0 \qquad \rightarrow k = \frac{\pi}{\alpha}$$

Substituting the result $k = \pi/\alpha$ (the smallest root that satisfies the condition of inextensibility) in the formula for k^2 will lead to the critical load on the arch. The buckling mode is represented by $w = A\sin\left(\frac{\pi\theta}{\alpha}\right)$, see Figure 24.

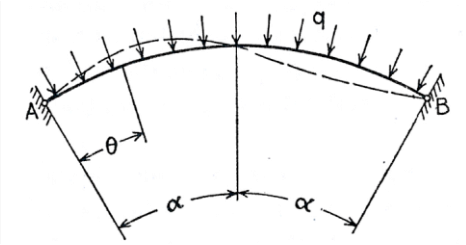

$$q_{cr,arch} = \frac{EI}{R^3}\left(\frac{\pi^2}{\alpha^2} - 1\right)$$

$$q_{cr,shell} = \frac{Et^3}{12(1-\nu^2)R^3}\left(\frac{\pi^2}{\alpha^2} - 1\right)$$

Figure 24: Buckling radially loaded circular arch [Tim61]

For cylindrical vaulted shells hinged along the straight edges, the same equation is valid, in which the plate stiffness $\frac{Et^3}{12(1-\nu^2)}$ is substituted instead of the bending stiffness EI.

In Figure 25 snap through buckling and anti-symmetrical (sway) buckling are shown. Both buckling modes can be defined by sine shapes. However, like all pure buckling problems, the amplitude of the mode is not solveable.

$$u_{snap\ through} = A \cdot \sin\left(\frac{\pi x}{l}\right) \qquad u_{asymmetrical} = A \cdot \sin\left(\frac{2\pi x}{l}\right)$$

In case the translation of the supports is prevented and the bar is inextensible, snap through buckling will not occur. However, the snap through mode can still be reached via the sway buckling mode, in which the buckled shape develops itself anti-symmetrically to the snap through mode.

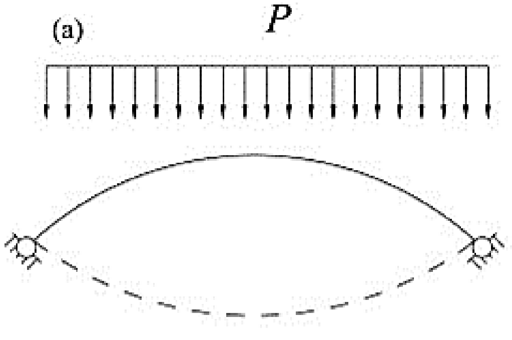

Figure 25: (a) snap through buckling and (b) anti-symmetrical buckling [Moo07].

The radial loading pattern on a circular member occurs for example in pressure vessels or in storage tanks. However, in case $\alpha = \pi$ (complete ring) the critical load according to arch buckling is $q_{cr} = 0$, since for $\alpha = \pi$ both supports have the same position. For arch bridges, the radial load does not occur often. A large share of the load is based on gravity (self-weight, dead-weight and part of the variable load). Buckling due to these loads are more complicated to determine analytically, especially when the deformations are taken into account. Alternatively, the problem can be solved by an eigenvalue and eigenvector analysis, which is implemented in most finite element programs.

For shallow arches, in which the rise is relatively small with respect to the span, snap through buckling is likely to be governing. For less shallow arches, the swaying buckling mechanism will be governing for in-plane stability. Buckling shapes with three or more half sine waves all lead to a lower buckling length, compared to the buckling modes as shown in Figure 25 and thus a higher buckling load.

8.4.2 In-plane buckling parabolic arch

The parabolic arch with a uniform load carries load via normal force only too, when the axial shortening of the member is not taken into account.

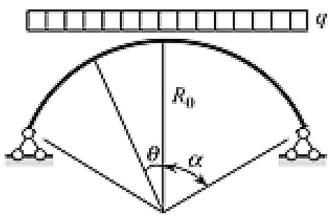

Figure 26: Uniformly loaded parabolic arch [Kar12] (redrawn)

For the parabolic arch, the critical load may be calculated by the formula, in which the K values are provided by [Kar12] and [Tim61].

$$q_{cr} = K \cdot \frac{EI}{l^3}$$

Table 10: K factors [Kar12]

f/l	0.1	0.2	0.3	0.4	0.5	0.6	0.8	1.0
Hingeless	60.7	101.0	115.0	111.0	97.4	83.8	59.1	43.7
2 hinged	28.5	45.4	46.5	43.9	38.4	30.5	20.0	14.7

8.5 Shell stability

The stability of shell structures is fundamental different with respect to global instability of columns and walls. Even instability of arch structures (see paragraph 8.4) is incomparable with shell instability. In shells, a kind of plate buckling mechanism occurs, as can be seen in Figure 27, in which the first, the fifth and twelfth buckling modes of a spherical shell are displayed.

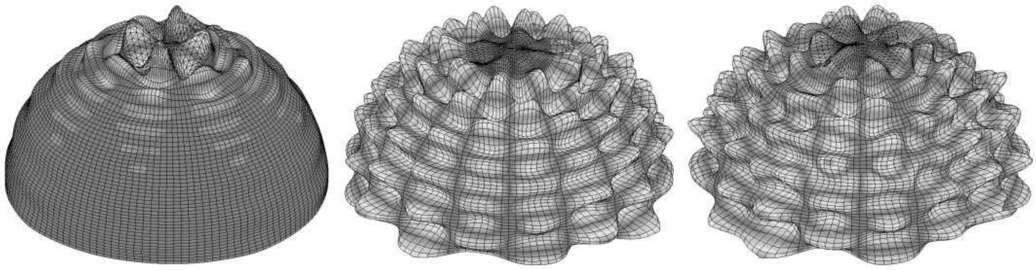

Figure 27: Buckling modes 1, 5 and 12 of spherical shell [BPe08].

Though, the concrete arches in the approach bridge differ from spherical shells with respect to the occurrence of ring normal forces. However, the structure is not a spherical shell but a barrel vaulted shell (“tonschaal” in Dutch).

8.6 Barrel vaulted concrete roofs

The barrel vault shells is a unique design solution which has not yet been applied before in bridge design. Thus there is no literature on barrel vaulted shells loaded by traffic. However, barrel vaults have been applied in the first half 20th century in roof systems, popular at that time due to the economic material use. In 1961 the Dutch journal *‘Cement’* published an overview of shell-structures in the Netherlands, containing 28 barrel vault shells.

With respect to roofing there has been research executed on barrel vault shells and some information is available in literature. Nevertheless, the increasing labour costs reduced the use of the barrel vaulted shells and together with the development of finite element analysis tools, research on the analysis of the barrel vaults stopped as well.

Still some information on barrel vault shells is available. In [Far92], there is a chapter on barrel vaulted roofs. The load transfer is visualized by means of a plot of stress trajectories (Figure 28), the three-dimensional load transfer (beam action in l_1 direction and arch action in l_2 direction) is clearly visible.

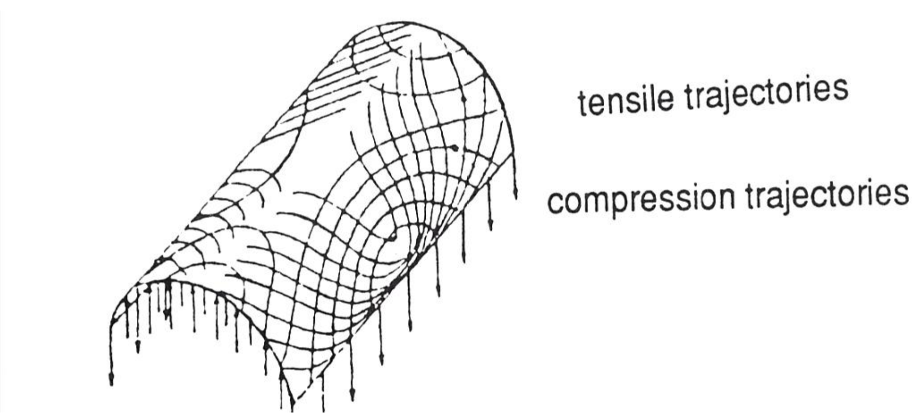

Figure 28: Stress trajectories in a simply supported barrel vaulted shell [Far92].

8.6.1 Buckling modes vaulted cylindrical shell roofs

The roof system is mainly applied in industrial halls, which requests for large column free space. Literature on these roofs focussed on roofs supported by only four columns. Depending on the span ratio $l_1\ /\ l_2$ (a) beam action is predominant when $l_1\ /\ l_2 > 4$ (b) arch action is important for $l_1/\ l_2 < 1$ or an intermediate load transfer occurs (c). Depending on the span ratio, different buckling modes occur as can be seen in Figure 29.

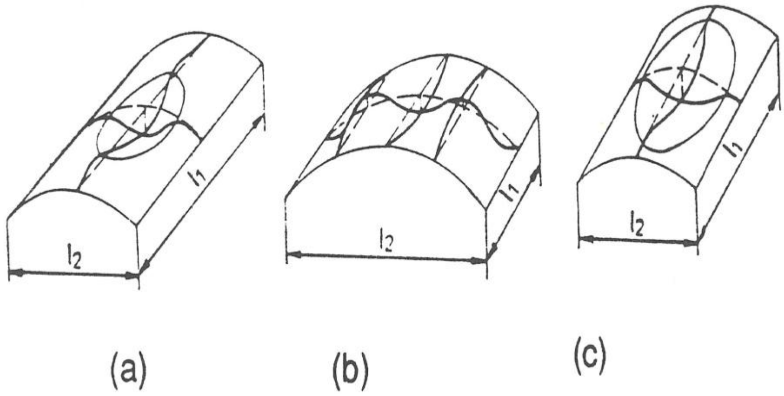

Figure 29: Buckling modes of roof cylinders [Far92].

In the approach bridge design, the shells span in transverse direction by beam action and in longitudinal direction mainly by arch action. The accessory spans are $l_1 = 21.3\text{m}$ and $l_2 = 42.5\ \text{m}$ which lead to $l_1/l_2 = 0.5 < 1$. Arch action in longitudinal direction is thus the main load carrying mechanism, when considering the geometry of a single span in the approach bridge. Using two dimensional arch models and neglecting the transverse direction is the most appropriate step in the geometrically nonlinear analysis of arches.

9. Parameter analysis arch buckling

The sensitivity of the buckling capacity of arches is investigated when varying the cross-section, the span and the rise of the arch. For each parameter, the critical loads are obtained with Scia Engineer (eigen value analysis, based on a unity load) for several translational support stiffnesses. In the buckling analyses, both the symmetrical and anti-symmetrical buckling modes (eigenvector) are considered, since it is not known in advance which mode is governing. For the considered circular arches, the pure (bifurcation) buckling will not occur, since bending moments and deformations will be present.

9.1 Critical loads beam model

In Figure 30, the critical buckling loads are displayed for the arch, when varying the translational support stiffness. The first analysis is based on a beam cross-section $300 \cdot 600\, mm$. The results are obtained via linear stability analysis. Only in-plane buckling is considered. Out-of-plane buckling is very unlikely to occur in the city bridge and therefore it is not considered in the analysis.

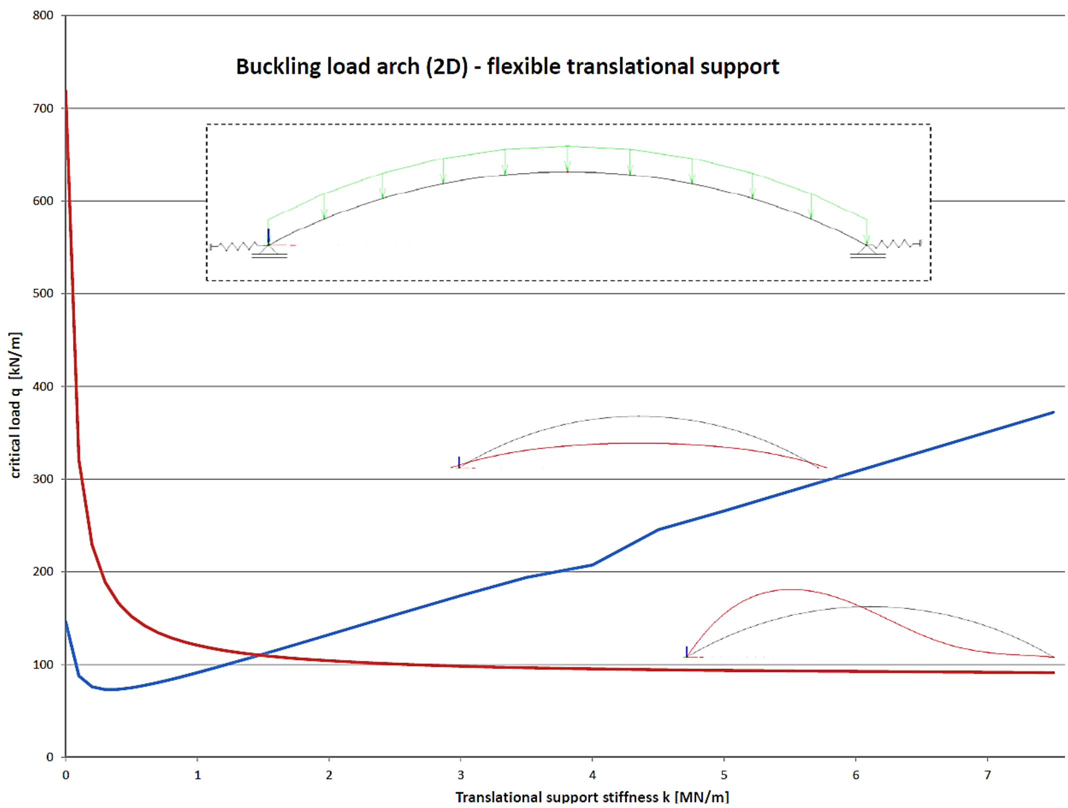

Figure 30: Buckling loads for flexible supported arch

For low support stiffnesses, the symmetrical mode will lead to the governing buckling load. Increasing the support stiffness, will lead to a higher buckling load, since more energy is required for the displacement of the supports. However, in the anti-symmetrical buckling mode the supports do not displace and the support stiffness is only an indirect parameter. At some point, the buckling load of the symmetrical mode will be that high, that the anti-symmetrical buckling mode will be governing.

The high buckling loads for lower support stiffnesses are explained by the fact that the normal forces that occur in the arch depend nonlinearly on the support stiffness (see part 2). Lower support stiffness will lead to lower normal forces and consequently higher bending moments. The arch behaviour reduces and the arch will act more like a curved beam. Thus decreasing support stiffness will lead to higher buckling loads. Especially in case $k < 0.3\ MN/m$, the low normal forces cause increasing critical loads.

In case the support stiffness $k = 0$, there is no constraint and no horizontal thrust. The normal force at the crown of the arch is zero as well. However, due to the curved shape and the direction of the support reaction, normal forces will develop to preserve equilibrium when combined with the support reaction and the shear forces (Figure 31). The buckling load will thus keep a finite value.

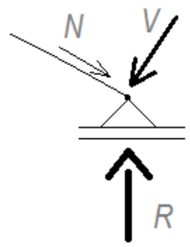

Figure 31

9.2 Parameter study based on a 3D model

Besides the support stiffness, several other parameters influence the buckling load of arches. In [Tim61] a formula for the critical load is found, in which γ_4 depends on the rise to span ratio. [Kar12] uses the same formula, with slightly different values for γ_4.

$$q_{cr} = \gamma_4 \cdot \frac{EI}{l^3}$$

Based on this information, the investigated parameters are the span, the cross-sectional height and the rise to span ratio. Additionally, the effect of half span loading and the effect of the width on the buckling load are researched. Since a three dimensional model is used, the load will be higher and the line supports will be longer, when increasing the width. Although the three dimensional model will lead to three dimensional buckling modes, only the two previously considered in plane arch buckling modes are investigated. In the three dimensional buckling modes, the cross-section rotates along the span. In stability analysis, the buckling loads of these three dimensional buckling modes appeared not to be governing. The investigated – two dimensional - buckling modes are displayed in Figure 32.

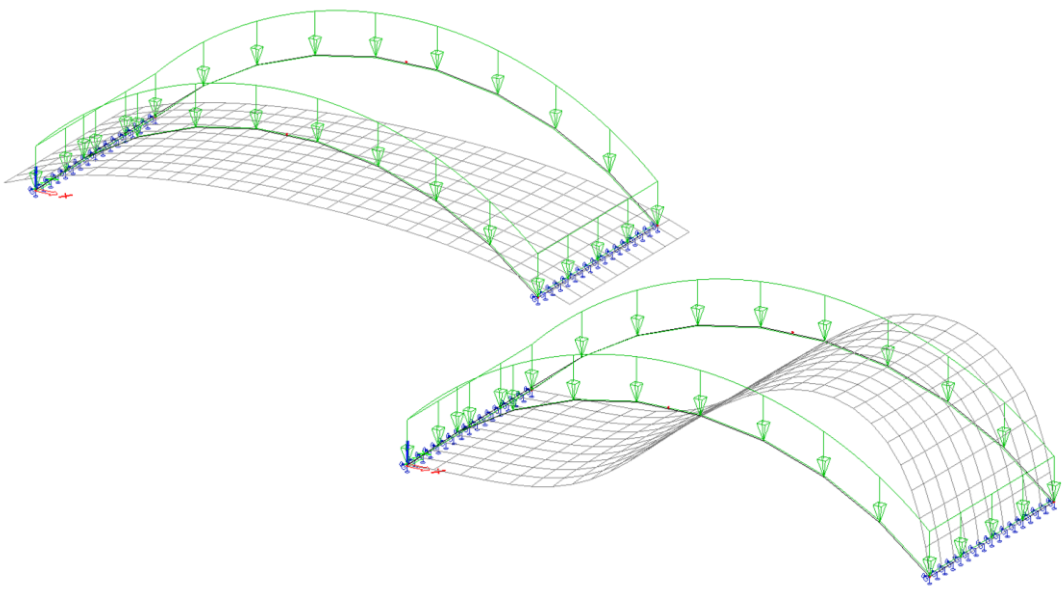

Figure 32: Investigated buckling modes

Varying width

Since the loads and the supports are defined per unit width, the size effect of the width can be investigated by just extending the model. For the three dimensional models, several support stiffnesses are investigated for the width ranging from $0.25\ m$ to $100\ m$. The support stiffness k in the legends is stated in $[MN/m^2]$.

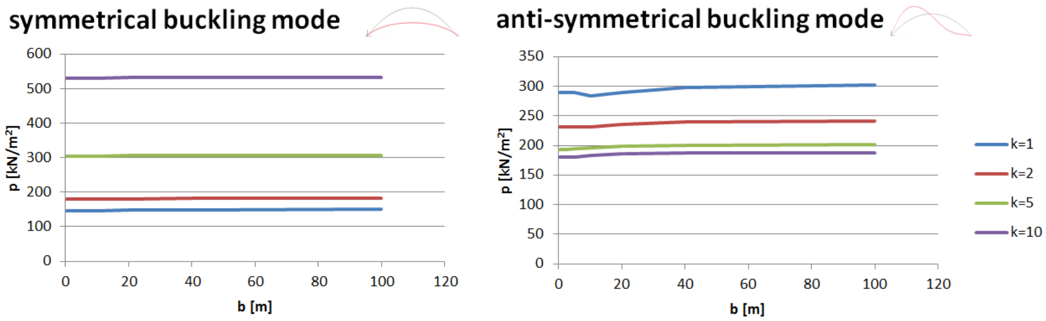

Figure 33: Influence of the width on the buckling load p

The results show that the buckling load p hardly varies when changing the width of the structure, in case line supports and uniformly distributed loads are applied. Only the anti-symmetrical mode shows a small deviation for the lower stiffnesses. However, for low support stiffnesses, the mode is not governing. The choice to investigate only the 25 m width, as applied in the city bridge design, is justified due to the small variation.

Cross-sectional height

The critical load is determined for different cross-sectional heights. Since the moment of inertia I for the cross-section is linearly related to the critical buckling load according to literature, consequentially the height should be related cubically to the buckling load. Therefore, the dotted line is plotted, representing h^3 is multiplied by the weighted average of all calculated results.

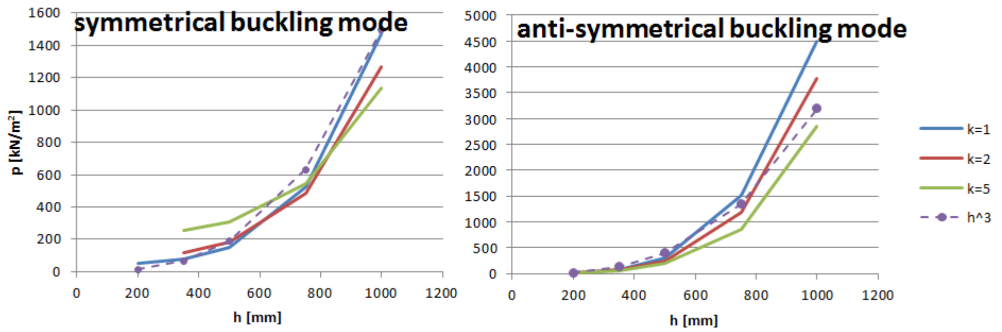

Figure 34: Buckling load p for different cross-sectional heights

As can be seen in Figure 34, there is good correspondence with the cubic relation. For the symmetrical buckling mode, the relation of the height and the load with the support stiffness is not unambiguous. For larger cross-sectional heights, the lower support stiffness will cause higher buckling loads (see 9.1). For the lower cross-sectional heights, the buckling load decreases for lower support stiffness. This can be explained by the lower bending stiffness, which leads to lower bending moments in case the arch deforms (analogous to a cable). These lower bending moments result in higher normal forces and that causes lower buckling loads. The relation between buckling load and support stiffness completely inverts for different bending stiffnesses. Thus, the support stiffness k and bending stiffness EI should be considered simultaneously.

Span

The length of a member determines the buckling length together with the boundary conditions. As stated in the Euler buckling formula, the buckling load is inverse proportional to the square buckling length ($1/l^2$), in case an external normal force is applied. However, for arches the normal force is caused by a uniform distributed load, which depends on the length too. Cubic inverse proportionality ($1/l^3$) seems a reasonable relation for the distributed critical buckling load and the member length. This relation is stated for more elementary models in literature too.

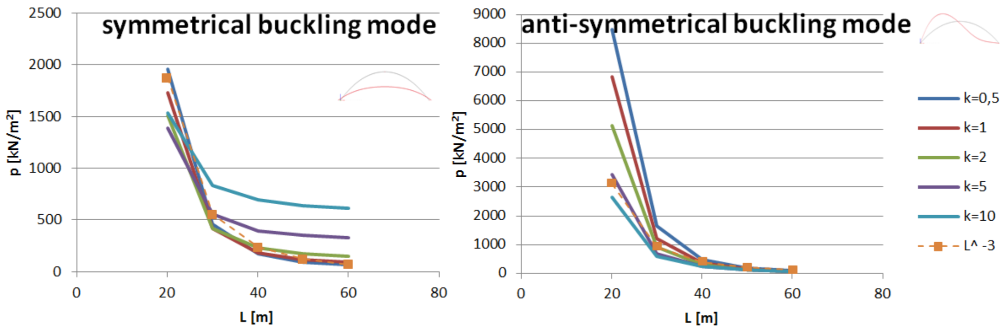

Figure 35: Buckling loads for different span lengths

Again a dotted line is plotted, in these graphs representing l^{-3}, factored by a weighted average of the computed results.

Rise to span ratio

For parabolic and circular arches, the rise to span ratio determines the shape of the arch. [Tim61] determined the values for the factor γ_4 as a function of the rise to span ratio (Figure 37), to compute the buckling load $q_{cr} = \gamma_4 \cdot EI/l^3$ for a parabolic arch with uniform distributed load. The large influence of the boundary conditions on the buckling length and the buckling load is illustrated in the figure. The two governing buckling modes are already taken into account in the γ_4 values. Figure 36 illustrates this. These γ_4 values are backwards calculated based on the eigenvalue analysis (finite element software), which appear to match reasonably with the values that are found in literature. For low rise to span ratios, the symmetrical buckling mode is governing, whilst the anti-symmetrical mode is governing for the higher ratios.

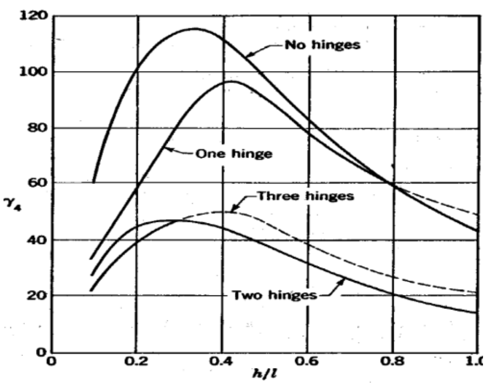

Figure 37: Values γ_4 factor [Tim61]

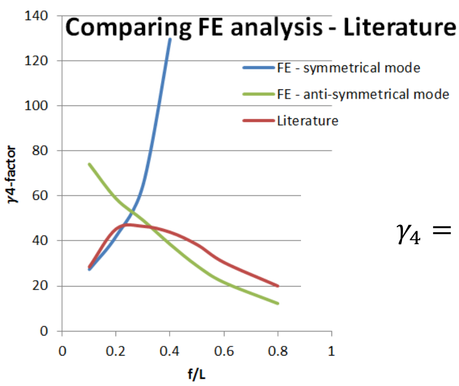

$$\gamma_4 = \frac{q_{cr} \cdot l^3}{EI}$$

Figure 36: Comparing FE and literature [Tim61]

Circular arches with uniform distributed load are evaluated as well for different rise to span ratios. Two combinations are analysed, first a span of 25 m with cross-sectional height of 350 mm and second a span of 40 m and cross-sectional height 500 mm.

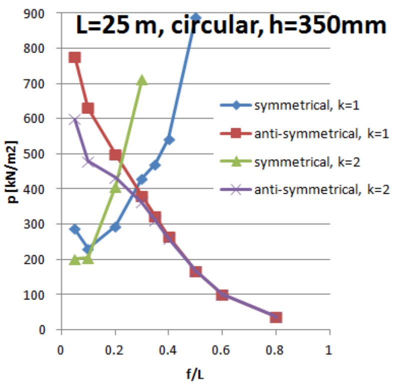

Figure 39: Rise to span - circular L=25 m

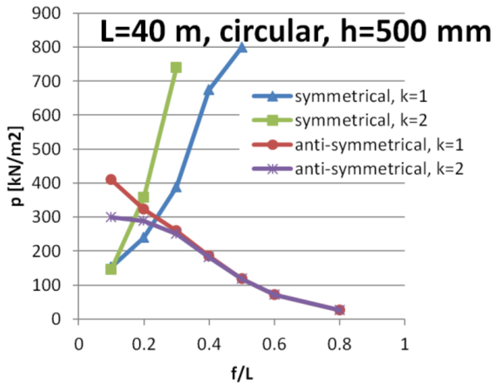

Figure 38: Rise to span – circular L=40 m

For the circular arch similar results are obtained. The main difference with the parabolic shape, is the considerably lower capacity of the circular arch for rise to span ratios $f/l > 0.5$. However, rise to span ratios larger than 0.5 are hardly applied in bridge design. A semicircle has a rise to span ratio of 0.5, a full circle has ratio 1.0. The highest buckling loads are obtained for rise to span ratios of 0.2 to 0.3 for circular arches and 0.3 to 0.4 for parabolic arches.

Half span loaded

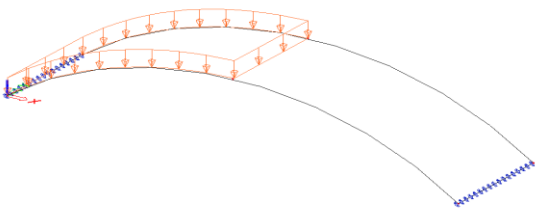

Figure 40: Half span loaded

Loads that act on a part of the arch will cause high bending moments and lower normal forces and thus leading to the governing situation for the reinforcement design of concrete arches. The effect of half loaded spans on buckling is analysed and the results are displayed in Figure 41.

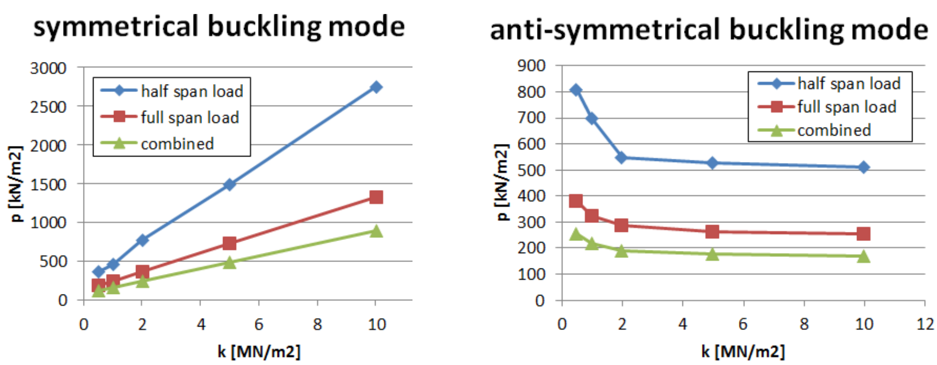

Figure 41: Buckling load half loaded and fully loaded arches

Since only a linear calculation is performed, the deformed shape is not taken into account. Therefore, only the lower normal forces are revealed in the results. The lower normal forces, in case only a half span is loaded, will lead to higher buckling loads.

When combining the fully loaded span and the half loaded span, the buckling load appeared to decrease according to the reciprocal relation, with an error of only 1%:

$$\frac{1}{p_{combined}} = \frac{1}{p_{half\ span\ loaded}} + \frac{1}{p_{full\ span\ loaded}}$$

9.3 Final remark on arch buckling sensitivity

The relation found in literature between bending stiffness, rise and span, derived by using the differential equation for arch buckling, based on the two basic models (parabolic with uniform load and circular with radial load), remains applicable for more complex situations which are evaluated via stability analysis in finite element software. The major difference is the factor for the rise to span ratio (γ_4), which is much lower for circular arches with high rise to span ratios (in Figure 42 the governing factors are displayed in one graph for different circular arches). Although for rise to span ratios between 0.2 to 0.4 a large scatter is found in the results, the values have the same order of magnitude, compared with the factors that are given by [Tim61] for the parabolic arch.

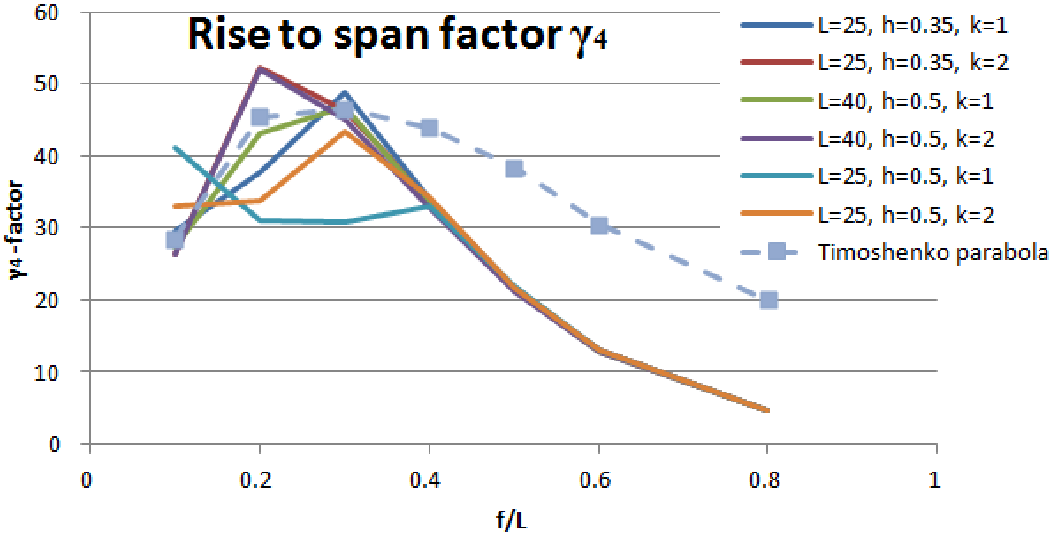

Figure 42: Rise to span factors γ_4

The arch buckling analysis is based on literature and finite element software. The analytical solution is not a practical approach, as stated in [Kar12], for example to model different boundary conditions on the radially loaded circular arch, the differential equation is given by:

$$\frac{d^6u}{d\varphi^6} + 2\frac{d^4u}{d\varphi^4} + \frac{d^2u}{d\varphi^2} + \frac{qR^3}{EI}\left(\frac{d^4u}{d\varphi^4} + \frac{d^2u}{d\varphi^2}\right) = 0$$

In case no radial load, but for example gravity load is considered, the differential equation will be more complicated, since deformation leads to a changing angle between load and arch axis. Furthermore, the solution will contain variable coefficients [Kar12]. Thus, solving the mathematical statement will be complicated and cumbersome, when it is kept in mind that answers are easily obtained via finite element analysis.

Part 2: Single Arch Analysis (2D)

Contents – part 2: Single arch analysis

10. Introduction to Part 2

This part deals with the basic structural mechanics that are involved in the analysis of arched structures. Main goal is to investigate the differences between the linear and geometrically nonlinear approaches, in order to obtain knowledge required for the judgement of software output.

Therefore, literature has been studied to investigate the assumptions that are made to linearize arch analysis and to accept or reject these assumptions when analysing geometrically nonlinearity. Next the differential equation for arch structures has been reviewed and analysed for linear and geometrically nonlinear behaviour. The analysis path via the differential equation will lead to an imaginary load that is caused by the product of the normal force and the second derivative of the deformation. For several load cases the analyses are carried out.

Main sources in literature for this part are [Bou89] and [Wel12].

11. Theory of arches

11.1 Classical methods

11.1.1 Three hinged arch

From the analysis point of view, the three hinged arch is the most basic one. Due to the third hinge, the arch is statically determined and normal forces and bending moments can be determined by using the static equilibrium equations.

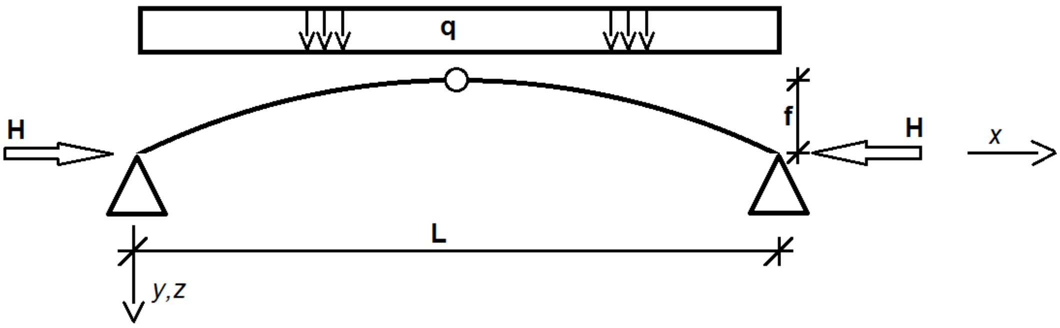

Figure 43: Statically determined - three hinged arch

By considering the section at the hinge, the horizontal thrust is determined via:

$$\sum F_H = 0 \rightarrow N_{hinge} = H$$

$$\sum M = 0 \rightarrow H \cdot f = \frac{1}{8} q l^2$$

Now the horizontal thrust is known, the bending moment distribution along the x-axis can be determined (in the applied axis system, the arch height '$z(x)$' is defined by negative coordinates):

$$M(x) = \frac{1}{2} q\, x(l - x) + H \cdot z(x)$$

11.1.2 Two hinged arch

The two hinged arch is simply statically undetermined. By solving one of the unknown parameters, the problem can be solved by considering the static equilibrium.

Horizontal Thrust

Regarding the horizontal thrust as the parameter to solve, seems the most appropriate way to decompose the problem. When replacing one support by a sliding support, the arch becomes a curved beam and a horizontal displacement occurs as a result of the vertical deflection. For small rotations it holds that the horizontal displacement equals rotation times vertical distance. Combining this with the definition of curvature (κ) and integrating it over the arch length, the horizontal displacement is known. M_{beam} represents the bending moment as a result of the beam action (without the horizontal thrust).

$dh = -z\, d\varphi$ and $\kappa = \frac{d\varphi}{dx} = \frac{M_{beam}}{EI}$

$$h_{beam} = \int_{arch} -\frac{M_{beam}\, z}{EI} ds$$

In the second step, a horizontal force H is applied, which counteracts the horizontal deformation. This deformation can be calculated via the bending moment $H \cdot z$, analogous to the displacement due to beam action.

$$h_H = \int_{arch} \frac{M_H\, z}{EI} ds = \int_{arch} -\frac{Hz^2}{EI} ds$$

By setting the sum of the horizontal deformations equal to zero ($h_{beam} + h_H = 0$), an approximated value for the horizontal thrust is obtained. The shortening of the arch and translation are not taken into account.

The shortening of the arch can be evaluated via Hooke's law. When neglecting the influence of bending moments, the shortening of a cable can be used:

$$\Delta L = -\frac{H}{EA} \int_{x=0}^{x=l} \left\{1 + \left(\frac{dz}{dx}\right)^2\right\} dx = \frac{Hl}{EA} + \frac{H}{EA} \int_{x=0}^{x=l} \left(\frac{dz}{dx}\right)^2 dx$$

For example, when analysing a parabolic arch with a uniform distributed load, evaluating the integral will lead to [Wel12]:

$$\Delta L = -\frac{Hl}{EA}\left(1 + \frac{16}{3}\left(\frac{f}{l}\right)^2\right)$$

For the rise and span as used in the design of the approach bridge ($f = 5.75\ m, l = 42.5\ m$), this leads to an increase of 9.8% compared to a straight member with the same normal force, length and cross-section. Thus for shallow arches, the last term can be neglected:

$$\Delta L = -\frac{Hl}{EA}$$

Flexibility of the horizontal support can be taken into account via the spring stiffness.

$$h_k = \frac{H}{k_{support}}$$

The horizontal displacement of the support:

$$h_{support} = h_{beam} + h_H + \Delta L = -\int_{arch} \frac{M_{beam}\, z}{EI} ds - \int_{arch} \frac{Hz^2}{EI} ds - \frac{Hl}{EA} = \frac{H}{k_{support}}$$

The thrust of the two hinged system is then solved.

$$H = -\frac{\int_{arch} \frac{M_{beam}\, z}{EI} ds}{\int_{arch} \frac{z^2}{EI} ds + \frac{l}{EA} \cdot \alpha + \frac{1}{k_{support}}}$$

In which α may take the rise of the arch into account in the shortening of the arch.

For shallow arches, the arch length and the horizontal length are almost equal. In those cases the classical arch formula is obtained by replacing 'ds' by 'dx', allowing no translation of the support ($k_{support} \rightarrow \infty$) and applying $\alpha = 1$.

$$H = -\frac{\int_{arch} \frac{M_{beam}\, z}{EI} dx}{\int_{arch} \frac{z^2}{EI} dx + \frac{l}{EA}}$$

Sensitivity to support stiffness

Both the shortening due to compressive strain and the flexible horizontal support conditions, lead to a lower horizontal thrust when stiffness decreases. In the graph (Figure 44) the horizontal thrust is plotted as a function of only the support stiffness. The red line indicates the horizontal thrust in case no displacement of the support occurs and axial deformation is neglected.

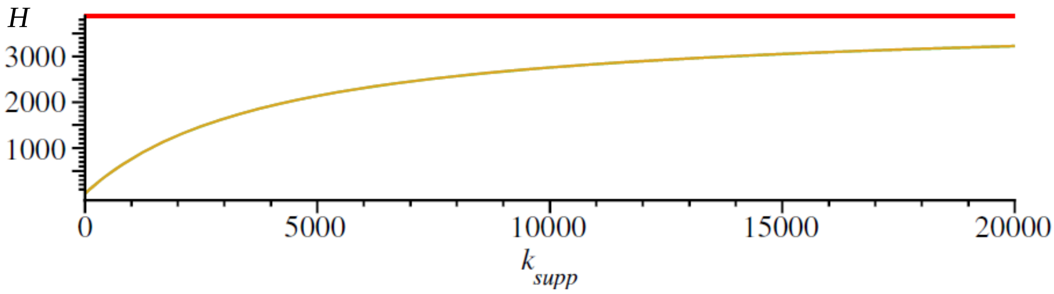

Figure 44: Influence support stiffness on horizontal thrust (span 42.5 m rise 5.75 m and load 100kN/m)

11.1.3 One hinged and hingeless arches

As previously described, the two hinged arch is simply statically undetermined. One unknown variable can be solved by the classical arch formula. The other (three) unknown variables form a statically determined structure, which can be solved by the equilibrium equations.

Arches with one hinge or hingeless arches are multiple statically undetermined structures. Applying the classical arch formula is not possible, since unknown bending moments, which occur at the support, should be incorporated in M_{beam}. With one equation, it is impossible to solve multiple variables. Thus a different approach is required, to analyze these structures. A robust solution strategy for these structures can be found in the differential equations that describe beam and arch behaviour.

11.2 Members to compose the differential equations

11.2.1 Cable / Arch action

Already in 1675, Robert Hooke published an anagram in his book '*Description of Helioscopes*', which stated:

"Ut pendet continuum flexile, sic stabit contiguum rigidum inversum"

Which can be translated to: "As hangs the flexible line so, but inverted, will stand the rigid arch" [Kur08].

Cable and arch action are based on the same principle of load transfer via normal forces. The difference is the bending stiffness, which is theoretically only present in arches. Arch action without bending is described by the same differential equation as used for cable structures. The difference is the direction of the load q and the direction of the horizontal force H. The differential equation for a cable structure reads:

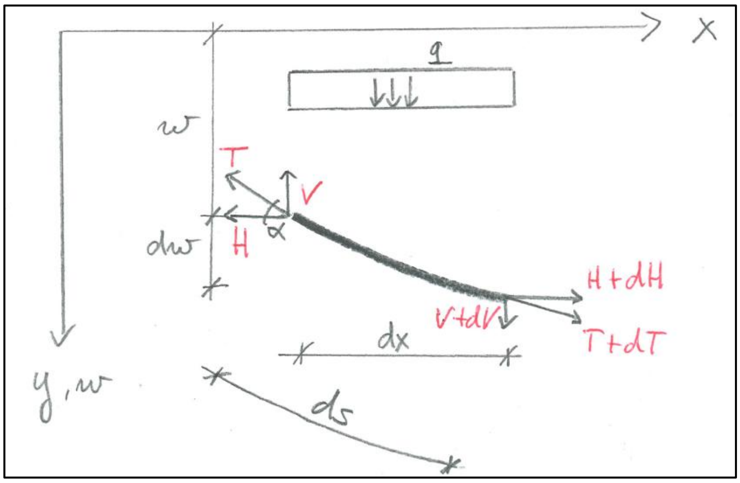

Figure 45: Model of cable action

Horizontal equilibrium: $-H + H + dH = 0 \;\rightarrow dH = 0 \quad \rightarrow\; H\ constant$

Vertical equilibrium: $\quad -V + V + dV + q \cdot dx = 0 \qquad \rightarrow q = -\frac{dV}{dx}$

Geometrical relation: $\quad V = H \cdot \tan(\alpha) = H \cdot \frac{dw}{dx}$

$$\boxed{H \cdot \frac{d^2w}{dx^2} = -q}$$

11.2.2 Euler-Bernoulli beam model

The beam model refers to the load carrying mechanism via bending. The assumptions in the Euler-Bernoulli model are the linear elastic material behaviour (application of Hooke's law), the assumption that plane cross-sections remain plane after deformation and cross-sections that are initially perpendicular to the beam axis remain perpendicular to the deformed beam axis.

From equilibrium follows, when higher order terms are neglected:

$$-V + V + dV + q \cdot dx = 0 \qquad \rightarrow q = -\frac{dV}{dx}$$

$$M - (M + dM) + (V + dV)dx + \frac{q \cdot dx^2}{2} = 0 \qquad \rightarrow V = \frac{dM}{dx}$$

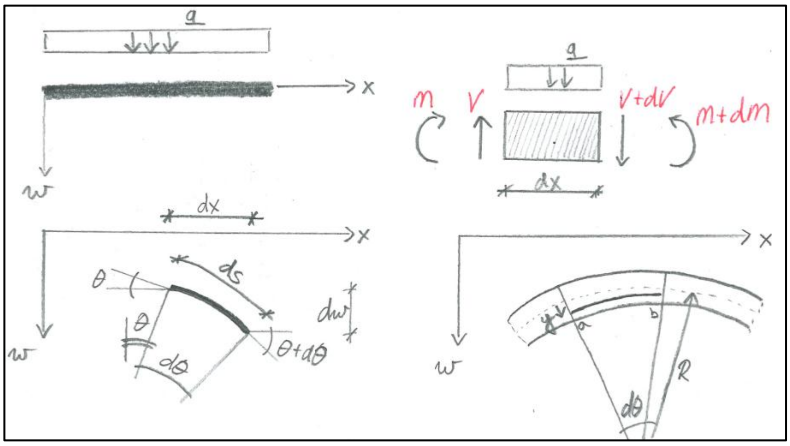

Figure 46: Model for beam action

The kinematic relations relate the curvature to the deformations:

$$ds = R \cdot d\theta \qquad \kappa = \frac{1}{R} = \frac{d\theta}{ds} \qquad \tan(\theta) = \frac{dw}{dx} \qquad ds = dx \cdot \cos(\theta)$$

When assuming small rotations:

$$\tan(\theta) = \frac{\sin(\theta)}{\cos(\theta)} \approx \frac{\theta}{1} = \theta \qquad ds = dx \cdot cos(\theta) \approx dx$$

$$\kappa = \frac{1}{R} = \frac{d\theta}{ds} \approx \frac{d\theta}{dx} \approx \frac{d^2w}{dx^2}$$

The link between kinematic and equilibrium equations is determined via the constitutive equations, in which the bending moment is linked to the curvature:

At the neutral axis: $dx = R \cdot d\theta$

Fibre at distance y to the neutral axis: $ds_{a-b} = (R - y) \cdot d\theta$

Strain of a fibre: $\varepsilon_{xx} = \frac{\Delta l}{l} = \frac{ds_{a-b} - dx}{dx} = -y\frac{d\theta}{dx} = -y \cdot \kappa$

Hooke's law: $\sigma_{xx} = E \cdot \varepsilon_{xx} = -E \cdot y \cdot \kappa$

Bending moment: $M = \int dM = \int \sigma_{xx} \cdot y \, dA = -E \cdot \kappa \int y^2 \, dA = -EI \cdot \kappa$

Combining: $q = -\frac{dV}{dx} \;\cap\; V = \frac{dM}{dx} \;\cap\; M = -EI \cdot \kappa \;\cap\; \kappa = \frac{d^2w}{dx^2}$

$$\boxed{EI \cdot \frac{d^4w}{dx^4} = q}$$

In case of a constant cross-section along the x-axis.

11.2.3 Geometrically Nonlinear

When deflections and rotations increase, several assumptions made in the derivation of the differential equation of the Euler-Bernoulli beam model are not valid anymore. In this paragraph the differences are shown. Source and further reading: [Fer99].

Equilibrium

The effect of large rotations on the equilibrium of a infinitely small beam part leads to different equilibrium equations, in which the rotation of the element is regarded and the load is divided in a part normal and parallel to the 't' axis.

$$\sum N = 0 \;\rightarrow\; -N + (N + dN)\cos(-d\theta) + (V + dV)\sin(-d\theta) + q_t\, ds = 0$$

$$\sum V = 0 \;\rightarrow\; +V - (V + dV)\cos(-d\theta) + (N + dN)\sin(-d\theta) + q_n\, ds = 0$$

$$\sum M = 0$$

$$-M + (M + dM) - (V + dV)ds + (N + dN)\left\{\sin(-d\theta)ds - \cos(-d\theta)\frac{1}{2}\, ds d\theta\right\} = 0$$

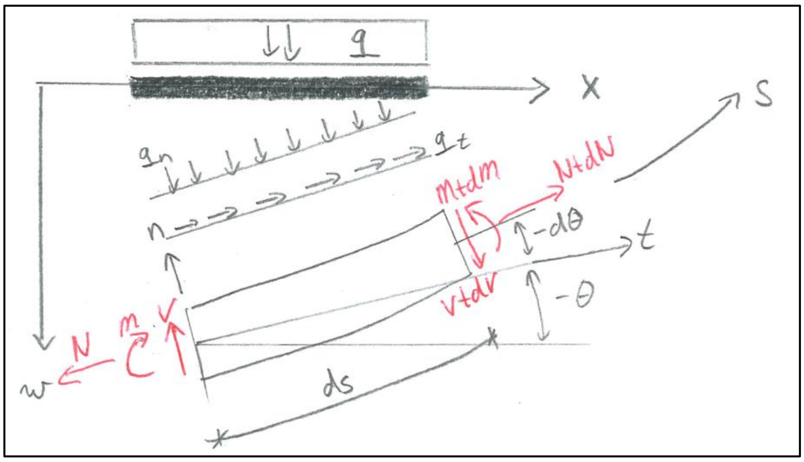

Figure 47: Nonlinear equilibrium

D.G. Fertis proposes in "Nonlinear Mechanics" to neglect the higher order terms $(dsd\theta)$. $d\theta$ is a small angle and therefore $\sin(d\theta) \approx d\theta \cap \cos(d\theta) \approx 1$. Also, the kinematic relation $\kappa = \frac{1}{R} = \frac{d\theta}{ds}$ is applied, which lead to:

$$\frac{dN}{ds} - \frac{V}{R} + q_t = 0 \qquad \frac{dV}{ds} + \frac{N}{R} + q_n = 0 \qquad \frac{dM}{ds} - V = 0$$

Similar to the Timoshenko beam model, this leads to a set of two differential equations which should be fulfilled simultaneously.

$$\begin{cases} \dfrac{dN}{ds} - \dfrac{dM}{ds} \cdot \dfrac{1}{R} + q_t = 0 \\[2ex] \dfrac{d^2M}{ds^2} + \dfrac{N}{R} + q_n = 0 \end{cases}$$

Constitutive relation

The constitutive law does not change ($M = -EI\kappa$), when it is assumed that even at large displacements, strains are still small and therefore the material behaves linear elastic.

Kinematic relation

In the kinematic relation small deformations assume $dx \approx ds$, $\Delta = L - l \approx 0$, $w' \ll 1$

The mathematical expression for the curvature of a line in two dimensional space:

$$\kappa = \frac{1}{R} = \frac{w''}{[1 + (w')^2]^{3/2}}$$

(in which the displacement w is differentiated with respect to x)

In case of small rotations, the term in the denominator is approximately 1, leading to the relation $\kappa = w''$, which is used in the Euler-Bernoulli beam model.

Differential Equations

When combining the nonlinear equilibrium and the mathematical expression for curvature, the following system of differential equations is obtained.

$$\begin{cases} \dfrac{dN}{ds} + EI\dfrac{d}{ds}\left\{\dfrac{w''}{[1 + (w')^2]^{3/2}}\right\} \cdot \left(\dfrac{w''}{[1 + (w')^2]^{3/2}}\right) + q_t = 0 \\ -EI\dfrac{d^2}{ds^2}\left\{\dfrac{w''}{[1 + (w')^2]^{3/2}}\right\} + N\left(\dfrac{w''}{[1 + (w')^2]^{3/2}}\right) + q_n = 0 \end{cases}$$

These equations will provide more detailed information, when these equations are solvable. However, as long as the Euler – Bernoulli assumptions are valid, the Euler – Bernoulli beam model is preferred, since it is less complicated to solve analytically. Therefore, the linearized Euler – Bernoulli model is applied in the investigation.

11.3 Differential Equations Arch

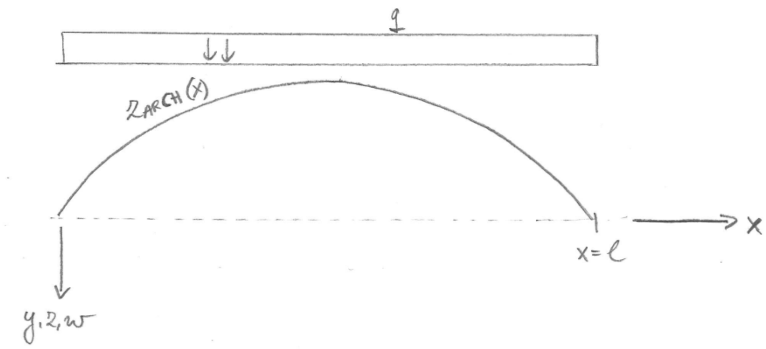

Figure 48: Axis system arch

The structural behaviour of an arch can be described by the combined system of a cable and a beam, in case the assumptions of the Euler-Bernoulli beam model are valid.
The differential equation for the arch according to [Bou89] is:

$$EI \cdot \frac{d^4 w}{dx^4} + H \cdot \frac{d^2(z+w)}{dx^2} = q(x)$$

In which 'z' defines the rise of the arch and 'w' represents its deformation. The differential equation is valid for arches that are supported during execution. A constant horizontal force is assumed as its increase is rather small. In geometrically nonlinear analysis, this cannot be neglected and therefore the differential equation is adapted to:

$$EI \cdot \frac{d^4 w}{dx^4} + (H + \Delta H) \cdot \frac{d^2(z+w)}{dx^2} = q(x)$$

11.3.1 Linearization (first order)

In most arches, the deflection is often much smaller than the rise of arch $(w \ll z)$ and when the arch deflects only little, the increase of the horizontal thrust is neglectable $(\Delta H \approx 0)$. Then the differential equation simplifies to:

$$EI \cdot \frac{d^4 w}{dx^4} + H \cdot \frac{d^2 z}{dx^2} = q(x)$$

Solving this differential equation (based on the boundary conditions) will lead to a displacement function that is depending on the thrust H. Analogous to the classical arch formula, the thrust can be determined by considering the translation of the support.

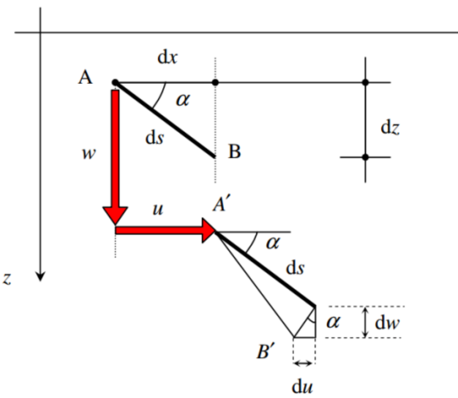

$$du = -\tan(\alpha) \cdot dw$$

$$\tan(\alpha) = \frac{dz}{dx}$$

$$du = -\frac{dz}{dx} \cdot dw$$

Figure 49: Translation u due to deformation w [Wel12]

Dividing both sides with dx and integrating once with respect to x gives:

$$u = -\int_0^l \frac{dz}{dx} \cdot \frac{dw}{dx}\, dx$$

In this formula, axial shortening and flexible supports can be accounted for via:

$$u = -\int_0^l \frac{dz}{dx} \cdot \frac{dw}{dx}\, dx = \frac{H}{k_{support}} + \frac{Hl}{EA}$$

The horizontal thrust (H) is the only unknown parameter in the formula and can be solved.

11.3.2 Geometrically nonlinear approximation for arches (second order)

In arched structures, bending moments provide the compatibility with the boundary conditions and the applied load (difference between thrust line and arch axis). Small differences in horizontal thrust and small deformations can lead to rather large variations in the bending moment distribution. Next to that, the deformations lead to a magnification of normal forces and bending moments which will increase the deformations again. This so called second order effect is neglected in linear calculation. For a more accurate description of the arch behaviour, the variation in the deflection and the thrust should be incorporated. In that case, the differential equations read:

$$EI \cdot \frac{d^4(w_1 + w_2)}{dx^4} + (H + \Delta H) \cdot \frac{d^2(w_1 + w_2)}{dx^2} + (H + \Delta H) \cdot \frac{d^2 z}{dx^2} = q(x)$$

In which a distinction is made for linear deflections (w_1) and the nonlinear $(w_2$, second order) deflections. The results from the linearized part can be subtracted, leading to

$$EI \cdot \frac{d^4 w_2}{dx^4} + (H + \Delta H) \cdot \frac{d^2(w_1 + w_2)}{dx^2} + \Delta H \cdot \frac{d^2 z}{dx^2} = 0$$

In this differential equation, the thrust and deflection as calculated in the linear analysis cause a mathematical second order load on the arch $(H \cdot w_1")$. There is no external loading $(q(x) = 0)$ in the second order analysis. The internal load is visualized in Figure 50 by the solid line, which represents the second derivative.

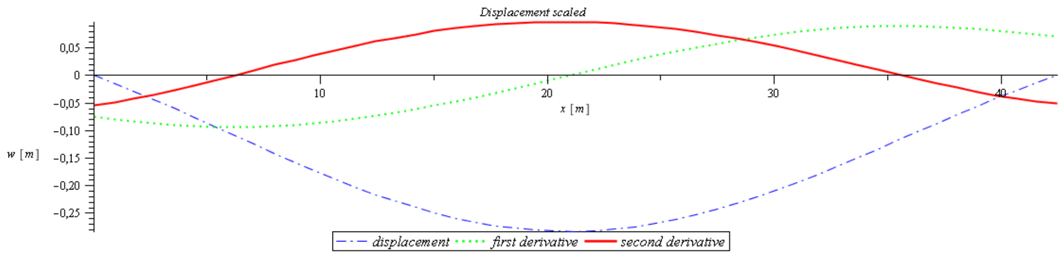

Figure 50: Displacement arch and two derivatives (not to scale, example with flexible supports)

The linear and nonlinear part lead to an analogous mathematical statement. Solving it will require the same steps. The differences are visible in the calculated parameters: $w(x, H)$ versus $w_2(x, \Delta H)$. Note that these differential equations do describe the basic structural behaviour of the system, but that these equations are based on the Euler-Bernoulli beam model, with the corresponding assumptions.

12. Analysis single arch

12.1 Analytical strategy

The analytical solution to the mathematical model is determined by using a Maple worksheet. Maple is an analytical mathematical software program. Solving the mathematical statement with the worksheet is a quick approach, once the worksheet is written. It thus enables investigation of multiple load cases and boundary conditions.

12.1.1 First order

Geometry

The circle shape can mathematically be described by: $z(x) = \sqrt{R^2 - \left(x - \frac{l}{2}\right)^2} - R + f$.
Integrating this will lead to complicated expressions, due to the quadratic function in the square root. A Taylor series expansion is a solution to this problem, since only polynomials are integrated. For smooth functions, like the arch axis, the approximation is quite accurate and it provides a good alternative in case it is not possible to integrate the exact function. The series is truncated after the 10^{th} term, based on a visual comparison of the two plots.

$$z(x) = -5.75 + 0.011865\,(x - 21.25)^2 + 1.67027 \cdot 10^{-6} \cdot (x - 21.25)^4 + 4.70262 \cdot 10^{-10} \cdot (x - 21.25)^6 + 1.65024 \cdot 10^{-13} \cdot (x - 21.25)^8 + 6.52359 \cdot 10^{-17} \cdot (x - 21.25)^{10}$$

Differential Equation and Boundary Conditions

The mathematical analysis starts with solving the differential equation to obtain the first order deformation (note the change of variables with respect to chapter 11.3, which is necessary for programming with Maple):

$$EI \cdot \frac{d^4W}{dx^4} + H \cdot \frac{d^2z}{dx^2} = q(x)$$

It will lead to a displacement function in which the four integration variables and the horizontal thrust have to be solved ($W(x, H, C1, C2, C3, C4)$). The integration constants can be solved with boundary conditions, after defining the bending moment and rotation $\left(M = -EI \cdot \frac{d^2W}{dx^2} \text{ and } \Phi = -\frac{dW}{dx}\right)$.

For example, two hinged supports:
At $x = 0$, $W(0) = 0$ and $M(0) = 0$
At $x = l$, $W(l) = 0$ and $M(l) = 0$

Other support conditions can be accounted for in the boundary conditions:
- Clamped supports ($\Phi = 0$)
- Flexible support (e.g. $C = M/\Phi = 500.000\ \mathrm{MNm/rad}$)
- Support settlement (e.g. $W(l) = 20\ \mathrm{mm}$)

Horizontal thrust

After solving the integration constants, the displacement function $W(x, H)$ is obtained, in which only the thrust has to be solved. Note that in computing the thrust H, translational flexibility of the support is taken into account. This flexibility is not modelled via the differential equation. The required formulae are given in paragraph 11.3.1.

First Order Results

Once the displacement and horizontal thrust are known, the force distributions (M, N, V) can be determined.

$$\alpha = \arctan\left(\frac{dz}{dx}\right) \qquad V_z = -EI\frac{d^3W}{dx^3} - H\frac{dz}{dx}$$

$$V = H\sin(\alpha) + V_z\cos(\alpha) \qquad N = -H\cos(\alpha) + V_z\sin(\alpha) \qquad M = -EI\frac{d^2W}{dx^2}$$

12.1.2 Second order

The next step is to include the second order effect. For this, the interaction between the thrust and the deformation should be incorporated. The differential equation in paragraph 11.3.2, when rewritten to the new variables (which are used in Maple), reads:

$$EI \cdot \frac{d^4(W+w)}{dx^4} + (H+h)\cdot\frac{d^2(W+w)}{dx^2} + (H+h)\cdot\frac{d^2z}{dx^2} = q(x)$$

To get rid of the abridged multiplication (the brackets), the equation is rewritten. Subtraction of the linear equation leads to (the apostrophes indicate differentiation with respect to the x-coordinate):

$$EI\cdot W'''' + EI\cdot w'''' + (H+h)\cdot W'' + (H+h)\cdot w'' + (H+h)\cdot z'' = q(x)$$

$$\underline{EI\cdot W'''' + \qquad\qquad\qquad\qquad H \quad \cdot z'' = q(x) \qquad -/-}$$

$$EI\cdot w'''' + (H+h)\cdot W'' + (H+h)\cdot w'' + \qquad h\cdot z'' = 0$$

In this differential equation the bending term $EI\cdot w''''$ and the arch term $h\cdot z''$ combine to an upward pressure. This should be in equilibrium with the downward 'load' that is caused by the other terms $(H+h)\cdot W''$ and $(H+h)\cdot w''$. When neglecting the second term of this load (w''), the differential equation simplifies to:

$$EI\cdot {w_1}'''' + (H+h_1)\cdot W'' + h_1\cdot z'' = 0$$

Note that new second order variables are introduced ($w_1, h1$) which are different from the actual second order deformation (w) and thrust (h). This differential equation is mathematically analogous to the linear differential equation ($EI\cdot W'''' + H\cdot z'' = q$). The parameters which are to be solved are w_1 and h. However, neglecting part of the imaginary second order load, will lead to an underestimation of the second order internal forces.

A solution to this underestimation can be found in dividing the second order deformation in a series:

$$w_{second\ order} = w_1 + w_2 + w_3 + w_4 + \ \ldots\ldots$$

The displacement w_1 is caused by the deformation W and the horizontal thrust $(H+h)$. The next step is to apply an imaginary load, based on ${w_1}''$. Since this load will lead to an increase in horizontal thrust and an increase in deformation, parameters $h2$ and w_2 are defined. The calculated deformation w_2 can then be used as the loading $(w_2{}'')$ to compute iteratively the internal forces as a result of the second order effect.

The total displacement and thrust are defined as:

$w_{total} = W + w_1 + w_2 + w_3 + \ldots\ldots$
$H_{total} = H \ + \ h_1 \ \ + h_2 + h_3 + \ldots\ldots$

<u>*Overview of the analysis*</u>

Analysis – step 1:
$EI \cdot W'''' + \qquad\qquad\qquad\qquad H \cdot z'' = q(x)$

Analysis – step 2:
$EI \cdot w_1{}'''' + (H + h_1) \cdot W'' + \qquad\qquad h_1 \cdot z'' = 0$

Analysis – step 3:
$EI \cdot w_2{}'''' + (H + h_1 + h_2) \cdot w_1{}'' + \qquad\qquad h_2 \cdot z'' = 0$

Analysis – step 4:
$EI \cdot w_3{}'''' + (H + h_1 + h_2 + h_3) \cdot w_2{}'' + \qquad h_3 \cdot z'' = 0$

Summing the above displayed differential equations, will show a deviation from the original differential equation. The terms that are missing (without the truncation error) are:

$(h_2 + h_3) \cdot W'' \quad / \quad h_3 \cdot w_1{}''$

In analysis step 3, the term $h_2 \cdot W''$ is added and in analysis step 4 the other terms $h_3 \cdot (W'' + w_1'')$ are added.

Solving problems iteratively requires numerical stability or convergence. Each next iteration should yield results that are an order of magnitude smaller compared to its previous iteration. In the MAPLE worksheet, each iteration step is programmed manually. In the second iteration of the nonlinear part, a relatively low increase in horizontal thrust was found, $h_2 < 20$ kN for the hinged and clamped supports. Since in linear analysis values for H of about $30{,}000$ kN are computed, truncating the analysis after this second iteration seems reasonable. However, the flexible supports with low support stiffness yields h_2 values larger than $1{,}000$ kN and thus requiring more iteration steps. It has been chosen to apply a third iteration step for all support conditions. Note that the differential equation neglects the horizontal deformations of the arch and will remain a poor model for low support stiffnesses, irrespectively of the number of iterations.

On the other hand, truncating the analysis should not be based on the increase in horizontal thrust solely. The increase of bending moments should converge too. As a small deviation in horizontal thrust causes a much larger deviation in the bending moments, due to the arch's rise. A small example will illustrate this effect:

For the Nijmegen city bridge (rise $f = 5{,}75\ \mathrm{m}$), assuming the horizontal thrust has values in the order of 35,000 kN *and the bending moment at midspan has values in the order of 6,000* kNm*.*

An underestimation of 1% with respect to the horizontal thrust, will lead to an increase in the calculated bending moment of:

$$0.01 \cdot 35{,}000 \cdot 5.75 = 2{,}012\ \mathrm{kNm}$$

Which means an increase of 33.5%. This illustrating the importance of a correct computation of the horizontal thrust.

The results of the second order analysis (normal forces, shear forces, bending moments and deformations) are only due to the second order “loading” effect. These results should be summed with the first order results to obtain the total result.

The bending moment magnification can be found via:

$$M = -EI \cdot \frac{d^2W}{dx^2}\ ,\ \ m = -EI \cdot \frac{d^2(w_1 + w_2 + w_3 + ..)}{dx^2}\ ,\ \ magnification = \frac{M+m}{M}$$

12.2 Finite Element Analysis by Scia Engineer

To compare the analytical results with a numerical computation, the structure is modelled in the finite element program Scia Engineer. Whereas finite element programs are often written for mechanics and academic research, Scia Engineer was developed with focus to practical use in the construction industry. Therefore, code checking of cross-sections is implemented in the post-processing and the mesh generation is automated to a high degree, to name some examples. The program requires only basic knowledge in computational mechanics for structural analysis. Consequentially, there are a lot of default settings in the program, which is convenient in most cases, but it may lead to erroneous output, most probably, in exceptional cases. Therefore, a small overview of the program’s characteristics is given, source: [Sci10] and [Sme07].

12.2.1 Elements, nodes and degrees of freedom

Basically, two element types are implemented in Scia Engineer, beam elements and shell elements. Other elements, like wall elements (only normal forces), are deduced from these elements. Both beam elements and shell elements have nodes with six degrees of freedom and both elements use linear interpolation polynomials. Beam elements and shell elements can thus be connected without compatibility problems. Translations u_x, u_y and u_z and rotations φ_x, φ_y and φ_z determine the internal forces in beams (N, V_y, V_z, M_x, M_y and M_z) and plates ($m_x,\ m_y,\ m_{xy},\ v_x.\ v_y,\ n_x,\ n_y$ and n_{xy}). Solid elements are not incorporated.

The beam elements are linear elements with two nodes. Although curved shapes can be modelled easily (circles, parabolas, splines and Bezier curves are implemented), only the nodal coordinates coincide with these curves. The finite elements will be straight. Shear stiffness is taken into account in the deformations (Timoshenko beam model), which might be neglected optionally (Euler – Bernoulli beam model). The interpolation for the displacements along the local x-axis is linear for u_x and cubic for u_y and u_z. For the rotations ($\varphi_x, \varphi_y, \varphi_z$), a quadratical interpolation is used. The internal forces are calculated analytically (e.g. $M_x = \int \sigma_x \cdot z \, dz$) in the integration points. These results are linearly extrapolated over the element length. To model curved structures with beam elements, the mesh fineness is the paramount variable in obtaining good representation of the continuous model, since too large mesh sizes will not follow the continuous curved shapes well.

When reviewing the finite element mesh of a model with shell elements (or membrane-bending elements), the elements seem to be quadrilateral with four nodes and thus 24 degrees of freedom. Nevertheless, during analysis, the quadrilaterals will be constructed out of four triangular sub elements, which share a fifth node that will be inputted by the program. The location of the fifth node is defined as the intersection of the two lines that connect the midpoints of two opposite lines of the quadrilateral (Figure 52). This definition has the benefit that in case the quadrilateral becomes a triangle (three nodes in line), no singularity problems are encountered. For the shell elements, both Mindlin and Kirchhoff plate bending theories can be chosen. For thick plates, the shear deformation influences the structural behaviour and the Mindlin theory should be applied (including twisting bending moment decreasing to zero at free edges, implying an increasing shear force at these edges, Figure 51, [Bla10]). The Kirchhoff theory does not account for the shear deformations. For thin plates Kirchhoff and Mindlin can be used, the results will be quite similar. The Kirchhoff theory requires finite elements with sizes about plate thickness or larger. While for the Mindlin theory, a mesh refinement is necessary near the edges to obtain the correct output. As a rule of thumb, five elements should be applied in the edge zone to model the edge effect when using Mindlin theory. The width of the edge zone is about plate thickness.

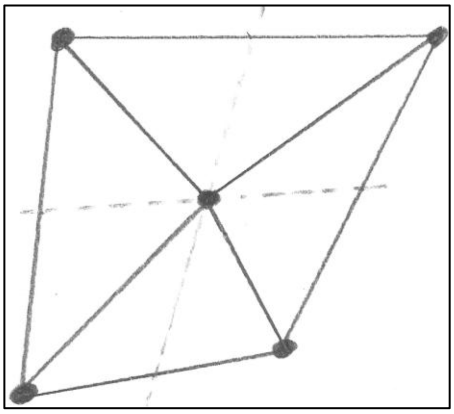

Figure 52: Shell element lay out

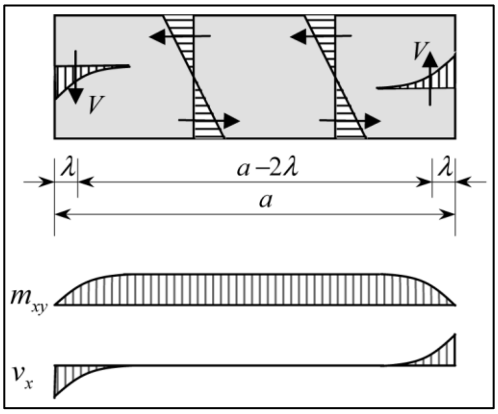

Figure 51: Mindlin theory for thick plates

The membrane (plane stress) effect is calculated with three degrees of freedom, u_x, u_y and φ_z. The displacement field is interpolated quadratically and thus strains vary linearly in the elements. Bending and shear forces are linked with degrees of freedom u_z, φ_x and φ_y, in which the displacements u_z in the plane finite element coordinates are interpolated quadratically too. The rotations φ_x and φ_y are interpolated linearly. Like the beam elements, the internal forces in shells are computed analytically and the elements are plane too. Internal forces are computed in the integration points, linearly interpolated and presented in the nodes. So again, for curved surfaces a sufficiently dense mesh is required to approximate the curves by plane elements.

12.2.2 Analysis

The solver determines the nodal displacements of the finite element model, by solving the system of equations $\boldsymbol{K} \cdot u = f$ (in which $\boldsymbol{K}$ is the stiffness matrix, vector f represents the loading and vector u are the nodal displacements). In elementary linear algebra, these problems are solved with Gaussian elimination (row reduction) or via the pre-multiplication with inverse stiffness matrix ($u = \boldsymbol{K^{-1}} \cdot f$). For large stiffness matrices (its size is approximately six times the number of nodes), there are faster methods. In Scia Engineer, two solvers can be chosen for the linear analysis, a direct and an iterative solver.

The direct solver determines the nodal displacements according to the Cholesky decomposition, in which the stiffness matrix is decomposed into the product of a lower triangular matrix and its conjugate transpose matrix. The nodal displacements are computed via substitution. The algorithm can solve so called multiple right-hand side equations, for example $\boldsymbol{K} \cdot \boldsymbol{U} = \boldsymbol{F}$. In structural engineering this means that in a single analysis run, multiple load cases are evaluated. Compared with the single right-hand side methods, it requires more computational capacity in terms of RAM (random access memory), but it is an efficient (fast) algorithm. When RAM disk space is insufficient, the solver will split the problem in parts, write the data to the computer's hard disk and solves first the single parts and then composes the solution out of these solved parts. Since writing to the hard disk is a much slower process than to the RAM, analysis time increases largely.

The iterative solver should be used when the direct solver is not functioning properly, due to low RAM capacity or numerical instability. The iterative solver is based on the Incomplete Cholesky conjugate gradient method. The method is based on an approximate decomposition (Incomplete Cholesky), which preconditions the stiffness matrix. Then the problem is solved by a numerical, iterative algorithm (conjugate gradient method), which will be truncated when the force convergence norm is reached. It is capable of solving only one right-hand side during an analysis. The methods benefits are the much lower required RAM size and its ability to solve with higher accuracy for ill-conditioned matrices (determinant approximately zero). Compared with the direct solver, the iterative solver is faster when models are large and there are only few load cases.

Nonlinear analysis

Several nonlinearities that occur in structures have to be taken into account in the structural analysis. The geometrically nonlinear behaviour is the main nonlinearity, in which equilibrium of forces is satisfied on the deformed structure. Nonlinear material behaviour, support nonlinearity and initial deformations can be modelled too. Nonlinear analysis is carried out via several linear analyses. The different solution procedures that can be chosen for the nonlinear analysis are Timoshenko, Newton-Raphson, Modified Newton-Raphson and Picard. For all solvers, convergence is checked based on the increase of displacements, see paragraph 12.2.3.

The Timoshenko solver determines the normal force distribution prior to the nonlinear analysis. Therefore, no load increments are possible and normal forces will maintain constant during nonlinear analysis. The solver uses the secant stiffness method (Figure 53), in which the stiffness matrix is iteratively adjusted and analysis is repeated until the convergence norm is reached. Assumptions in the Timoshenko algorithm are small displacements, small rotations and small strains.

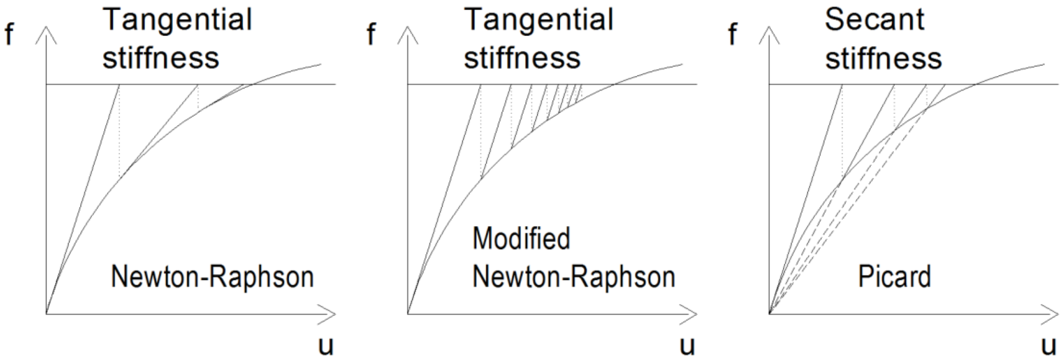

Figure 53: Nonlinear load-deflection curves, secant and tangential stiffness analysis methods

The Newton-Raphson solver uses the tangential stiffness and modifies the stiffness matrix in each iteration. Loads can be applied incrementally, varying normal forces are taken into account and large deformations can still be analysed. Drawbacks of the Newton-Raphson method is that it might not find numerical equilibrium when the approaching the top of the load deflection diagram and it is slower than the Timoshenko solver.

Modified Newton-Raphson is a variant to the Newton-Rapshon algorithm. The method uses the tangential stiffness, but it does not update the stiffness matrix in each iteration. It uses the tangential stiffness of the first iteration until convergence is reached in a load increment. Furthermore, in case critical points are reached, the program reduces the magnitude of the load increment and recalculates the stiffness matrix . A refinement of the increment step size at critical points cannot be inputted manually in the program. When using the Newton-Raphson solver, this local refinement is not possible in Scia Engineer. Although the total number of increments can be increased for smaller step sizes, this is a less convenient strategy, since most structures behave approximately linear for the lower loads.

Like the Timoshenko method, the Picard solver uses the secant stiffness method to find the nodal displacements. Nevertheless, the Picard method provides more accurate results. Normal forces may vary and large displacements can be analysed. The Picard solver might be an alternative to the Newton-Raphson methods, in case these methods do not reach convergence, but the Picard is a slower algorithm.

12.2.3 Arch model thesis

The applied model will be described in paragraph 13.1. For the arch, (linear) beam elements with an average mesh size of 250 mm are used. Since normal forces are variable in arch analysis, the Timoshenko solver should not be employed. Since no critical points will be met (except in case the load will be highly increased or the cross-section decreased), the other solvers could be used (Newton-Raphson, Modified Newton-Raphson and Picard). A quick check of the three solvers led indeed to similar results. The Newton-Rapshon solver is used for the analyses, since it is the fastest solver, according to the program's manual. The load is applied in 10 increments with a convergence norm of 0.001, which can be adapted in Scia Engineer via the solver precision ratio:

$$\frac{\sum\left({u_{x,i}}^2+{u_{y,i}}^2+{u_{z,i}}^2\right)-\sum\left({u_{x,i-1}}^2+{u_{y,i-1}}^2+{u_{z,i-1}}^2\right)}{\sum\left({u_{x,i}}^2+{u_{y,i}}^2+{u_{z,i}}^2\right)}\leq\frac{0.005}{precision\;ratio}$$

13. Solving the differential equations

13.1 Model

The theory in chapter 11 and 12 is used to investigate the geometrically nonlinear behaviour of the single arch, which is modelled (Figure 54) in Scia Engineer. The same parameters are applied in the analytical model. Although several load cases and boundary conditions are investigated, for the arch geometry, only the dimensions according to the city bridge design are considered in this chapter. Span $42.5\ \mathrm{m}$, rise $5.75\ \mathrm{m}$, width $25\ \mathrm{m}$, height $500\ \mathrm{mm}$. In chapter 15, different geometries are investigated.

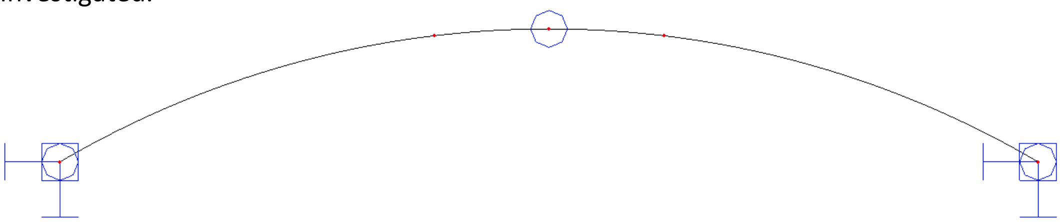

Figure 54: Single arch model

13.1.1 Supports (boundary conditions)

Two basic support conditions are investigated, the hinged support and the clamped support, in which translation of the supports is not allowed. A more realistic model for the foundation or substructure is a flexible support with rotational and translational stiffness. To agree with the analytical model, only one support is modelled with the translation flexibility. The support stiffness is estimated, based on comparable internal forces between the city bridge and the single arch model. Important aspect in the estimation is the fact that a single arch is different from a series of arches next to each other, since in the latter case, an arch is supported by adjacent arches. Since no exact representation of the city bridge model can be achieved with the single arch model, it makes no sense to fine tune the support stiffnesses. To investigate the influence in more depth, lower and higher stiffnesses are assumed:

$C_{low} = 100\ \mathrm{MNm/rad}$ and $k_{low} = 50\ \mathrm{MN/m}$ *(Flexible low)*
$C = 500\ \mathrm{MNm/rad}$ and $k = 200\ \mathrm{MN/m}$ *(Flexible)*
$C_{high} = 1{,}000\ \mathrm{MNm/rad}$ and $k_{high} = 400\ \mathrm{MN/m}$ *(Flexible high)*

In Scia Engineer, a third support is required to avoid rigid body rotation around the x-axis, since the two dimensional arch (a line) is modelled in a three dimensional space.

13.1.2 Material stiffness

Concrete C35/45 is used for the arches in the city bridge. The material has a Young's modulus $E_{cd} = 34{,}000\ \mathrm{N/mm^2}$ and when creep is taken into account (100 years, $\varphi = 1.558$) the elasticity reduces to $E_{cd,eff} = 13{,}292\ \mathrm{N/mm^2}$. However, the Young's modulus is used for a homogenous and linear elastic cross-section. The amount of reinforcement and cracking should be modelled via a fictitious Young's modulus. As a rule of thumb, $1/3$ of the original stiffness can be used ($E_f = 11{,}333\ \mathrm{N/mm^2}$).

In case a higher accuracy is required, estimation formulae (for example the formulae provided in table NB-1 of the Dutch national annex to Eurocode 2 (EN1992-1-1), see Table 11), bending moment – curvature (M-N-κ) diagrams (Figure 55) or a physically nonlinear finite element analysis can be utilized. Note that a physically nonlinear analysis requires all reinforcement to be modelled and after cracking, internal forces and deformations should match the nonlinear material behaviour, requiring high computer capacity and long computation time.

Table 11: Fictitious Young's modulus for combined bending and normal forces (NEN-EN-1992-1-1+C2:2011/NB:2011 - paragraph 5.8.5 - table NB-1)

beton-sterkte-klasse	buiging en normaalkracht symmetrisch gewapende rechthoekige doorsnede	
	$\alpha_n \leq 0{,}5$	$0{,}5 \leq \alpha_n \leq 0{,}9$
C20/25	$1600 + 420\,000\,\rho + (14\,000 - 160\,000\,\rho)\,\alpha_n \geq 3600$	$(12\,900 + 510\,000\,\rho)\,(1 - {}^2/_3\,\alpha_n)$
C25/30	$1750 + 425\,000\,\rho + (16\,500 - 175\,000\,\rho)\,\alpha_n \geq 3950$	$(15\,000 + 506\,000\,\rho)\,(1 - {}^2/_3\,\alpha_n)$
C30/37	$1960 + 432\,000\,\rho + (20\,000 - 196\,000\,\rho)\,\alpha_n \geq 4450$	$(17\,900 + 501\,000\,\rho)\,(1 - {}^2/_3\,\alpha_n)$
C35/45	$2200 + 440\,000\,\rho + (24\,000 - 220\,000\,\rho)\,\alpha_n \geq 5000$	$(21\,300 + 495\,000\,\rho)\,(1 - {}^2/_3\,\alpha_n)$
C45/55	$2500 + 450\,000\,\rho + (29\,000 - 250\,000\,\rho)\,\alpha_n \geq 5700$	$(25\,500 + 487\,500\,\rho)\,(1 - {}^2/_3\,\alpha_n)$
		$0{,}5 \leq \alpha_n \leq 0{,}8$
C55/67	$2860 + 462\,000\,\rho + (34\,600 - 258\,000\,\rho)\,\alpha_n \geq 6400$	$(29\,200 + 480\,000\,\rho)\,(1 - {}^3/_6\,\alpha_n)$
C70/85	$3100 + 470\,000\,\rho + (41\,500 - 170\,000\,\rho)\,\alpha_n \geq 6400$	$(29\,800 + 481\,000\,\rho)\,(1 - {}^2/_5\,\alpha_n)$
C90/105	$3100 + 470\,000\,\rho + (51\,000 - 170\,000\,\rho)\,\alpha_n \geq 6400$	$(35\,750 + 481\,000\,\rho)\,(1 - {}^2/_5\,\alpha_n)$

waarin:

$$\rho = \frac{A_{st} + A_{sc}}{A_c} \qquad \alpha_n = \frac{N_{Ed}}{f_{cd}A_c + (A_{st} + A_{sc})f_{yd}}$$

A_{st} is het oppervlak van de wapening aan de meest getrokken of de minst gedrukte zijde.
A_{sc} is het oppervlak van de wapening aan de meest gedrukte zijde.

The mutual influence between the Young's modulus and the bending moments is a complicating mechanism. The higher the Young's modulus, the higher the bending moments that will be computed. After cracking, the stiffness decreases, leading to lower bending moments. A high Young's modulus is thus a safe approach, but might be too conservative.

Including the geometrically nonlinear behaviour, a lower Young's modulus leads to lower bending moments, but deformations will be relatively larger, increasing the second order bending moments.

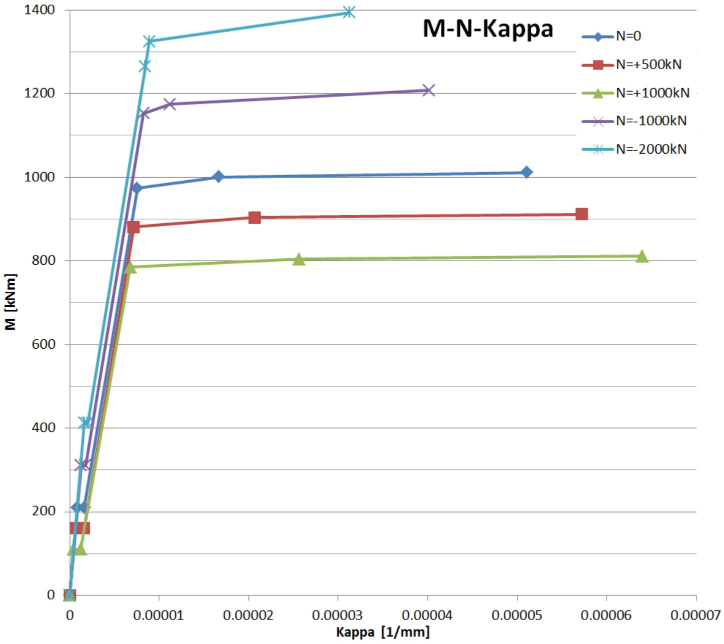

Figure 55: Bending moment - curvature relation for different normal forces

For the analyses, the fictitious stiffness is used. The derivation of this formula is based on the secant stiffnesses found in bending moment – curvature diagrams for instantaneous load combinations, including creep effects.

$$E_f = [2.20 + 440\rho + (24.0 - 220\rho)\alpha_n] \cdot 10^3 \geq 5000$$

In which ρ represents the reinforcement ratio and α_n is the ratio between the normal force due to loading and the plastic normal force capacity of the cross-section.

$$\rho = \frac{A_{st} + A_{sc}}{A_c} \qquad \alpha_n = \frac{N_{Ed}}{A_c\, f_{cd} + (A_{st} + A_{sc}) f_{yd}}$$

The fictitious stiffness is determined based on the cross-section $500 \times 25{,}000\ mm^2$, top and bottom reinforcement $ø32 - 150$, normal force $20{,}000\ kN$, $f_{cd} = 18.7\ N/mm^2$ and $f_{yd} = 435\ N/mm^2$.

Leading to a reinforcement ratio: $\rho = 0.0214$
And normal force ratio: $\alpha_n = 0.0571$

The fictitious Young's modulus: $\underline{E_f = 12{,}718\ \mathrm{N/mm^2}}$

The effect of the Young's modulus on the structural behaviour is investigated by using different values in the range $7{,}500\ \mathrm{N/mm^2}$ to $35{,}000\ \mathrm{N/mm^2}$, see paragraph 13.4.2. In part 4, the stiffness is determined with the M-N-κ relations, providing more detailed information on the fictitious Young's modulus. Due to time constraints, it was not possible to adapt the analyses in this part to the more detailed Young's moduli.

13.1.3 Geometrical Imperfections

Arches are slender structures. Imperfections, for example due to execution tolerances, will lead to additional bending moments in structural elements that are axially loaded. The most unfavourable imperfection for compressed columns is the buckling mode with the lowest buckling load, especially when it is affine with the first order deformation due tom transverse loading.

For arched structures, it should be kept in mind that the lowest buckling load is obtained in the anti-symmetrical buckling mode, while the deformation is symmetrical for a large part of the load. So both the lowest symmetrical and lowest anti-symmetrical buckling mode are considered.

Stability analysis only provides the shape of the buckling modes. Buckling analysis always encounters solutions in which one unknown (the amplitude of the deformations) remains unsolved. Rules for the amplitude of the geometrical imperfection that should be taken into account are provided in the codes (Eurocode NEN-EN 1992-2 art. 5.2 note (106)). The amplitude that should be taken into account is:

$$a = \theta_0 \cdot \frac{2}{\sqrt{l}} \cdot \frac{l}{2} = \frac{1}{300} \cdot \sqrt{l} = 0.022\ m$$

The first buckling mode is anti-symmetrical in most cases. It is modelled by a sine wave (Figure 56):

$$z_{asym} = \sqrt{R^2 - \left(x - \frac{l}{2}\right)^2} - (R - f) + 0.022 \cdot \sin\left(\frac{2\pi x}{l}\right)$$

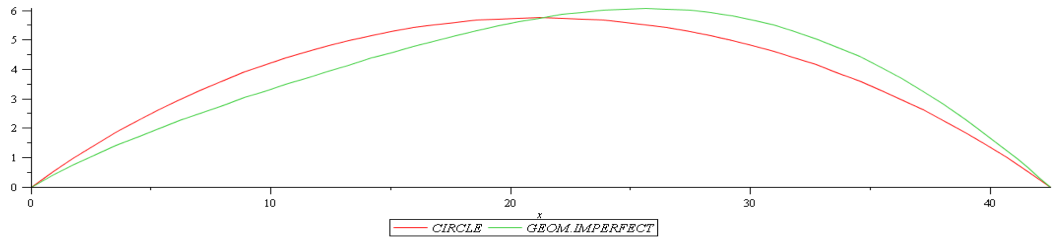

Figure 56: Anti-symmetrical geometrical imperfection (exaggerated amplitude)

The symmetrical buckling mode is modelled similarly.

$$z_{sym} = \sqrt{R^2 - \left(x - \frac{l}{2}\right)^2} - (R - f) + 0.022 \cdot \sin\left(\frac{3\pi x}{l}\right)$$

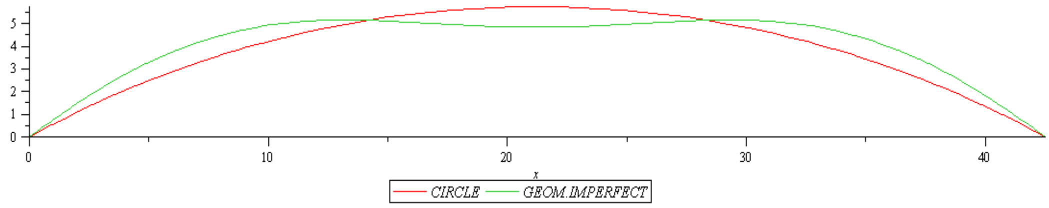

Figure 57: Symmetrical geometrical imperfection (exaggerated amplitude)

Which again can be expanded into a truncated Taylor series. Note that the Taylor series expansion will lead to good approximations for smooth functions only.

The investigated load cases are:

- Uniformly distributed load
- Non-uniform load
- Half span loaded
- Point loads
- Support settlements ($w = 20\ mm$)
- Geometrical imperfections (combined with distributed load and asymmetrical positioned point loads).

Next to these load cases, different cross-sectional heights, different Young's moduli and stepwise increasing load are investigated.

13.2 Results different loading patterns

The characteristic results of the analytical analysis and the Scia Engineer computations are displayed in the tables. All corresponding Maple worksheets and Scia Engineer output are added in the appendices.

13.2.1 Uniform load

A uniform load, $q(x) = 1{,}000\ kN/m$, is applied to the structure. The value is chosen based on the actual serviceability limit state load that varies between 660 and $1400\ kN/m$.

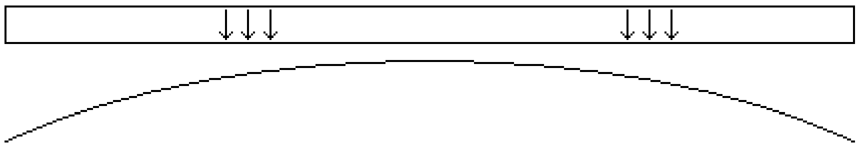

Table 12: **Uniform loading (bending moments and displacements at midspan)**

	Horizontal thrust H		Bending moment M		Displacement w	
	Linear	2nd order	Linear	2nd order	Linear	2nd order
Hinged	[kN]	[kN]	[kNm]	[kNm]	[m]	[m]
Analytical	-38,816	-38,981	2,596	3,468	0.0392	0.0470
Scia Engineer	-38,807	-38,951	2,643	3,678	0.0410	0.0513
Clamped						
Analytical	-39,385	-39,654	1,961	2,374	0.0315	0.0345
Scia Engineer	-39,392	-39,656	1,968	2,422	0.0326	0.0363
Flexible low						
Analytical	-34,437	-42,325	21,289	29,906	1.0396	1.3124
Scia Engineer	-34,479	-45,787	21,073	36,056	1.0460	1.6661
Flexible high						
Analytical	-37,620	-38,875	5,817	7,155	0.1840	0.1999
Scia Engineer	-37,680	-39,063	5,778	7,247	0.1857	0.2068

13.2.2 Non-uniform load

Permanent load and uniform distributed traffic load in serviceability limit state are considered. This load can be approximated by $q(x) = 660 + 1.64(x - 0.5 \cdot l)^2$.

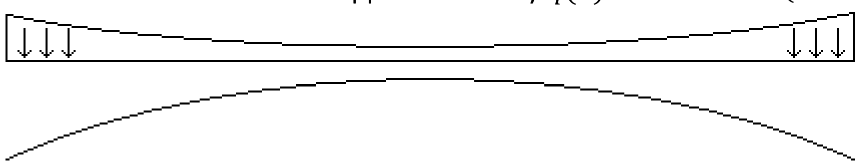

Table 13: **Non-uniform loading (bending moments and displacements at midspan)**

	Horizontal thrust H		Bending moment M		Displacement w	
	Linear	2nd order	Linear	2nd order	Linear	2nd order
Hinged	[kN]	[kN]	[kNm]	[kNm]	[m]	[m]
Analytical	-31,104	-31,133	-1,956	-2,518	-0.0079	-0.0128
Scia Engineer	-30,866	-30,919	-1,865	-2,494	-0.0070	-0.0125
Clamped						
Analytical	-30,183	-30,207	-927	-1,104	0.0046	0.0035
Scia Engineer	-30,027	-30,051	-898	-1,093	0.0050	0.0038
Flexible low						
Analytical	-27,480	-31,882	13,105	16,798	0.7922	0.9347
Scia Engineer	-27,305	-32,866	12,885	18,480	0.7871	1.0658
Flexible high						
Analytical	-29,473	-30,084	1,342	1,437	0.1149	0.1183
Scia Engineer	-29,299	-29,983	1,369	1,438	0.1151	0.1198

13.2.3 Half span loaded

Loading only half span, leads to high bending moments in arches. The uniform distributed load ($q = 1{,}000\ kN/m$) is investigated.

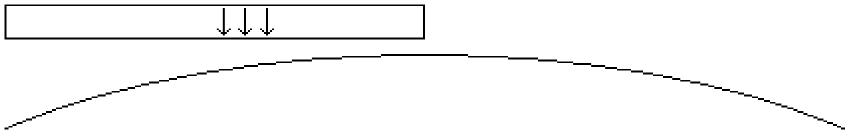

Table 14: Half span loaded (bending moments and displacements at 0.25 L)

	Horizontal thrust $\boldsymbol{H}$		Bending moment $\boldsymbol{M}$		Displacement $\boldsymbol{w}$	
	Linear	2nd order	Linear	2nd order	Linear	2nd order
Hinged	[kN]	[kN]	[kNm]	[kNm]	[m]	[m]
Analytical	-19,408	-19,448	27,721	38,067	0.4042	0.5486
Scia Engineer	-19,403	-19,192	27,603	42,500	0.4543	0.7619
Clamped						
Analytical	-19,693	-19,757	13,679	15,789	0.1641	0.1877
Scia Engineer	-19,696	-19,482	13,510	16,048	0.1832	0.2239
Flexible low						
Analytical	-17,218	-18,773	31,560	39,693	0.7111	0.8487
Scia Engineer	-17,240	-18,714	30,974	43,119	0.7687	1.0630
Flexible high						
Analytical	-18,810	-19,107	18,901	22,504	0.2875	0.3333
Scia Engineer	-18,840	-18,824	18,424	22,892	0.3131	0.3948

13.2.4 Tandem axle load

The Eurocode axle loading is considered (Loadmodel 1). Three axle systems of $100, 200$ and $300\ \mathrm{kN/axle}$, lead to two $600\ \mathrm{kN}$ point loads in the two dimensional model at a distance of $1.2\ \mathrm{m}$. Modelling point loads is a conservative approach, as the load spreads through the pavement and the backfill, An axle system can be anywhere on the bridge span. For the investigation, it is placed at a distance of $0.25\ l$ and $0.25\ l + 1.2$.

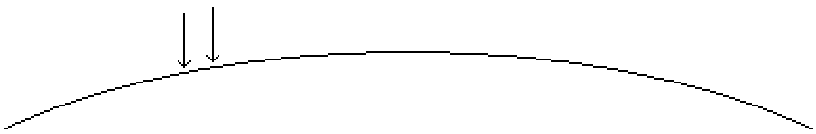

Table 15: Point loads (bending moments and displacements at 0.25 L)

	Horizontal thrust $\boldsymbol{H}$		Bending moment $\boldsymbol{M}$		Displacement $\boldsymbol{w}$	
	Linear	2nd order	Linear	2nd order	Linear	2nd order
Hinged	[kN]	[kN]	[kNm]	[kNm]	[m]	[m]
Analytical	-1,271	-1,271	3,803	3,852	0.0381	0.0387
Scia Engineer	-1,238	1,237	3,852	3,914	0.0432	0.0444
Clamped						
Analytical	-1,622	-1,262	2,635	2,651	0.0182	0.0183
Scia Engineer	-1,211	-1,209	2,766	2,786	0.0204	0.0206
Flexible low						
Analytical	-1,126	-1,131	4,013	4,051	0.0574	0.0580
Scia Engineer	-1,096	-1,100	4,011	4,102	0.0621	0.0632
Flexible high						
Analytical	-1,218	-1,219	3,057	3,079	0.0276	0.0278
Scia Engineer	-1,179	-1,178	3,142	3,169	0.0303	0.0307

13.2.5 Support settlement

A settlement of 20 mm is investigated, in accordance with the geotechnical analysis for the city bridge. It is combined with the uniform load. Hinged supports are not considered, since support settlement will not alter the force distribution. In Scia Engineer, the settlement is modelled via a flexible support.

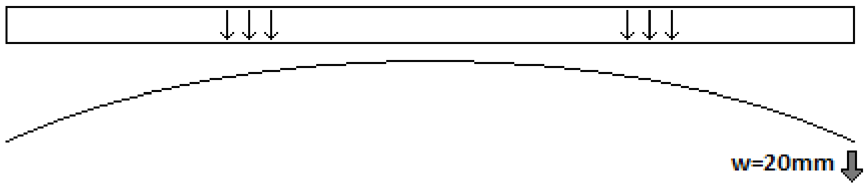

Table 16: Support settlement (bending moment at right support, displacement at midspan)

	Horizontal thrust H		Bending moment M		Displacement w	
	Linear	2nd order	Linear	2nd order	Linear	2nd order
Clamped	[kN]	[kN]	[kNm]	[kNm]	[m]	[m]
Analytical	-39,385	-39,654	2,854	3,351	0.0415	0.0445
Scia Engineer	-39,392	-39,658	1,968	2,423	0.0421	0.0458
Flexible low						
Analytical	-34,437	-42,325	6,453	7,432	1.0496	1.3224
Scia Engineer	-34,479	-45,787	6,418	9,378	1.0508	1.6707
Flexible high						
Analytical	-37,620	-38,875	3,511	2,757	0.1940	0.2098
Scia Engineer	-37,680	-39,063	3,211	2,485	0.1949	0.2161

13.3 Geometrical Imperfections

The geometrical imperfections that are taken into account are explained in paragraph 13.1.3. The anti-symmetrical imperfect shape is loaded by the half span load and the symmetrical imperfection is loaded over its full span. These combinations provide the most unfavourable situations.

13.3.1 Anti-symmetrical

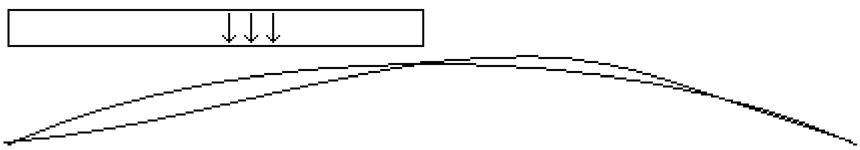

Table 17: Geometrical imperfections anti-symmetrical (bending moments and deformations at 0.25 L)

	Horizontal thrust H		Bending moment M		Displacement w	
	Linear	2nd order	Linear	2nd order	Linear	2nd order
Hinged	[kN]	[kN]	[kNm]	[kNm]	[m]	[m]
Analytical	-19,390	-19,449	28,227	38,754	0.4143	0.5625
Scia Engineer	-19,405	-19,183	27,607	43,420	0.4543	0.7841
Clamped						
Analytical	-19,650	-19,720	13,927	16,065	0.1681	0.1922
Scia Engineer	-19,696	-19,541	13,513	15,706	0.1832	0.2176
Flexible						
Analytical	-18,368	-18,862	22,376	27,133	0.3791	0.4440
Scia Engineer	-18,427	-18,561	21,469	27,995	0.4045	0.5328

13.3.2 Symmetrical

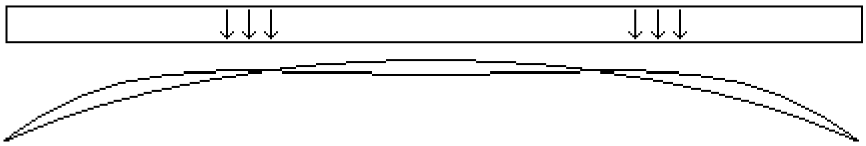

Table 18: Geometrical imperfections symmetrical (bending moments and displacements at midspan)

	Horizontal thrust H		Bending moment M		Displacement w	
	Linear	2nd order	Linear	2nd order	Linear	2nd order
Hinged	[kN]	[kN]	[kNm]	[kNm]	[m]	[m]
Analytical	-38,848	-39,035	3,460	4,611	0.0469	0.0573
Scia Engineer	-38,810	-38,997	2,626	4,614	0.0409	0.0606
Clamped						
Analytical	-39,598	-39,912	2,637	3,206	0.0367	0.0408
Scia Engineer	-39,394	-39,831	1,952	3,157	0.0325	0.0418
Flexible						
Analytical	-36,876	-39,021	9,320	11,708	0.3258	0.3611
Scia Engineer	-36,852	-39,351	8,478	11,690	0.3196	0.3764

13.4 Results different arch stiffnesses

The influence of the member stiffness of the arch is investigated, based on the model with the non-uniform load and flexible supports.

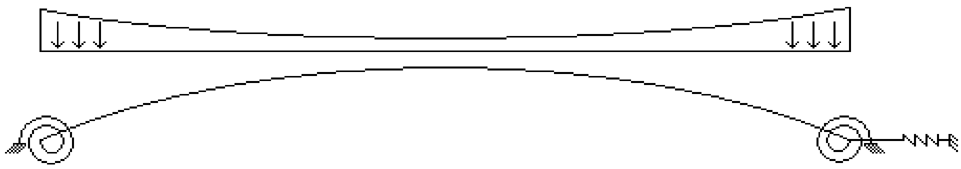

13.4.1 Cross-sectional height

Table 19: Different heights (bending moment at sagging maximum, displacement at midspan)

	Horizontal thrust H		Bending moment M		Displacement w	
	Linear	2nd order	Linear	2nd order	Linear	2nd order
h = 350 **mm**	[kN]	[kN]	[kNm]	[kNm]	[m]	[m]
Analytical	-27,719	-30,976	2,025	2,230	0.2170	0.2271
Scia Engineer	-30,338	-31,721	2,421	3,335	0.2143	0.2261
h = 450 **mm**						
Analytical	-29,284	-30,467	3,064	3,148	0.2200	0.2328
Scia Engineer	-29,933	-31,324	3,339	3,614	0.2202	0.2368
h = 600 **mm**						
Analytical	-28,513	-29,549	6,144	6,491	0.2135	0.2231
Scia Engineer	-29,182	-30,422	6,115	6,508	0.2169	0.2323
h = 750 **mm**						
Analytical	-27,509	-28,411	-11,566	-12,235	0.2042	0.2117
Scia Engineer	-28,184	-29,261	11,119	11,926	0.2087	0.2219

13.4.2 Young's modulus

Table 20: Different Young's moduli, (E in $[N/mm^2]$ bending moment and displacement at midspan)

	Horizontal thrust H		Bending moment M		Displacement w	
	Linear	2^{nd} order	Linear	2^{nd} order	Linear	2^{nd} order
E = 7,500	[kN]	[kN]	[kNm]	[kNm]	[m]	[m]
Analytical	29,386	30,636	-1,698	-1,995	0.2269	0.2411
Scia Engineer	30,029	31,482	-3,017	-3,347	0.2263	0.2432
E = 15,000						
Analytical	28,914	30,013	-3,906	-4,351	0.2160	0.2269
Scia Engineer	29,576	30,866	-4,533	-4,812	0.2182	0.2344
E = 25,000						
Analytical	28,395	29,394	-6,661	-7,194	0.2087	0.2175
Scia Engineer	29,066	30,264	-6,718	-7,152	0.2121	0.2267
E=35,000						
Analytical	27,927	28,858	-9,293	-9,893	0.2036	0.2114
Scia Engineer	28,600	29,718	-9,013	-9,630	0.2076	0.2210

Increasing the bending stiffness EI via both the Young's modulus or the cross-sectional height, will lead to slightly ($\sim 10\%$) lower displacements w and lower normal forces H. The translation at the supports depends on this horizontal thrust and thus decreases only little for higher bending stiffnesses. The arch' curvature due to the translation is approximately constant, leading to higher bending moments for higher bending stiffnesses, since $M = EI \cdot \kappa$.

13.5 Results increasing load

Based on the model with flexible supports and the non-uniform load, the influence of increasing load is investigated, since the second order effect is larger for higher loads. The non-uniform load is multiplied with factors varying between 0.5 and 10.

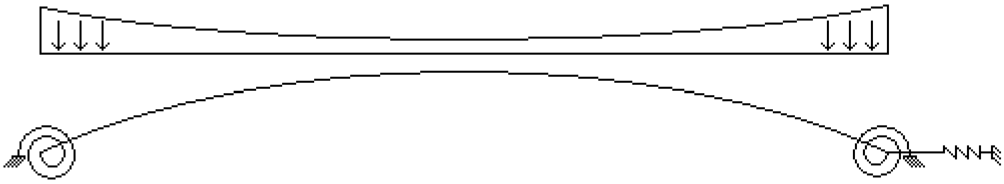

Table 21: Increasing load (bending moment and displacement at midspan)

	Horizontal thrust H		Bending moment M		Displacement w	
	1st order	2nd order	1st order	2nd order	1st order	2nd order
$q \cdot 0.5$	[kN]	[kN]	[kNm]	[kNm]	[m]	[m]
Analytical	-14,523	-14,794	1,626	1,718	0.1092	0.1119
Scia Engineer	-14,852	-15,170	1,373	1,434	0.1100	0.1139
$q \cdot 1.0$						
Analytical	-29,046	-30,178	3,252	3,668	0.2184	0.2300
Scia Engineer	-29,704	-31,049	2,745	3,031	0.2201	0.2368
$q \cdot 1.5$						
Analytical	-43,570	-46,241	4,878	5,943	0.3277	0.3557
Scia Engineer	-44,556	-47,775	4,118	4,881	0.3301	0.3710
$q \cdot 2.0$						
Analytical	-58,093	-63,093	6,504	8,674	0.4369	0.4909
Scia Engineer	-59,408	-65,549	5,491	7,165	0.4401	0.5205
$q \cdot 2.5$						
Analytical	-72,616	-80,881	8,130	12,046	0.5462	0.6382
Scia Engineer	-74,260	-84,692	6,863	10,302	0.5502	0.6925
$q \cdot 3.0$						
Analytical	-87,139	-99,795	9,756	16,315	0.6554	0.8010
Scia Engineer	*Error: Singular Stiffness-Matrix (buckling load (= $3.06q$) almost reached)*					
$q \cdot 4.0$						
Analytical	-116,186	-142,108	13,008	29,129	0.8739	1.1948
Scia Engineer						
$q \cdot 5.0$						
Analytical	-145,231	-193,469	16,260	52,212	1.0924	1.7394
Scia Engineer						
$q \cdot 7.5$						
Analytical	-217,848	-442,862	24,390	281,434	1.6385	5.4019
Scia Engineer						

Geometrically nonlinear theory is confirmed by this table. In first order analysis, the bending moments, normal forces and deformations increase linearly. In second order analysis, the results increase non-proportional when increasing the load, as can be seen by the increasing bending moment magnification factors in Table 22.

13.6 Bending moment magnification arches

13.6.1 Different loading patterns

In Table 22, the bending moment magnification factors are displayed for the models investigated in paragraphs 13.1.3 to 13.5. The factors are computed manually by dividing the second order bending moment by the first order bending moment. Note that these magnification factors vary along the arch axis (see paragraph 16.1) and that depending on the load, the bending moments are considered at mid span, at the support or at $0.25L$.

Table 22: Bending moment magnification factors - different loads and support conditions $E = 12,718$

Uniform Load	Analytical	Scia	Non-uniform load	Analytical	Scia
Hinged	1.34	1.39	Hinged	1.29	1.34
Clamped	1.21	1.23	Clamped	1.19	1.22
Flexible low	1.40	1.71	Flexible low	1.28	1.43
Flexible high	1.23	1.25	Flexible high	1.07	1.05
Half span load	**Analytical**	**Scia**	**Point loads**	**Analytical**	**Scia**
Hinged	1.37	1.54	Hinged	1.01	1.02
Clamped	1.15	1.19	Clamped	1.01	1.01
Flexible low	1.26	1.39	Flexible low	1.01	1.02
Flexible high	1.19	1.24	Flexible high	1.01	1.01
Geometrical imperfection - Anti-symmetr	**Analytical**	**Scia**	**Geometrical imperfection - symmetrical**	**Analytical**	**Scia**
Hinged	1.37	1.57	Hinged	1.33	1.76
Clamped	1.15	1.16	Clamped	1.22	1.62
Flexible	1.21	1.30	Flexible	1.26	1.38
Support settlements	**Analytical**	**Scia**	**Height**	**Analytical**	**Scia**
Clamped	1.17	1.23	h=350	1.10	1.38
Flexible low	1.15	1.46	h=450	1.03	1.08
Flexible high	0.79	0.77	h=600	1.06	1.06
			h=750	1.06	1.07
Young's moduli	**Analytical**	**Scia**	**Loads**	**Analytical**	**Scia**
E=7,500	1.17	1.11	0.5 q	1.06	1.04
E=15,000	1.11	1.06	1.0 q	1.13	1.10
E=25,000	1.08	1.06	1.5 q	1.22	1.19
E=35,000	1.06	1.07	2.0 q	1.33	1.30
			2.5 q	1.48	1.50
			3.0 q	1.67	-
			4.0 q	2.24	-
			5.0 q	3.21	-
			7.5 q	11.54	-

Different Young's modulus $E_f = 27{,}100\ N/mm^2$

After writing the MAPLE worksheets for the analytical geometrically nonlinear analyses, the obtained intermediate answers were compared with finite element models (Scia Engineer). In these 'quick checks', a (default) Young's modulus $E_f = 27{,}100\ \mathrm{N/mm^2}$ was applied. Erroneously this Young's modulus was not adapted in the analysis of the different load cases and support conditions. To match the results with the estimation formula, all analyses were repeated with the value $E_f = 12{,}718\ \mathrm{N/mm^2}$.

Since the erroneous analyses lead to a different data set, it is chosen to display briefly the magnification factors that were found in these analyses. The different magnification factors that were found, when only varying the Young's modulus, illustrate the theory. Increasing the Young's modulus lead to lower deformations and lower second order bending moments. Simultaneously, the bending moments (first order) increase for higher Young's moduli. Both effects lead to smaller bending moment magnification factors. To display the effect of the Young's modulus, the results of the analyses with the erroneous Young's modulus, are displayed in Table 23.

Table 23: Bending moment magnification factors - erroneous Young's modulus $E = 27,100$

Uniform Load	Analytical	Scia	Non-uniform load	Analytical	Scia
Hinged	1.14	1.15	Hinged	1.12	1.14
Clamped	1.09	1.09	Clamped	1.08	1.09
Flexible low	1.22	1.38	Flexible low	1.17	1.30
Flexible high	1.10	1.11	Flexible high	1.05	1.05
Half span load	**Analytical**	**Scia**	**Point loads**	**Analytical**	**Scia**
Hinged	1.15	1.20	Hinged	1.00	1.01
Clamped	1.07	1.08	Clamped	1.00	1.00
Flexible (avg.)	1.09	1.13	Flexible (avg.)	1.00	1.01
Geometrical imperfection - Anti-symmetr	**Analytical**	**Scia**	**Geometrical imperfection - symmetrical**	**Analytical**	**Scia**
Hinged	1.15	1.22	Hinged	1.13	1.45
Clamped	1.07	1.10	Clamped	1.09	1.44
Flexible (avg.)	1.09	1.15	Flexible (avg.)	1.11	1.18
Support Settlements	**Analytical**	**Scia**	**Height**	**Analytical**	**Scia**
Clamped	1.06	1.06	h=300	1.04	1.20
Flexible low	1.15	1.35	h=450	1.05	1.06
Flexible high	0.97	1.05	h=600	1.05	1.06
			h=750	1.04	1.06
			Loads	**Analytical**	**Scia**
			0.5 q	1.04	1.04
			1.0 q	1.08	1.09
			1.5 q	1.12	1.15
			2.0 q	1.17	1.22
			2.5 q	1.23	1.30
			3.0 q	1.31	1.41
			4.0 q	1.49	1.78
			5.0 q	1.74	-
			7.5 q	3.14	-

13.6.2 Differences analytical solution and Scia Engineer models

For most analysed load cases, the results computed by Scia Engineer and the analytical solution coincide really well. However, especially in case the stiffness of the flexible supports is low, larger differences are found in the results. It should be kept in mind that the geometrically nonlinear behaviour is accounted for in the arch action part of the differential equation, but the bending action is still based on the Euler-Bernoulli beam mode. In this model linear relations are assumed (Hooke's law and small rotations) in the derivation of the differential equation. For lower support stiffnesses, the deformations and rotations will be higher. The lower the support stiffness, the poorer the approximation of small rotations will be. The relation between deformation and curvature results in overestimated curvatures when the relation $\kappa = w''$ is used.
The exact form (paragraph 11.2.3) will lead to smaller curvatures (since the denominator: $[1 + (w')^2]^{3/2}$ is always larger than 1). Since the bending moments are based on the curvatures ($M = -EI\kappa$), the bending moments will be overestimated with respect to the deformations too.

Neglected term in arch shortening when determining horizontal thrust

Small deformations are assumed once more in the horizontal displacement of the arch, which will be visible when considering the arch length before and after loading [Wel12].

The arch length before loading (L) is given by:

$$L = \int_{x=0}^{x=l} ds = \int_{x=0}^{x=l} \sqrt{dx^2 + dz^2}\, dx = \int_{x=0}^{x=l} \sqrt{1 + \left(\frac{dz}{dx}\right)^2}\, dx \approx \int_{x=0}^{x=l} 1 + \frac{1}{2}\left(\frac{dz}{dx}\right)^2 dx$$

(the last term is a Taylor approximation)
Similarly, the length of the deformed arch (L^*) can be computed:

$$L^* - \frac{Hl}{EA} \approx \int_{x=0}^{x=l} 1 + \frac{1}{2}\left(\frac{d(z+w)}{dx}\right)^2 dx$$

Since both lengths should be equal ($L = L^*$)

$$\int_{x=0}^{x=l} \frac{1}{2}\left(\frac{dz}{dx}\right)^2 dx = \int_{x=0}^{x=l} \frac{1}{2}\left(\frac{d(z+w)}{dx}\right)^2 dx + \frac{Hl}{EA}$$

Which can be simplified to:

$$\int_{x=0}^{x=l} \frac{dz}{dx}\frac{dw}{dx}\, dx + \int_{x=0}^{x=l} \frac{1}{2}\left(\frac{dw}{dx}\right)^2 dx + \frac{Hl}{EA} = 0$$

When comparing the result with the formula in paragraph 11.3.1, it can be seen that the second term is neglected in the analysis. In case $dw/dx \ll dz/dx$ (small rotations) this approximation is justified. In case rotations are large, neglecting this term causes overestimation of the deflection and thus overestimation of bending moments.

Translation in x-direction

The most fundamental difference between the analytical model and the finite element model is the horizontal displacement, which is not a parameter in the analytical model (only vertical deformations), while in FE analysis it is taken into account. In the analytical model, the support stiffness only determines the magnitude of normal forces, whereas the nodes in the FE model do displace horizontally. The horizontal displacement curves the arch. The bending moments due to this curvature will carry part of the load and thus lower bending moments are to be expected in geometrically nonlinear finite element analysis.

However, in the analysis it appeared that for flexible supported arches with low support stiffness, the bending moments in FE analysis are larger than analytically determined in the geometrically nonlinear analysis, while in the linear calculation, the analytical method leads to the larger bending moments. For low support stiffnesses, the translation of the support reaches values between $0.4\ m$ and $0.75\ m$. The corresponding lowering of the arch crown, solely based on a circular arch with constant length, reaches values with order of magnitude of respectively $0.6\ m$ and $1.1\ m$. This lower rise of the arch will lead to larger normal forces and thus larger bending moments in geometrically nonlinear analysis. The bending moment magnification will be much larger in FE analysis since in linear analysis the bending moments are smaller, whilst in nonlinear analysis the bending moments are larger, compared with the analytical results.

For arches with low support stiffness, it should be concluded that a geometrically nonlinear finite element analysis will lead to more accurate results. However, basic principle in arch design is to ensure the confinement of the arch, to obtain large normal forces and small bending moments.

Geometrical imperfection

For the geometrical imperfection, large magnification factors are found in Scia Engineer. When using the buckling mode to model the geometrical imperfection, it will only be taken into account in the nonlinear analysis. To perform a stability analysis, a linear static analysis is required in advance. When calculating magnification factors, the magnification will include the geometrically nonlinear behaviour and the extra internal forces due to the imperfection. In the analytical model, the imperfection is applied in the arch elevation and thus incorporated in the linear analysis too. To evaluate the linear geometrically imperfect force distribution in the arch in Scia Engineer, the imperfect shape should be drawn, see Figure 50 and Figure 56. For a single arch, this is a realistic approach. In case several arches are considered, like the city bridge, drawing the imperfect shape is a too labour intensive for practical application. The symmetrical geometrical imperfection is manually drawn (as spline) in Scia Engineer for a single arch. The results are displayed in Table 24.

Table 24: Geometrical Imperfections symmetrical (bending moments and displacements at midspan)

	Horizontal thrust H		Bending moment M		Displacement w	
	linear	2nd order	linear	2nd order	linear	2nd order
Hinged	[kN]	[kN]	[kNm]	[kNm]	[m]	[m]
Analytical	-38,848	-39,035	3,460	4,611	0.0469	0.0573
Scia Engineer	-38,810	-38,997	2,626	4,614	0.0409	0.0606
Scia Engineer Imperf. drawn	-38,868	-39,023	3,534	4,821	0.0476	0.0605
Clamped						
Analytical	-39,598	-39,912	2,637	3,206	0.0367	0.0408
Scia Engineer	-39,394	-39,831	1,952	3,157	0.0325	0.0418
Scia Engineer Imperf. drawn	-39,537	-39,884	2,331	2,958	0.0380	0.0431
Flexible						
Analytical	-36,876	-39,021	9,320	11,708	0.3258	0.3611
Scia Engineer	-36,852	-39,351	8,478	11,690	0.3196	0.3764
Scia Engineer Imperf. drawn	-36,925	-39,348	9,318	12,000	0.3288	0.3801

Drawing the imperfection manually will lead to slightly higher bending moments in nonlinear (2nd order) analysis, but its influence on the linear (1st order) bending moments, the goal of the investigation, demonstrates the large share of the initial imperfection on the magnification factor between linear and geometrically imperfect nonlinear analysis.

13.7 Loading according to ultimate limit state – city bridge Nijmegen

All considered load cases in chapter 13 are generalised loads, somehow based on the loads of the city bridge Nijmegen, to investigate the different load cases. When considering the bending moment magnification more specific for the city bridge, the ultimate limit state loads should be considered. Furthermore, the support stiffnesses should be more realistic, thus internal forces and deformations should resemble the results of the structural analysis of the entire approach bridge model.

13.7.1 Load

The loads in ultimate limit state (including partial safety factors, $\gamma_G = \gamma_Q = 1.35$) are:

- Self-weight $\rightarrow q_{Ed} = 421.9\ kN/m$
- Fill and parapets $\rightarrow q_{Ed}(x) = 16.2 + 2.217 \cdot (x - 0.5l)^2\ kN/m$
- Pavement $\rightarrow q_{Ed} = 338.9\ kN/m$

- Traffic load
  - Uniformly distributed load $(64\ kN/m)$
  - Pedestrian load $(4.40 \cdot 3\ kN/m)$

    $\rightarrow q_{Ed} = 104.2\ kN/m$

- Tandem axle $\rightarrow F_{Ed} = 2 \cdot 810\ kN$

13.7.2 Support stiffness

When considering the results that are computed during design, it can be seen that there are two characteristic boundary conditions for the city bridge design. The translation at the support is relatively large at the supports and much smaller in the intermediate spans. Therefore two combinations are considered:

- Flexible high ULS $C_{high} = 3{,}000\ \mathrm{MNm/rad}$ and $k_{high} = 1{,}000\ \mathrm{MN/m}$
- Flexible low ULS $C_{low} = 200\ \mathrm{MNm/rad}$ and $k_{low} = 50\ \mathrm{MN/m}$

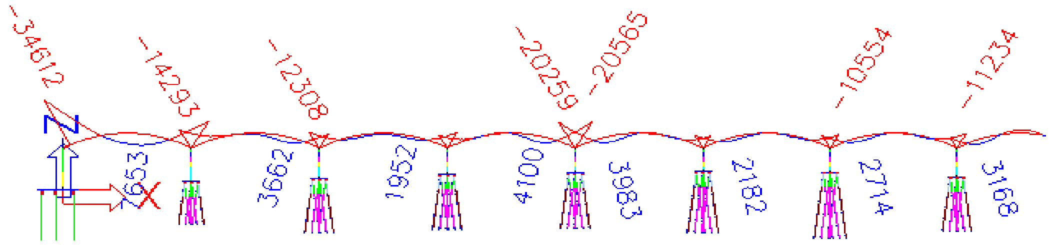

Figure 58: Linear bending moment distribution city bridge

13.7.3 Results

Since deformations determine the second order internal forces, the low and medium stiffnesses as described in paragraph 13.1 are investigated in combination with the city bridge load too. As to be expected, the higher support stiffness leads to much lower second order bending moments.

Table 25: ULS loading city bridge (Bending moments at tandem axle 0.25 L, displacements at mid span)

	Horizontal thrust H		Bending moment M		Displacement w	
	1st order	2nd order	1st order	2nd order	1st order	2nd order
Flexible high ULS	[kN]	[kN]	[kNm]	[kNm]	[m]	[m]
Analytical	-41,493	-42,028	6,049	7,305	0.0868	0.0990
Scia Engineer	-42,227	-42,787	6,459	8,212	0.0622	0.0607
Flexible low ULS						
Analytical	-37,053	-46,121	19,871	24,118	0.8115	1.0275
Scia Engineer	-37,875	-52,393	19,950	32,441	1.0981	1.9119

Table 25 illustrates the geometrically nonlinear theory. When increasing the load from serviceability limit state to ultimate limit state, the internal forces increase and the bending moment magnification factors increase as well. The magnification factors on the bending moments in Table 25 are respectively 1.21 – 1.27 – 1.21 – 1.63. As stated in paragraph 13.6.2, the analytical model is not accurate for large deformations (low stiffnesses), which can easily be seen in the table.

13.7.4 Incremental loading

In the previous analyses, the load is applied in one step. However, all structures will be built incrementally and thus will deform incrementally. This will affect the final deformation in a second order analysis. For the Nijmegen city bridge load, the effect is analysed. The load is divided in four steps: (1) Self-weight, (2) Parapets and backfill, (3) Pavement and barriers and (4) traffic load. The deformed shape due to a load step is used in the geometry for the next step.

The bending moments for each load step are displayed in Figure 59 for high support stiffness. In all bending moment distributions, the geometrically nonlinear behaviour is included.

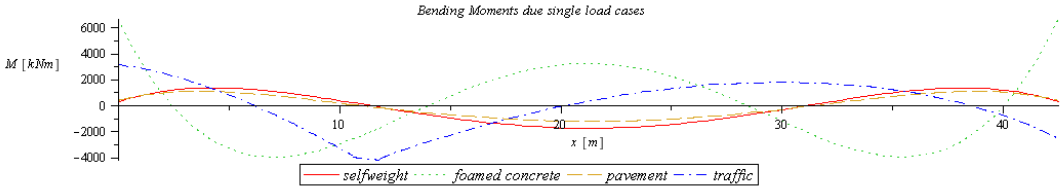

Figure 59: Bending moments - single load cases – high support stiffness

When summing the bending moments after each load step with the bending moments calculated in previous steps, the diagrams in Figure 60 are obtained.

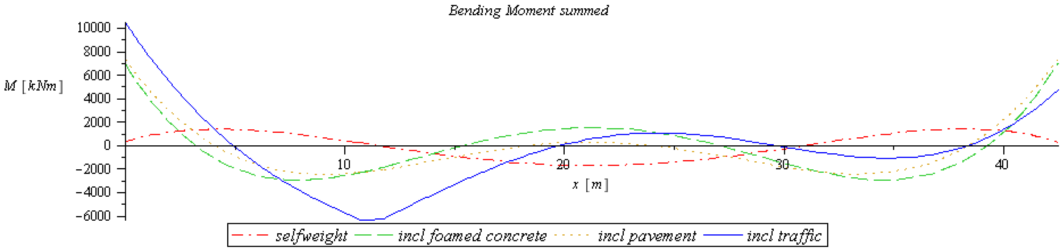

Figure 60: Bending moments – summed with results previous load steps – high support stiffness

Comparing iterative loading and loading in one step

The iterative loading analysis is compared with the previous analysis. In Figure 61- Figure 63 the resulting bending moments are displayed for several support conditions.

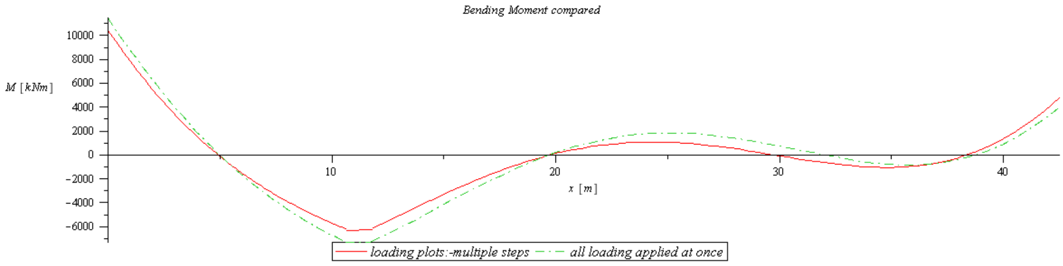

Figure 61: Bending moments - comparing iterative and non-iterative loading - high support stiffness

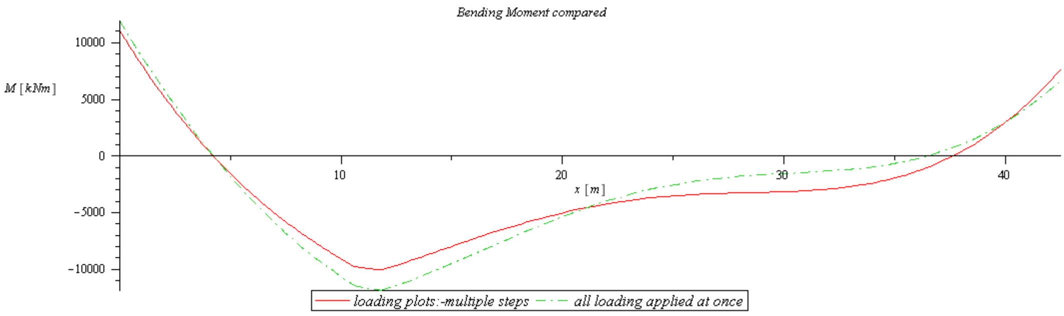

Figure 62: Bending moments - comparing iterative and non-iterative loading - medium support stiffness

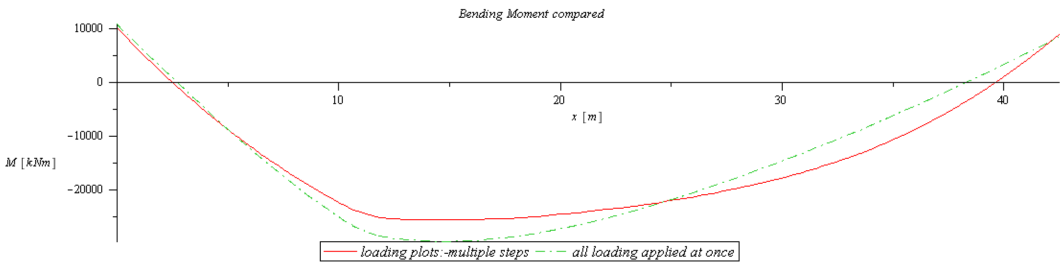

Figure 63: Bending moments - comparing iterative and non-iterative loading - low support stiffness

The results seem to coincide well visually, the iterative loading leads to bending moments that are 3% to 7% smaller compared with the loading in one step. So the more straightforward approach, to apply all load at the same time, leads to slightly higher forces and is therefore a safe assumption.

14. Comparing magnification factors

In structural analysis of columns, geometrically nonlinear behaviour is captured in the bending moment magnification factor. For columns, the magnification factor is linked to the critical load factor, the quotient of the Euler buckling load and the actual normal force. For rigid bars and for a flexible bar with sine shaped imperfection, this factor defines the exact magnification factor. However, for differently shaped imperfections and transverse loads, the formula $n/(n-1)$ is not exact, but the deviations are small. Especially when the critical load factor is low and the buckling mode is affine with the displacement caused by the load.

To determine whether the affine buckling mode might provide a reasonable estimation for the magnifications of bending moments in a single arch, linear stability analyses are carried out in Scia Engineer, providing the buckling modes and the accompanying critical load factors. Theoretical magnification factors are then easily obtained. The models that are analysed, are the same models that are used in the previous investigation (Table 26) and the results of the geometrically nonlinear analyses are displayed in the table as well. The n_1 values coincide with the anti-symmetrical buckling mode, the n_2 values with the symmetrical buckling mode. The influence of a geometrical imperfection on the buckling load is not investigated and therefore not included in the table.

In buckling analysis, a reduced Young's modulus should be applied to account for the nonlinear material behaviour. In arches, the deformation and the normal forces increase simultaneously. Therefore, the tangent stiffness of the stress-strain relation should be used [Cem73-3]. For good coherence between the nonlinear analysis and the buckling analysis, it is assumed that the tangent stiffness for buckling has the same value as the fictitious Young's modulus, $E_f = 12{,}718\ \mathrm{N/mm^2}$.

Table 26: Bending moment magnification factors via buckling analysis

	Stability analysis		Stability analysis		Geometrically nonlinear	
Uniform Load	n_1	$n_1/(n_1-1)$	n_2	$n_2/(n_2-1)$	**Analytical**	**Scia**
Hinged	*1.60*	2.67	*3.61*	1.38	1.34	1.39
Clamped	*3.36*	1.42	*5.47*	1.22	1.21	1.23
Flexible low	*2.01*	1.99	*4.10*	1.32	1.40	1.71
Flexible high	*2.77*	1.56	*4.67*	1.27	1.23	1.25
Non-uniform load	n_1	$n_1/(n_1-1)$	n_2	$n_2/(n_2-1)$	**Analytical**	**Scia**
Hinged	*2.00*	2.00	*4.53*	1.28	1.29	1.34
Clamped	*4.40*	1.29	*7.17*	1.16	1.19	1.22
Flexible low	*2.52*	1.66	*5.19*	1.24	1.28	1.43
Flexible high	*3.55*	1.39	*6.01*	1.20	1.07	1.05
Half span load	n_1	$n_1/(n_1-1)$	n_2	$n_2/(n_2-1)$	**Analytical**	**Scia**
Hinged	*3.19*	1.46	*7.22*	1.28	1.37	1.54
Clamped	*6.72*	1.17	*10.9*	1.16	1.15	1.19
Flexible low	*4.01*	1.33	*8.21*	1.24	1.26	1.39
Flexible high	*5.53*	1.39	*9.34*	1.20	1.19	1.24

	Stability analysis		Stability analysis		Geometrically nonlinear	
Point loads	n_1	$n_1/(n_1-1)$	n_2	$n_2/(n_2-1)$	**Analytical**	**Scia**
Hinged	*50.16*	1.02	*114*	1.01	1.01	1.02
Clamped	*108.2*	1.01	*180*	1.01	1.01	1.01
Flexible low	*63.16*	1.02	*130*	1.01	1.01	1.02
Flexible high	*87.92*	1.01	*151*	1.01	1.01	1.01
Support settlements	n_1	$n_1/(n_1-1)$	n_2	$n_2/(n_2-1)$	**Analytical**	**Scia**
Clamped	*3.36*	1.42	*5.47*	1.22	1.17	1.23
Flexible low	*2.01*	1.99	*4.10*	1.32	1.15	1.46
Flexible high	*2.77*	1.56	*4.67*	1.27	0.79	0.77
Height	n_1	$n_1/(n_1-1)$	n_2	$n_2/(n_2-1)$	**Analytical**	**Scia**
h=350	*1.29*	4.45	*2.14*	1.88	1.10	1.38
h=450	*2.42*	1.70	*4.22*	1.31	1.03	1.08
h=600	*4.95*	1.25	*9.33*	1.12	1.06	1.06
h=750	*8.91*	1.13	*17.7*	1.06	1.06	1.07
Loads	n_1	$n_1/(n_1-1)$	n_2	$n_2/(n_2-1)$	**Analytical**	**Scia**
0.5 q	*6.28*	1.19	*11.2*	1.10	1.06	1.04
1.0 q	*3.14*	1.47	*5.62*	1.22	1.13	1.10
1.5 q	*2.09*	1.92	*3.75*	1.36	1.22	1.19
2.0 q	*1.57*	2.75	*2.81*	1.55	1.33	1.30
2.5 q	*1.26*	4.85	*2.25*	1.80	1.48	1.50
3.0 q	*1.05*	21	*1.87*	2.15	1.67	-
4.0 q	*0.79*	-	*1.41*	3.44	2.24	-
5.0 q	*0.63*	-	*1.12*	9.33	3.21	-
7.5 q	*0.42*	-	*0.75*	-	11.54	-

The table illustrates the principle relation between the affine buckling mode and the bending moment magnification. The symmetrical buckling mode, which coincides best with the deformations due to the uniform load, appears to be a better representation for the bending moment magnification, when compared with the lowest (anti-symmetrical) buckling mode. Additionally, for the half span load, the anti-symmetrical buckling mode is the better approximation, supporting the hypothesis of using the affine buckling mode. For arches there is no general analytical relation derived, which could link the buckling load to the bending moment magnification and for a statistical proof, the number of computations is too small. Especially since the buckling load is sensitive for variations in rise and span (chapter 15), which are not varied in the comparison with the geometrically nonlinear analysis in Table 26.

Furthermore, the linear and the second order bending moment distributions have different shapes. Thus the bending moment magnification factor is not constant along the arch. The displayed results are given in the regions of maximum bending moments (at mid span or at a quarter of the span), which are the most important locations to determine the magnification. Nevertheless, comparing these values with the buckling load analyses via $n/(n-1)$, might lead to some differences, since only one value at one location along the arch is compared. To determine the order of magnitude of the factor in a quick check, the affine buckling mode provides a reasonable approximation for the bending moment magnification of the perfect structure. It does not cover the extra loading due to imperfections. For a more detailed result, the geometrically nonlinear analysis is required.

15. Different arch geometries

The investigation of the geometrically nonlinear behaviour so far is based on the Nijmegen city bridge geometry. This part will provide insight in the bending moments and their magnification in nonlinear analysis for arches with different geometries. In the model, a strip of unit width ($1\ m$) is used. The different geometries will focus on the spans and rise-to-span ratios. The cross-sectional height will be adapted according to the span. For the spans values between $10\ \mathrm{m}$ and $100\ \mathrm{m}$ are investigated, the rise to span ratio varies from $f/l = 0.1$ to 0.5. Values higher than 0.5 represent circle segments larger than $180°$, which are not likely to be applied for structural purposes. The chosen combinations are displayed in Table 27.

Table 27: Overview of investigated geometries

Span $[\mathbf{m}]$	$\boldsymbol{h}\,[\mathbf{mm}]$	$\boldsymbol{f/l = 0.1}$ $\boldsymbol{f}\,[\mathbf{m}]$	$\boldsymbol{f/l = 0.2}$ $\boldsymbol{f}\,[\mathbf{m}]$	$\boldsymbol{f/l = 0.3}$ $\boldsymbol{f}\,[\mathbf{m}]$	$\boldsymbol{f/l = 0.4}$ $\boldsymbol{f}\,[\mathbf{m}]$	$\boldsymbol{f/l = 0.5}$ $\boldsymbol{f}\,[\mathbf{m}]$
10	300	1	2	3	4	5
25	400	2.5	5	7.5	10	12.5
50	500	5	10	15	20	25
75	750	7.5	15	22.5	30	37.5
100	1,000	10	20	30	40	50

Since stiffness is a governing parameter, the geometries are combined with two support conditions (clamped and flexible supports) and two Young's moduli (E_f and $2 \cdot E_f$). For the flexible supports, stiffnesses $C = 20 \cdot L\ \mathrm{kNm/rad}$ and $k = 10 \cdot L\ \mathrm{kN/m}$ are used, so that support stiffness is higher for larger spans. The fictitious Young's moduli are $E_f = 12{,}718\ \mathrm{N/mm^2}$ and $2E_f \approx 25{,}000\ \mathrm{N/mm^2}$ (see paragraph 18.2.1). Five spans, five span to rise ratios, two supports and two Young's moduli lead to 100 combinations ($5 \cdot 5 \cdot 2 \cdot 2$).

To limit the amount of data, only a single load case will be reviewed. Since the loading will depend on the backfill volume and this volume is depending on the span and rise, it has been chosen to neglect the nonlinear loading pattern and to use a uniform distributed load. An intermediate value is chosen, based on the ultimate limit state city bridge load, which varies between $890\ \mathrm{kN/m}$ and $1{,}882\ \mathrm{kN/m}$. For the intermediate value of the load $q = 1{,}285\ \mathrm{kN/m}$ is chosen. It is based on the vertical support reaction of the nonlinear load in single arch analysis ($R = 27{,}314\ \mathrm{kN}$) divided by the half span length ($0.5 \cdot 42.5\ \mathrm{m}$). For the unit width strip, this leads to $q = 1{,}285/25 = 51.4\ \mathrm{kN/m}$.

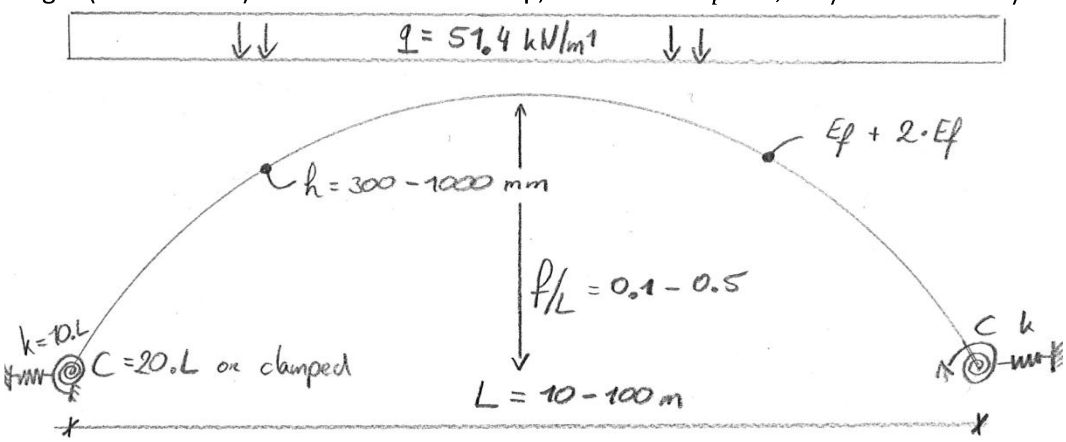

Figure 64: Overview model

15.1 Analysis results

A brief overview of the obtained results is provided in Table 28 to Table 31.

15.1.1 Clamped arch

Young's modulus E_f

Table 28: Bending moments [kNm] for clamped arches with Young's modulus Ef

Span	f	Support			Midspan		
$[\mathrm{m}]$	$[\mathrm{m}]$	Linear	Nonlinear	Factor	Linear	Nonlinear	Factor
10	1	-27.39	-28.00	1.02	19.02	18.24	0.96
	2	13.70	13.45	0.98	13.68	12.93	0.95
	3	45.96	46.09	1.00	23.02	22.17	0.96
	4	85.58	86.22	1.01	39.03	38.49	0.99
	5	133.72	134.94	1.01	60.98	60.85	1.00
25	2.5	-26.24	-18.02	0.69*	45.46	49.99	1.10
	5	127.96	134.54	1.05	64.54	68.96	1.07
	7.5	312.09	324.58	1.04	132.84	142.14	1.07
	10	553.44	577.14	1.04	236.44	254.93	1.08
	12.5	851.35	894.87	1.05	375.24	410.26	1.09
50	5	46.69	183.29	3.93	105.49	210.40	1.99
	10	553.05	689.34	1.25	237.58	353.25	1.49
	15	1269.67	1524.11	1.20	521.10	740.91	1.42
	20	2228.62	2721.07	1.22	938.98	1372.25	1.46
	25	3417.52	4373.02	1.28	1495.76	2363.27	1.58
75	7.5	105.28	413.86	3.93	237.31	474.73	2.00
	15	1245.16	1552.52	1.25	534.42	796.04	1.49
	22.5	2858.09	3430.84	1.20	1172.23	1668.19	1.42
	30	5016.09	6124.10	1.22	2112.40	3088.72	1.46
	37.5	7691.21	9841.07	1.28	3365.14	5318.65	1.58
100	10	187.31	736.66	3.93	421.85	844.78	2.00
	20	2214.10	2760.94	1.25	950.00	1415.90	1.49
	30	5081.90	6100.29	1.20	2083.82	2966.40	1.42
	40	8918.57	10888.37	1.22	3755.20	5491.79	1.46
	50	13674.45	17496.47	1.28	5982.25	9456.24	1.58

* for the $25\ \mathrm{m}$ span and $2.5\ \mathrm{m}$ rise, the small negative bending moment decreases by a large factor. However, the absolute value of the reduction is only $6\ \mathrm{kNm}$. In Figure 70 it is explained that at some point along the arch, the bending moments can reduce in geometrically nonlinear analysis when compared with linear analysis, due to the imaginary second order load. For the other Young's modulus and support conditions, reductions of the support bending moment for the arch $L = 25\ \mathrm{m}, f = 2.5\ \mathrm{m}$ were found in analysis too.

Young's modulus $2 \cdot E_f$

Table 29:Bending moments [kNm] for clamped arches with Young's modulus 2*Ef

Span $[\mathrm{m}]$	f $[\mathrm{m}]$	Support Linear	Nonlinear	Factor	Midspan Linear	Nonlinear	Factor
10	1	-27.39	-28.18	1.03	19.02	18.07	0.95
	2	13.70	13.34	0.97	13.68	12.86	0.94
	3	45.96	45.93	1.00	23.01	22.05	0.96
	4	85.58	85.94	1.00	39.03	38.27	0.98
	5	133.72	134.44	1.01	60.98	60.45	0.99
25	2.5	-26.24	-22.73	0.87	45.46	47.04	1.03
	5	127.96	130.93	1.02	64.54	66.17	1.03
	7.5	312.09	318.17	1.02	132.84	136.90	1.03
	10	553.44	565.15	1.02	236.44	244.99	1.04
	12.5	851.35	872.77	1.03	375.23	391.72	1.04
50	5	46.69	96.62	2.07	105.49	138.61	1.31
	10	553.05	611.10	1.10	237.58	284.35	1.20
	15	1269.67	1380.49	1.09	521.10	612.68	1.18
	20	2228.63	2440.00	1.09	938.98	1116.04	1.19
	25	3417.52	3812.03	1.12	1495.76	1831.48	1.22
75	7.5	105.28	218.79	2.08	237.13	313.13	1.32
	15	1245.16	1376.46	1.11	534.42	640.95	1.20
	22.5	2858.09	3107.66	1.09	1172.23	1379.59	1.18
	30	5016.09	5491.60	1.09	2112.40	2512.09	1.19
	37.5	7691.21	8578.66	1.12	3365.13	4121.80	1.22
100	10	187.31	389.82	2.08	421.85	557.47	1.32
	20	2214.10	2447.92	1.11	950.00	1140.16	1.20
	30	5081.91	5525.72	1.09	2083.82	2453.28	1.18
	40	8918.58	9763.87	1.09	3755.20	4466.57	1.19
	50	13674.45	15252.02	1.12	5982.25	7328.28	1.23

15.1.2 Flexible arch

Young's modulus E_f

Table 30: Bending moments [kNm] for flexible supported arches with Young's modulus Ef

Span $[\mathrm{m}]$	f $[\mathrm{m}]$	Support Linear	Nonlinear	Factor	Midspan Linear	Nonlinear	Factor
10	1	-154.64	-157.67	1.02	90.12	91.74	1.02
	2	-33.85	-34.10	1.01	39.61	39.20	0.99
	3	20.39	20.57	1.01	35.93	35.21	0.98
	4	66.37	67.04	1.01	47.51	47.05	0.99
	5	115.89	117.15	1.01	67.86	67.82	1.00
25	2.5	-112.93	-99.56	0.88	90.99	102.07	1.12
	5	99.23	107.04	1.08	77.87	83.19	1.07
	7.5	288.35	301.50	1.05	141.54	151.50	1.07
	10	526.23	550.63	1.05	245.01	264.34	1.08
	12.5	818.88	863.36	1.05	384.89	421.11	1.09
50	5	-1.8	165.81	-	129.95	260.67	2.01
	10	526.86	668.39	1.27	247.24	368.26	1.49
	15	1234.86	1494.09	1.21	531.40	757.53	1.43
	20	2180.66	2680.22	1.23	952.42	1395.50	1.47
	25	3356.47	4323.43	1.29	1512.82	2396.65	1.58
75	7.5	30.94	383.45	-	274.41	555.65	2.02
	15	1178.57	1496.83	1.27	555.85	832.06	1.50
	22.5	2750.26	3336.64	1.21	1202.17	1718.28	1.43
	30	4859.97	5990.28	1.23	2155.02	3163.75	1.47
	37.5	7489.28	9676.13	1.29	3420.86	5428.84	1.59
100	10	84.84	688.31	-	472.18	963.38	2.04
	20	2075.19	2641.90	1.27	991.33	1488.82	1.50
	30	4836.07	5883.99	1.22	2150.32	3079.56	1.43
	40	8555.60	10575.82	1.24	3853.30	5665.97	1.47
	50	13201.83	17108.65	1.30	6112.09	9714.36	1.59

Young's modulus $2 \cdot E_f$

Table 31: Bending moments [kNm] for flexible supported arches with Young's modulus $2 \cdot E_f$

Span $[\mathrm{m}]$	f $[\mathrm{m}]$	Support Linear	Nonlinear	Factor	Midspan Linear	Nonlinear	Factor
10	1	-202.11	-204.97	1.01	124.42	125.29	1.01
	2	-62.76	-63.26	1.01	58.10	57.63	0.99
	3	2.36	2.32	0.98	46.12	45.29	0.98
	4	51.79	52.13	1.01	54.42	53.75	0.99
	5	101.73	102.44	1.01	73.55	73.12	0.99
25	2.5	-182.88	-176.81	0.97	130.20	138.05	1.06
	5	74.65	78.62	1.05	89.83	92.30	1.03
	7.5	267.59	274.22	1.02	149.35	154.02	1.03
	10	502.07	514.34	1.02	252.71	262.04	1.04
	12.5	789.67	811.88	1.03	393.61	411.20	1.04
50	5	-45.59	23.65	-	152.70	200.50	1.31
	10	502.94	564.91	1.12	256.20	306.87	1.20
	15	1202.82	1317.16	1.10	540.94	637.26	1.18
	20	2136.19	2352.75	1.10	964.91	1149.10	1.19
	25	3299.53	3702.26	1.12	1528.74	1875.43	1.23
75	7.5	-34.54	103.75	-	308.57	408.44	1.32
	15	1119.24	1257.90	1.12	575.26	692.31	1.20
	22.5	2653.22	2912.17	1.10	1229.23	1451.62	1.18
	30	4718.04	5209.10	1.10	2193.81	2616.99	1.19
	37.5	7304.07	8217.16	1.13	3471.99	4265.18	1.23
100	10	-3.15	225.27	-	517.93	689.63	1.33
	20	1954.47	2200.44	1.13	1027.80	1240.53	1.21
	30	4619.64	5082.65	1.10	2209.05	2613.12	1.18
	40	8231.90	9110.85	1.11	3940.88	4707.15	1.19
	50	12775.43	14409.79	1.13	6229.26	7661.05	1.23

15.2 Conclusion different geometries

The results of the analyses in the tables of chapter 15.1 are displayed in graphs. The bending moment magnification factors at mid span and at the support are displayed as a function of the rise to span factor.

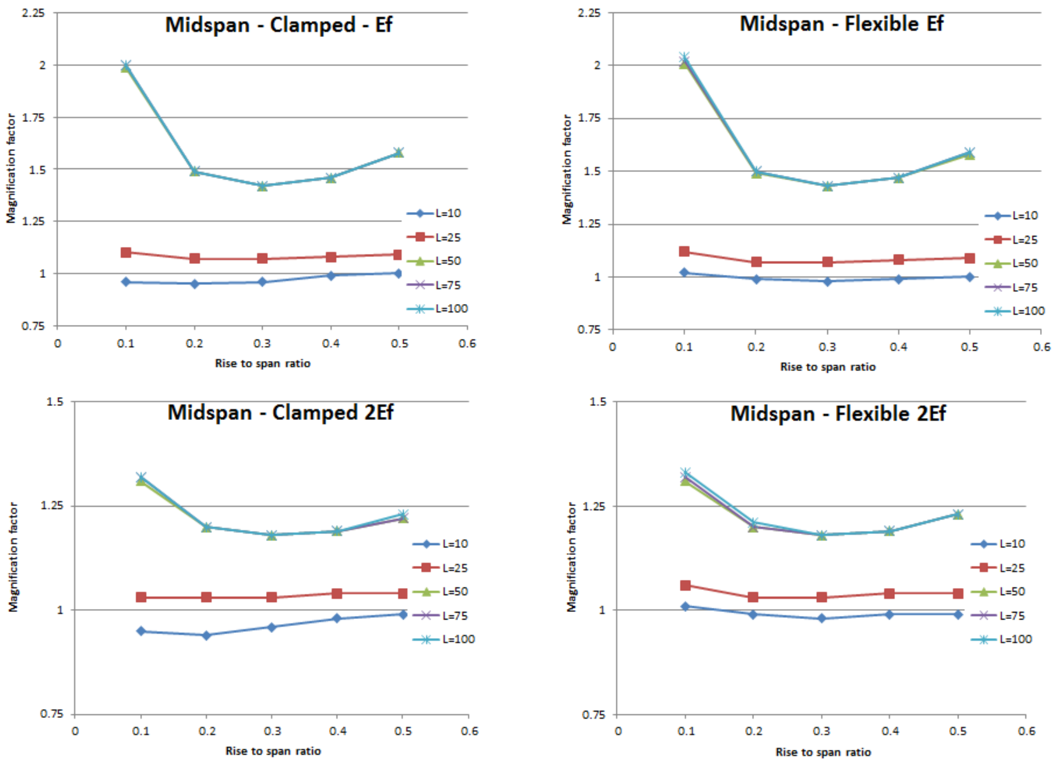

Figure 65: Bending moment magnification at mid span

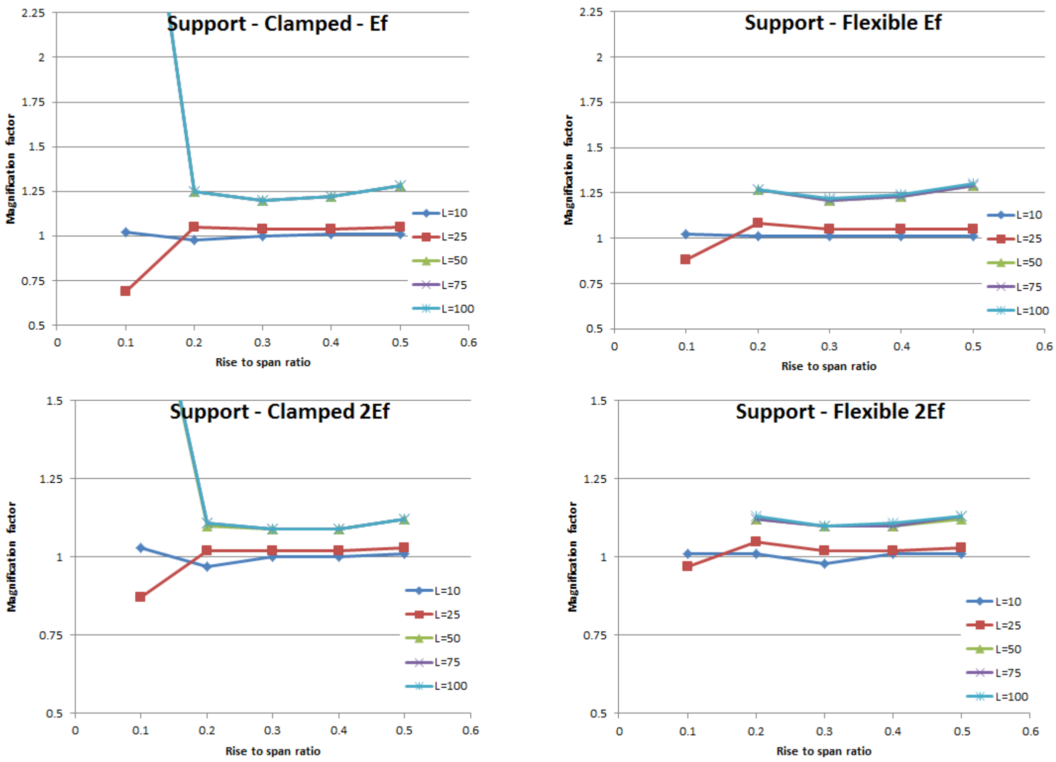

Figure 66: Bending moment magnification at support

Both the bending moments at support and at mid span increase for higher rise to span ratios. Simultaneously, the bending moment magnification reduces due to the lower normal forces that occur when the arch's rise is high, only for the highest investigated rise to span ratio ($f/L = 0.5$), deformations are larger and magnification factors increase a little.

For the spans $L = 50$, $L = 75$ and $L = 100$ m equal magnification factors are found. For these spans, the cross-sectional height increases proportional to the span ($h = 0.01L$). For the spans $L = 10$ and $L = 25$ m this relation was not used, since bending stiffness was assumed to relate cubically to the cross-sectional height ($I = bh^3/12$) and thus higher cross-sectional heights were chosen. The much lower magnification factor for the spans $L = 10$ and $L = 25$ m might be caused by the relatively high cross-sectional height, compared with the other three investigated spans.

Span [m]	**h [mm]**
10	300
25	400
50	500
75	750
100	1,000

The rise to span ratio $f/L = 0.1$ leads to unrealistically high magnification factors, due to the low first order bending moments. For the rise to span ratio's $f/L = 0.3$ and 0.4 the lowest magnification factors are found.

16. Conclusions single arch analysis

16.1 Bending moment magnification

The second order bending moment distribution in arched structures is a complex phenomenon, dictated by loads, geometry and stiffnesses, which determine together the mathematical second order load ($H \cdot w''$). Since the deformed arch has C^2 continuity (C^2: first and second derivative are continuous), the second order load is at least C^0 continuous (C^0: only function itself is continuous) and the second order bending moment is C^2 continuous again. Since the mathematical second order load $H \cdot w''$ has a different distribution compared with the loads q and F, which are applied in the linear analysis step, the bending moment distributions have different shapes. This is illustrated in Figure 68, in which the non-uniform load and a tandem axle are applied to a single arch with flexible supports. Since the first order and second order bending moments have different shapes, the bending moment magnification varies along the arch span (Figure 69).

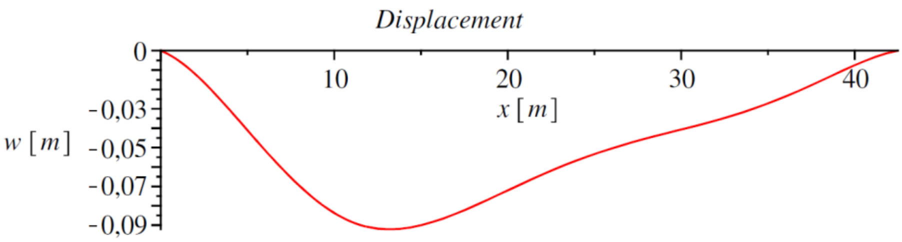

Figure 67: First order deformation

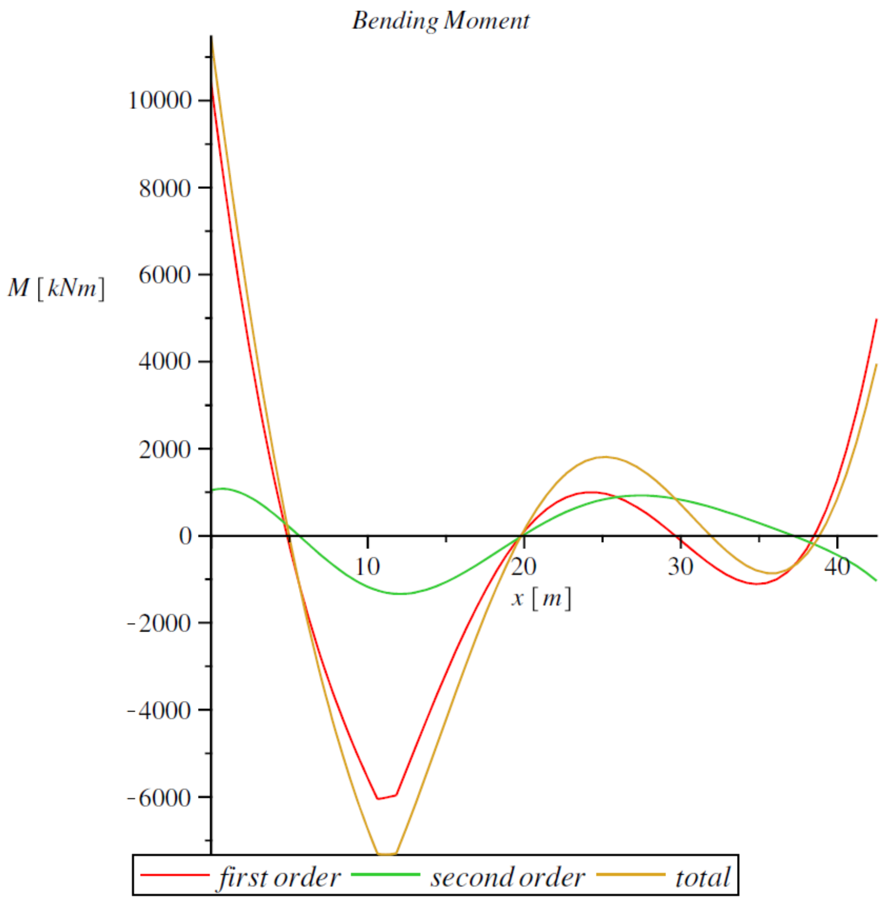

Figure 68: Bending moment distribution, first order, second order and total

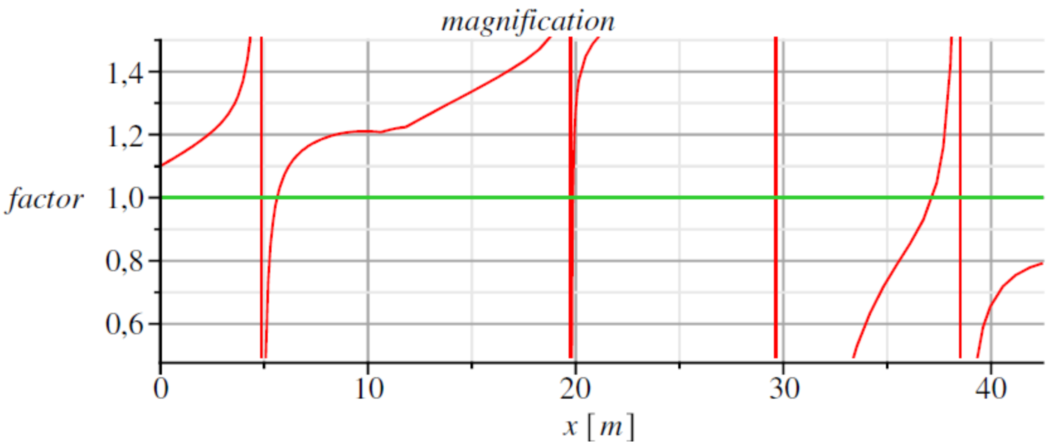

Figure 69: Bending moment magnification

The internal forces and deformations that are computed in the analysis of arched structures are influenced by many parameters, in which the stiffnesses are the most important. A uniform formula or rule of thumb cannot be given. The affine buckling appears to be a good approximation when designing for the maximum bending moments. However, to understand the principle of geometrically nonlinear behaviour in arches, a different way of thinking is required. Instead of linking geometrical nonlinearity to buckling, as is good practice in column design, the geometrically nonlinear behaviour of arches could better be envisioned in terms of the second order loading, $H \cdot w''$. This second derivative of deformations might be a vague concept, but it can be imagined via the analogy with the moment area method (Mohr's theorems). This moment area method uses the Euler-Bernoulli bending theory to compute rotations and deflections ($w'' = \kappa = -M/EI$) by loading the structure with the reduced bending moment area. In second order analysis of arched structures, this reduced bending moment area can be used too. When multiplied by the horizontal thrust, the imaginary second order load is obtained (axial deformation are neglected) and second order bending moments can be computed. In Figure 70, the concept of the reduced bending moment area is presented for a flexible supported arch with uniformly distributed load.

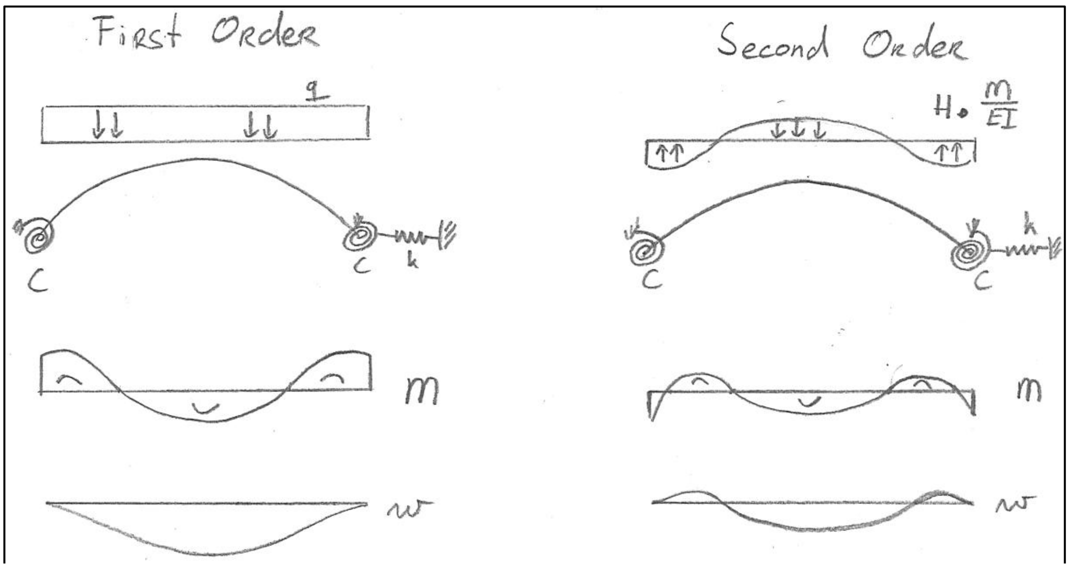

Figure 70: Visualization second order loading for engineering judgement (not to scale)

Although several combinations of load cases and stiffnesses are investigated and results of analytical and finite element analysis coincide well, the internal forces depend on stiffnesses. When assuming a stiffness parameter (Young's modulus, cross-sectional dimensions, support stiffness) it should be kept in mind that the chosen value has a major influence on the obtained results. And especially for the low stiffnesses, irrespectively of which stiffness is low, the results of the models differ.

16.2 SLS and ULS loading

In terms of loading, the difference between serviceability and ultimate limit state are the partial safety factors. In linear analysis, the internal forces can be multiplied by this factor to obtain the internal forces in ultimate limit state. In geometrically nonlinear analysis, this superposition principle (linearly summing of results) is not valid. Increasing the load will lead to deformations that are larger than proportionally can be expected, based on the load increase. This nonlinear behaviour is illustrated in Figure 71. In this figure, the different approaches to the geometrically nonlinear behaviour are compared. The figure illustrates the non-proportional increase of bending moments when loading is increased from SLS to ULS.

Conform Eurocode, only in ultimate limit state a nonlinear analysis is required to meet safety standards, since the nonlinear effect is larger for higher loads. However, in serviceability limit state, deformations will be larger than computed with linear theory too. For accurate results, a nonlinear analysis could be useful for SLS loading. It should be kept in mind that superposition is not valid and for each load combination, iteratively a solution has to be found. Restricting the number of load combinations in nonlinear analysis is thus essential.

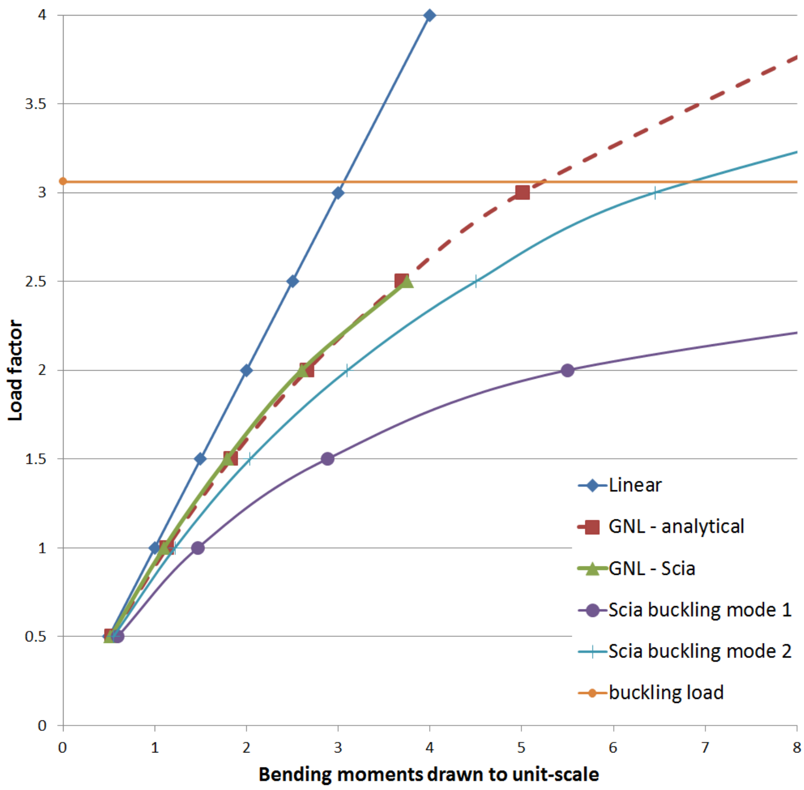

Figure 71: Comparing geometrically nonlinear and stability analyses

Part 3: Multiple arch models (2D)

Contents – Part 3: Multiple arch models

17. Introduction to Part 3

The approach bridge structure consists of several arches, each arch mutually confining the adjacent spans in horizontal direction. Structural systems containing multiple arches benefit this mutual confinement, when compared to single arches. Since the horizontal thrust is excited mainly at the end spans, the deformations that emerge in the intermediate spans to acquire the horizontal thrust are smaller.

In this part, models with multiple arches will be considered to investigate the mutual confinement. The main pier, the intermediate piers and the abutment provide stiffness to the multiple arch system. The horizontal stiffness of the substructure elements is investigated first. In a multiple arch system with flexible supports, the end spans suffer the lower degree of confinement. This edge disturbance results in higher deformations and higher bending moments. Next the number of spans is investigated for the edge disturbance to fade out.

The geometrically nonlinear analysis is carried out for several multiple span models. First the arches are modelled with rotational and translational flexible supports (linear behaviour) at the heel of the arches. After this analysis, the substructure is added for a better representation of the structural system, as the actual response of the substructure in second order analysis is nonlinear. The last analysis in this part deals with the entire approach bridge model, made by BAM Infraconsult and modified for the nonlinear analysis.

18. Modelling

18.1 Load

The distributed load on the arches in ultimate limit state, thus including the partial safety factors ($\gamma_{G,Q} = 1.35$), can be approximated by $q_{Ed} = 890 + 2.216(x - 0.5l)^2$. This load is visualised in Figure 72. As stated in part 1, this load includes permanent loads and distributed traffic load. This load is applied in all models.

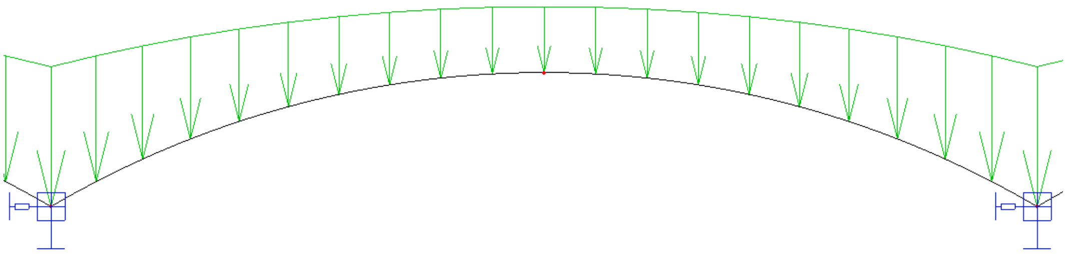

Figure 72: Non-uniform distributed load q_{Ed}

Additionally, tandem axle load, shrinkage and temperature load are modelled in the approach bridge model. For the temperature load, only the shortening due to cooling is analysed, since cooling lead to downward deformations and thus contributing to the second order behaviour. Heating will reduce the deformation due to permanent and traffic load and it is therefore not incorporated in analysis. All loads are summed into fifteen combinations, in which only the location of the tandem axle system differs.

18.2 Arches

In this part, the effect of multiple arches next to each other is investigated. Different geometries are not considered in this analysis. Only the city bridge arch design (span $42.5\ \mathrm{m}$, rise $5.75\ \mathrm{m}$, cross-section $0.5 \cdot 25\ \mathrm{m}^2$) is used.

18.2.1 <u>Young's modulus</u>

The Young's modulus is one of the stiffness parameters, determining the structural behaviour. As stated in part 2, a fictitious Young's modulus can be estimated according to the Dutch national annex to Eurocode 2 (EN1992-1-1).

$$E_f = [2.20 + 440\rho + (24.0 - 220\rho)\alpha_n] \cdot 10^3 \geq 5000$$

In part 2 (paragraph 13.1.2), the formula is evaluated, leading to $E_f = 12{,}718\ \mathrm{N/mm^2}$. A higher Young's modulus will cause higher first order bending moments, but the smaller deformations result in smaller second order bending moments. Therefore, a higher Young's modulus is investigated too in the multiple arch models. For this higher stiffness the value $2 \cdot E_f \approx 25{,}000\ \mathrm{N/mm^2}$ is used. It is higher than the maximum value that can be computed with the estimation formula, but lower than the initial concrete stiffness $E_{cm} = 34.000\ \mathrm{N/mm^2}$. Analysis of the M-N-κ relations in part 4 displayed higher stiffnesses up to $E_f = 42{,}000\ \mathrm{N/mm^2}$, since reinforcement contributes too. This fictitious stiffness of the uncracked cross-section leads to high bending moments and cracking. Due to cracking the stiffness will decrease and bending moments reduce. The fictitious stiffness of the cracked cross-section appears to be approximately $E_f = 10.000 - 15.000\ \mathrm{N/mm^2}$, depending on the height of the cross-section and whether creep is or is not taken into account.

18.2.2 Finite element model

The finite element analyses are based on two-dimensional models, in which (one-dimensional) beam elements are used. For the analyses Scia Engineer is used. This program discretizes a curve into straight elements. An average mesh size of $0.9\ \mathrm{m}$ is applied, so that at least 50 finite elements along a single arch are used. Shear deformations are taken into account and the direct solver is applied in linear analysis. For nonlinear analysis, the Newton-Raphson solver is used. Critical points will not be reached in the analysis, thus refining the size of the load increments is not required. The Timoshenko solver will neglect the increase in normal forces and should not be used.

18.2.3 Number of arches

Structural arch behaviour relies on confinement of the supports. Large share of the horizontal thrust is excited in the end supports (the main pier and the abutment). The intermediate supports contribute little, since the horizontal thrust of the two adjacent spans equalize in these nodes. Nevertheless, the end spans benefit this stiffening due to adjacent spans only on one side. The end supports provide only horizontal support after deformation. This leads to a kind of "edge disturbance" in which high bending moments occur in the end spans. The effect fades out over several spans. Based on a 30 span model (Figure 73), the influence of the end span disturbance is determined and visualised (Figure 73 and Figure 75). For this 30 span model, the upper and lower Young's modulus and the high and low support stiffness are regarded.

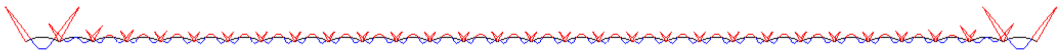

Figure 73: 30 span arch model – bending moment distribution

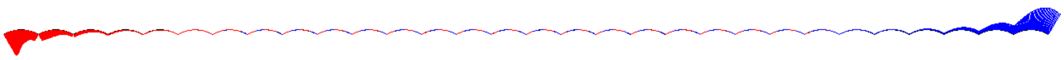

Figure 74: 30 span arch model – displacements u_x along arch

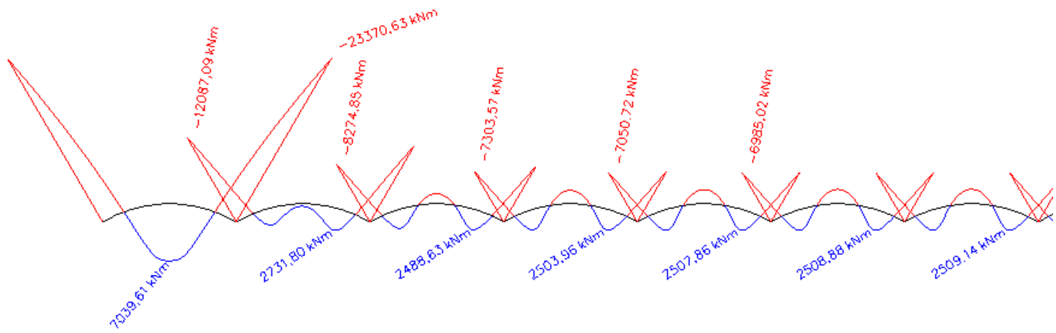

Figure 75: 30 span arch model - bending moment distribution – detail span 1 to 7

All four combinations of support stiffness and Young's moduli lead to similar shapes of the bending moment distribution, although the values of bending moment distributions differ. As can be seen in Figure 75 (bending moments for high support stiffnesses and low Young's modulus), the first span, and the second span to a lesser extent, have different bending moment distributions due to the edge effect. From the fourth span and further away from the edge, the bending moments reach an almost constant distribution for these intermediate spans.

In structural analysis of these multiple arch models, at least three spans are required for the edge effect to fade out. Thus, when modelling two edges, at least seven spans should be modelled to cover both the behaviour at the edges and the behaviour of the spans that are not affected by the edges. This is illustrated by the bending moment distributions for three, five and seven spans (Figure 76).

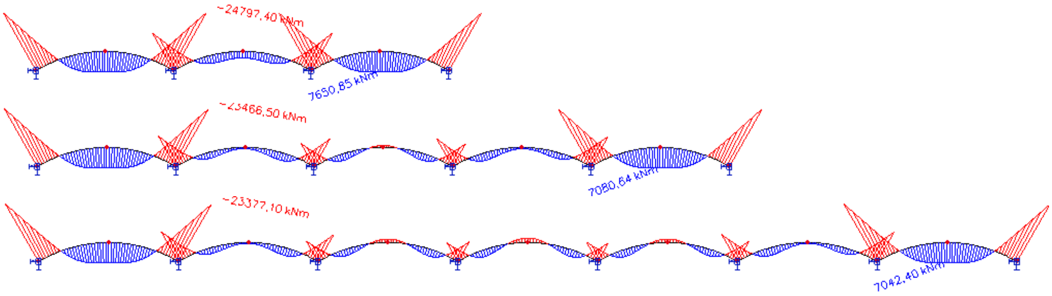

Figure 76: Bending moment distribution for 3, 5 and 7 span arch models

19. Analysis multiple arch models without substructure

Figure 77: 7 span model without substructure

19.1 Support stiffness

19.1.1 Substructure

For the arched structure in the approach bridge, four different cases can be distinguished in the design of the substructure. These four cases are the intermediate piers founded on drilled piles, the intermediate piers founded on vibro piles, the abutment and the main pier at the river bank. These elements all provide horizontal, vertical and rotational stiffness to the arched spans. In this analysis, the vertical stiffness (and support settlements) are not considered. When modelling only a part of the approach bridge, the neglected spans provide horizontal and rotational stiffness to the end spans of the reduced models. The stiffnesses that will be taken into account in analysis, are the horizontal and rotational stiffness. The values are determined by using the two-dimensional model of the approach bridge which is developed by BAM Infraconsult. In these models, the soil stiffness computed in the geotechnical analysis is divided by a factor $\sqrt{2}$ and a fictitious (secant) Young's modulus $E_f = 15{,}849\ \mathrm{N/mm^2}$ is applied. This model is split into the required parts and then loaded by unit forces and unit bending moments ($100{,}000\ \mathrm{kN}\ and\ 100{,}000\ \mathrm{kNm}$ respectively).

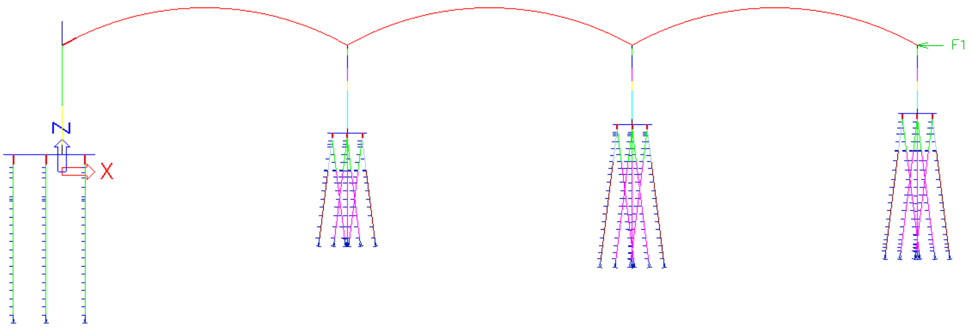

Figure 78: Three spans and river bank pier (left)

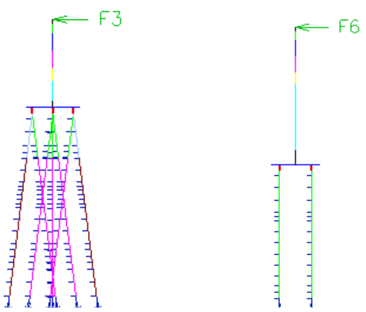

Figure 79: Single piers, founded on vibro piles (left) and drilled piles (right)

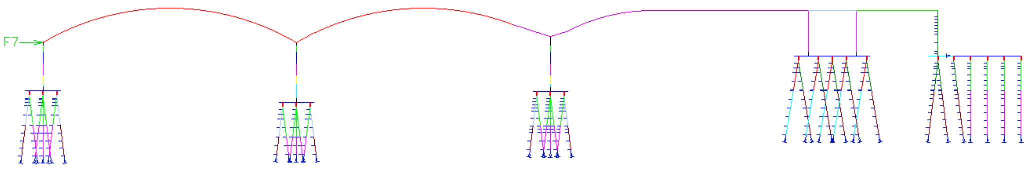

Figure 80: Three spans and abutment (right)

19.1.2 Stiffnesses

Structural linear analysis provides deformations (rotations and translations), via which the stiffnesses are computed easily by $C = M/\varphi$ and $k = F/\,u$. Nevertheless, this is not the exact representation of the model. The formulae are valid for springs. In the structural behaviour there are mutual influences (terms k_{12} and k_{21}), since forces lead to rotations and bending moments to displacements as well. It is visualised in matrix notation:

$$\begin{bmatrix} F \\ M \end{bmatrix} = \begin{bmatrix} k_{11} & k_{12} \\ k_{21} & k_{22} \end{bmatrix} \cdot \begin{bmatrix} u \\ \varphi \end{bmatrix}$$

However, the flexible support conditions in the finite element software can handle only linear translational and linear rotational stiffnesses. Using the C and k values is the most obvious approach. The results of the substructure analysis are displayed in Table 32. The stiffnesses are computed manually and the values are rounded.

Table 32: Substructure analysis results and stiffnesses

	Translation $\boldsymbol{u}$ [mm]	Stiffness $\boldsymbol{k}$ [kN/m]	Rotation $\boldsymbol{\varphi}$ [mrad]	Stiffness $\boldsymbol{C}$ [kNm/rad]
3 span & river pier	905.2	110,000	12.5	8,000,000
3 span & abutment	653.2	153,000	10.9	9,200,000
Piers on vibro piles				
- **Short**	1,375.7		19.7	
- **Medium**	1,955.9		21.4	
- **Long**	1,931.4		20.5	
- ***Average***	*1,754.3*	*57,000*	*20.5*	*4,900,000*
Piers on drilled piles				
- **Short**	4,142.5		28.8	
- **Long**	3,832.2		28.0	
- ***Average***	*3,987.4*	*25,000*	*28.4*	*3,500,000*

To investigate the second order effects, the lower bound value is most probably governing. However, high support stiffness leads to higher normal forces and is therefore included in the investigation.

Table 33: Substructure stiffnesses applied in analyses

Support:	**Intermediate**		**End**	
	$\boldsymbol{C}$ [kNm/rad]	$\boldsymbol{k}$ [kN/m]	$\boldsymbol{C}$ [kNm/rad]	$\boldsymbol{k}$ [kN/m]
Low stiffness	3,000,000	25,000	8,000,000	100,000
High stiffness	5,000,000	60,000	10,000,000	150,000

19.1.3 Soil stiffness

The soil stiffness influences largely the support stiffness for the superstructure. When including the substructure in the structural model, the soil stiffness is a paramount parameter. However, geotechnical analysis is not in the scope of the thesis and similar to the design of structures, conservative values will be used in analysis. In the thesis, the soil stiffnesses are copied unaltered, together with the substructure, out of the existing models made by BAM Infraconsult and are regarded as given parameters.

19.2 Analysis

Based on the linear structural analysis, seven spans are required in the investigation. When considering geometrically nonlinear behaviour, only the first, the second and the middle span will be researched. This limits the amount of data, while still providing information on three characteristic spans of the (symmetrical) multiple arch model.

Four cases are investigated, by combining the low and high support stiffnesses with the lower and upper bound values for the fictitious Young's modulus.

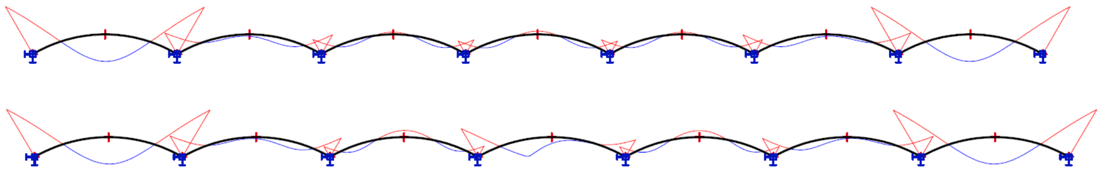

Figure 81: Bending moment distributions without (upper) and with (lower) tandem axle loading at middle span

The bending moment distributions have similar shapes for the different support stiffnesses (denoted by C&k low and high) and the fictitious Young's moduli (E_f and $2 \cdot E_f$). Therefore, for each span the bending moment distributions are graphically displayed only for the C&k low – E_f model. The bending moments that occur in the models with different stiffnesses are displayed numerically in the tables.

19.2.1 End span

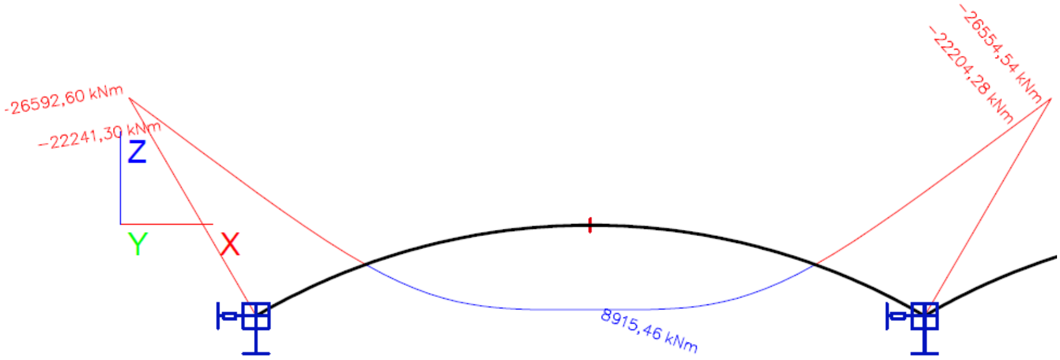

Figure 82: Bending moments endspan - linear

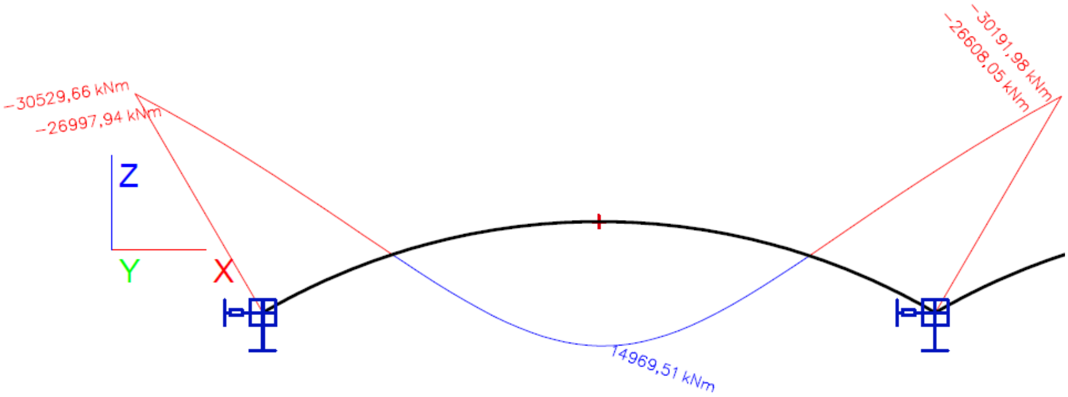

Figure 83: Bending moments endspan - nonlinear

Table 34: End span: characteristic values bending moment distribution

End span Model		$M_{hog-left}$ [kNm]	$M_{sag-mid}$ [kNm]	$M_{hog-right}$ [kNm]
C&k low E_f	Linear	-26,592.6	+8,915.5	-26,554.5
	Non-linear	-30,529.7	+14,969.5	-30,192.0
	Difference	*-3,937.1*	*+6,054.0*	*-3,637.5*
	Factor	*1.15*	*1.68*	*1.14*
C&k low $2 \cdot E_f$	Linear	-35,415.9	+14,594.5	-36,149.2
	Non-linear	-38,709.1	+18,445.9	-38,776.3
	Difference	*-3,293.2*	*-3,851.4*	*-2,627.1*
	Factor	*1.09*	*1.26*	*1.07*
C&k high E_f	Linear	-23,341.1	+7,042.4	-23,377.1
	Non-linear	-24,871.6	+10,634.3	-24,798.6
	Difference	*-1,530.5*	*+3,591.9*	*-1,421.5*
	Factor	*1.07*	*1.51*	*1.06*
C&k high $2 \cdot E_f$	Linear	-31,791.8	+12,207.4	-32,172.9
	Non-linear	-33,934.3	+15,075.2	-33,996.0
	Difference	*-2,142.5*	*+2,867.8*	*-1,823.1*
	Factor	*1.07*	*1.24*	*1.06*

19.2.2 Second span

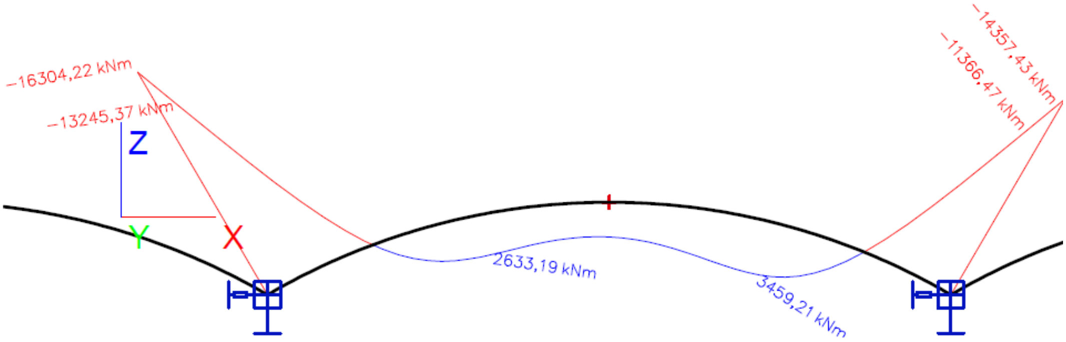

Figure 84: Bending moments second span - linear

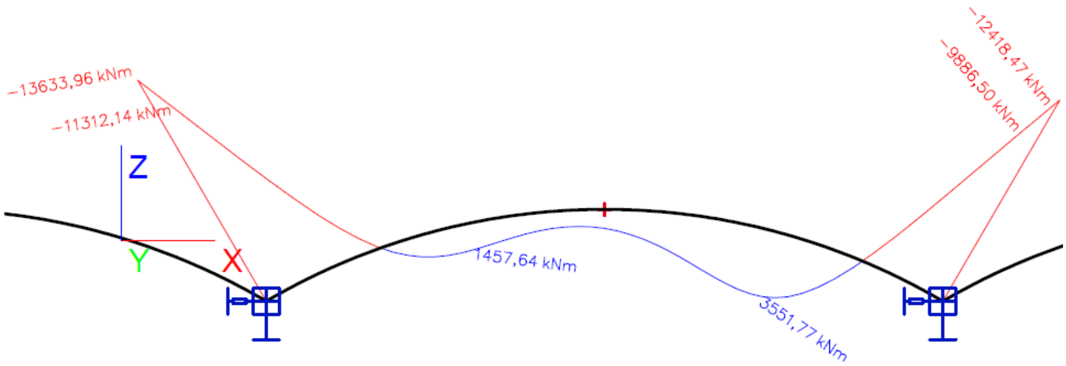

Figure 85: Bending moments second span - nonlinear

Table 35: Second span: characteristic values bending moment distribution

Second span Model		$M_{hog-left}$ [kNm]	$M_{sag-mid}$ [kNm]	$M_{hog-right}$ [kNm]
C&k low E_f	Linear	-16,304.2	+3,459.2	-14,357.1
	Non-linear	-13,634.0	+3,551.8	-12,418.5
	Difference	*+2,670.2*	*+92.6*	*+1,938.6*
	Factor	*0.84*	*1.03*	*0.87*
C&k low $2 \cdot E_f$	Linear	-25,468.9	+6,356.8	-21,370.7
	Non-linear	-24,557.6	+6,731.0	-20,568.8
	Difference	*+911.3*	*+374.2*	*+801.9*
	Factor	*0.96*	*1.06*	*0.96*
C&k high E_f	Linear	-12,105.4	+2,731.2	-10,918.1
	Non-linear	-10,436.0	+3,016.6	-9,845.4
	Difference	*+1,669.4*	*+285.4*	*+1,072.7*
	Factor	*0.86*	*1.10*	*0.90*
C&k high $2 \cdot E_f$	Linear	-18,524.8	+3,958.2	-15,538.4
	Non-linear	-17,486.7	+4,018.7	-14,871.5
	Difference	*+1,038.1*	*+60.5*	*+666.9*
	Factor	*0.94*	*1.02*	*0.96*

19.2.3 Middle span

Since the middle spans have an almost symmetrical bending moment distribution (Figure 86 and Figure 87), only the characteristic values of the left half span are displayed in Table 36 (at the support and the sagging and hogging maxima)

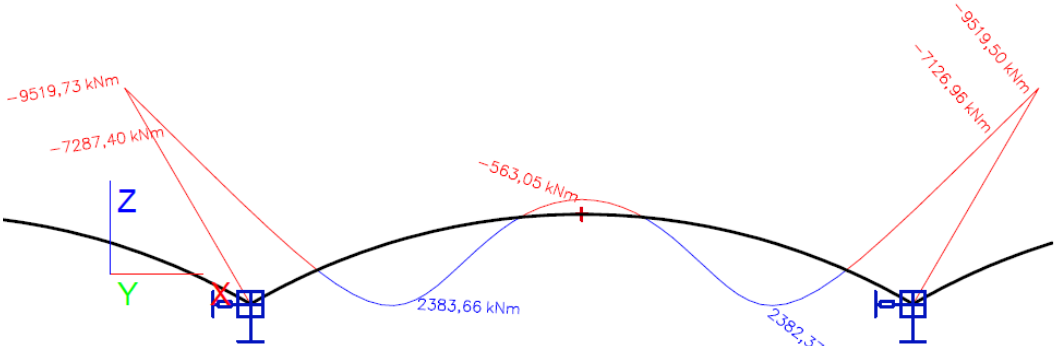

Figure 86: Bending moments middle span - linear

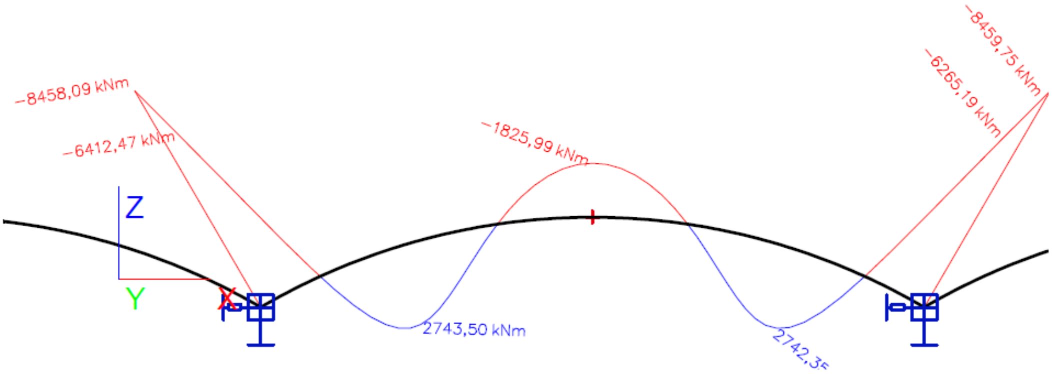

Figure 87: Bending moments middle span - nonlinear

Table 36: Middle span: characteristic values bending moment distribution – left half span

Middle span Model		$M_{hog-supp.left}$ [kNm]	$M_{sag-max}$ [kNm]	$M_{hog-midspan}$ [kNm]
C&k low E_f	Linear	-9,519.7	+2,383.7	-563.1
	Non-linear	-8,458.1	+2,743.5	-1,826.3
	Difference	*+1,061.6*	*+359.8*	*-1,263.2*
	Factor	*0.89*	*1.15*	*3.24*
C&k low $2 \cdot E_f$	Linear	-14,893.9	+2,996.8	+2,059.4
	Non-linear	-13,492.3	+2,709.2	+1,398.7
	Difference	*+1,401.6*	*-287.6*	*-660.7*
	Factor	*0.91*	*0.90*	*0.68*
C&k high E_f	Linear	-7,572.7	+2,450.7	-1,509.2
	Non-linear	-7,753.8	+2,894.9	-2,297.0
	Difference	*-181.1*	*+444.2*	*-787.8*
	Factor	*1.02*	*1.18*	*1.52*
C&k high $2 \cdot E_f$	Linear	-9,616.5	+2,368.2	-538.2
	Non-linear	-9,100.1	+2,456.9	-1,110.2
	Difference	*+516.4*	*+88.7*	*-572.0*
	Factor	*0.95*	*1.04*	*2.06*

19.2.4 Middle span including tandem axle

For bending moment distributions including loading by the tandem axle system, the support bending moments and the sagging bending moment at the tandem axle is provided. In all cases the tandem axle system is positioned at a quarter of the span and 1.2 m towards midspan.

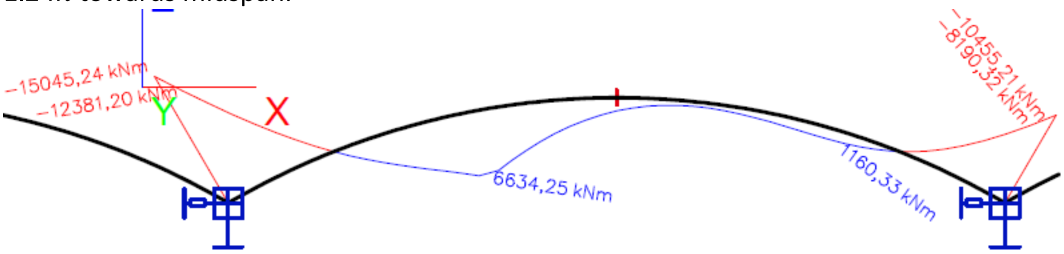

Figure 88: Bending moments middle span including tandem axle - linear

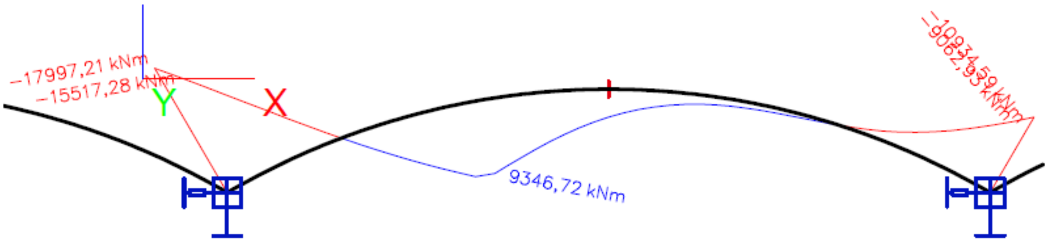

Figure 89: Bending moments middle span including tandem axle - nonlinear

Table 37: Middle span: characteristic values bending moment distribution – left half span

Middle span Model – tandem axle		$M_{hog-supp.left}$ [kNm]	$M_{sag-max}$ [kNm]	$M_{hog-supp.right}$ [kNm]
C&k low E_f	Linear	-15,045.2	+6,634.3	-10,455.2
	Non-linear	-17,997.2	+9,346.7	-10,934.6
	Difference	*-2,952.0*	*+2,712.4*	*-479.4*
	Factor	*1.20*	*1.41*	*1.05*
C&k low $2 \cdot E_f$	Linear	-20,847.3	+8,826.0	-16,632.7
	Non-linear	-21,431.1	+10,097.0	-16,290.7
	Difference	*-583.8*	*+1,271.0*	*+342.0*
	Factor	*1.03*	*1.14*	*0.98*
C&k high E_f	Linear	-12,041.5	+5,564.6	-7,250.6
	Non-linear	-14,208.4	+7,457.5	-6,985.4
	Difference	*-2,166.9*	*+1,892.9*	*+265.2*
	Factor	*1.18*	*1.34*	*0.96*
C&k high $2 \cdot E_f$	Linear	-14,747.6	+6,565.8	-10,231.7
	Non-linear	-15,432.8	+7,388.5	-9,949.6
	Difference	*-685.2*	*+882.7*	*+282.1*
	Factor	*1.05*	*1.13*	*0.97*

19.2.5 Middle span including geometrical imperfection

The geometrical imperfection (lowest buckling mode with amplitude of $22\ mm$), is only taken into account in the nonlinear analysis. The linear analysis is based on the perfect shape of the structure. Again only the left half span is displayed in the table.

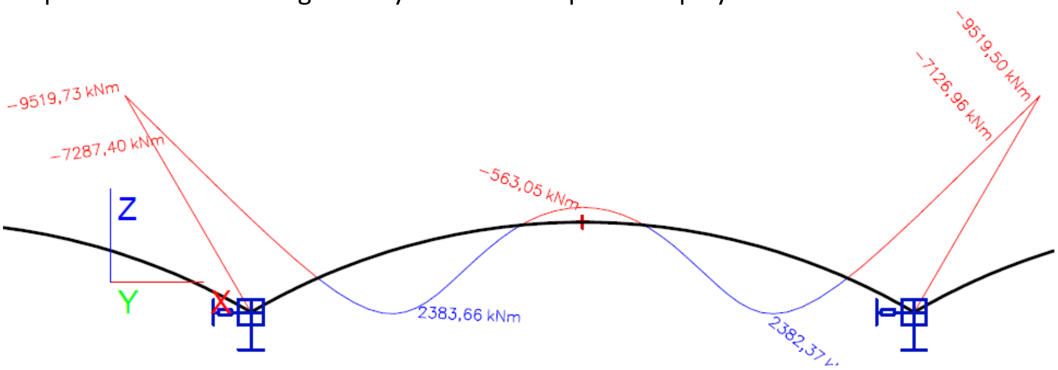

Figure 90: Bending moments middle span - linear

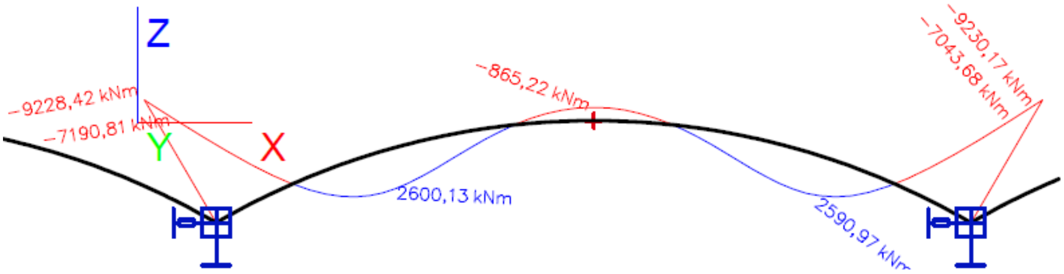

Figure 91: Bending moments middle span including geometrical imperfection - nonlinear

Table 38: Middle span: characteristic values bending moment distribution – left half span

Middle span Model		$M_{hog-supp.left}$ [kNm]	$M_{sag-max}$ [kNm]	$M_{hog-midspan}$ [kNm]
C&k low E_f	Linear	-9,519.7	+2,383.7	-563.1
	Non-linear	-9,228.4	+2,600.1	-865.2
	Difference	*+291.3*	*+216.4*	*-302.1*
	Factor	*0.97*	*1.09*	*1.54*
C&k low $2 \cdot E_f$	Linear	-14,893.9	+2,996.8	+2,059.4
	Non-linear	-12,914.1	+2,502.8	+719.9
	Difference	*+1,979.8*	*-494.0*	-1,339.5
	Factor	*0.87*	*0.84*	0.35
C&k high E_f	Linear	-7,572.7	+2,450.7	-1,509.2
	Non-linear	-8,070.6	+2,653.1	-1,681.3
	Difference	*-497.9*	*+202.4*	*-172.1*
	Factor	*1.07*	*1.08*	*1.11*
C&k high $2 \cdot E_f$	Linear	-9,616.5	+2,368.2	-538.2
	Non-linear	-9,500.3	+2,380.3	-575.4
	Difference	*+116.2*	*+12.1*	*-37.2*
	Factor	*0.99*	*1.01*	*1.07*

19.3 Concluding arch model without substructure

When comparing the (symmetrical) seven span models to the single arch models, two comparable situations occur. At the end span the flexible supported situation occurs and the middle span resembles the fully clamped arch, when comparing the bending moment distributions and deformations. Actually, these differences in confinement are the main reason to model multiple arches. As can be seen in Figure 97, the normal forces do increase towards the middle span, but the largest share of the horizontal thrust is excited in the end span. Since in the end span larger deformations occur, the bending moment magnification is the highest in the end span. Although the horizontal support stiffness at the end spans was tuned to resemble only intermediate spans in these 7 span models, the edge disturbance remains (deformation before horizontal thrust is excited), irrespectively of the modelled stiffness.

In the second span, the bending moments at the supports decrease in geometrically nonlinear analysis, when compared with linear analysis.

In the middle span, the small hogging moment in linear analysis is increased in geometrically nonlinear analysis, leading to large magnification factors.

The two extreme combinations in stiffness (low support stiffness, lower bound Young's modulus and high support stiffness and upper bound Young's modulus) lead to bending moments with the same order of magnitude. Combining low support stiffness with the upper bound Young's modulus, higher bending moments will be found, since higher curvature is required to follow the horizontal translations.

20. Analysis multiple arch models including substructure

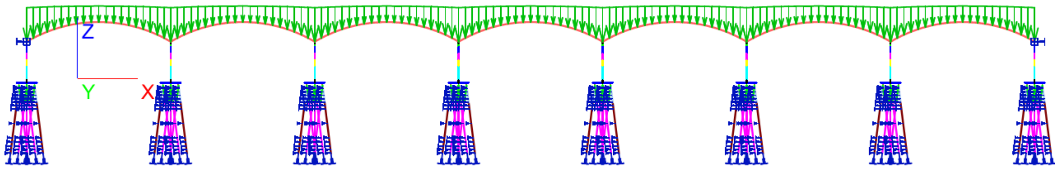

Figure 92: 7 span model with batter piles (piers number 3 and 6)

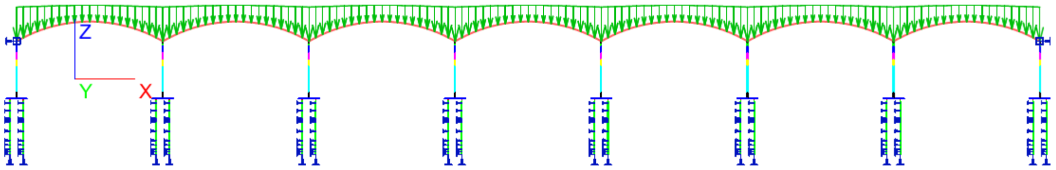

Figure 93: 7 span model with drilled piles (pier number 12)

20.1 Seven span models

In this analysis, the model is enlarged by adding the substructure. This substructure with foundation and support stiffnesses for the different soil layers is already modelled by BAM Infraconsult in design. The substructure and the additional data is added to the seven span models by simply copying part of the approach bridge structure into a new model for this investigation. All intermediate piers have different support stiffnesses due to different soil properties. Therefore, intermediate piers number 2 to number 12, are loaded by unit loads ($1{,}000 \text{ kN}$), to investigate the substructure stiffness and to select three piers for the structural analysis of the arched superstructure. The horizontal translation is displayed in Figure 94. The difference with the analysis in paragraph 19.1.2, is that in this analysis no stiffness values are required, but a choice is made for the piers that are modelled in the multiple arch models.

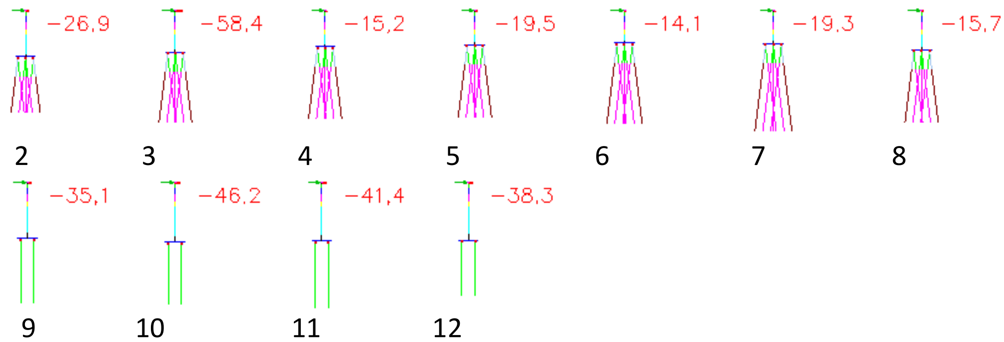

Figure 94: Horizontal translation piers city bridge due to unit loading, values in [mm]

For the piers with batter piles (the vibro pile system), translation varies mainly between 14 mm and 20 mm. Only piers number 2 and 3, suffer a much lower vertical soil stiffness and a much higher translation occurs. The drilled casing piles all have similar translations. To investigate the effect of the substructure stiffness on the bending moments in the arches, piers number 3, number 6 and number 12 will be analysed in the seven span model.

At the end spans, horizontal and rotational supports should be modelled to account for the adjacent spans. Since the intermediate piers at the end spans are modelled, the end support stiffness in Table 32, should be reduced. The most straightforward method is subtracting the intermediate pier stiffness from the end span stiffness. To obtain a lower bound value, the river bank pier stiffness is used (lowest value) and subtracted is the average stiffness of the piers on vibro piles (highest value), leading to:

$$k_{end} = (110 - 57) \cdot 10^3 = \quad 53{,}000 \text{ kN/m}$$
$$C_{end} = (8 - 4.9) \cdot 10^6 \quad = 3{,}100{,}000 \text{ kNm/rad}$$

Piers number 3, 6 and 12 are copied out of the approach bridge model and arches and loads are added. For the Young's modulus, both the upper and lower bound values will be investigated.

20.1.1 Bending moment distribution

As visualised in Figure 95, the bending moment distribution has a shape similar to the bending moment distribution that was found in the 7 span models without substructure (Figure 81). For the other investigated piers (№3 and №12), similar shaped bending moment distributions are found, although for the lower support stiffness, at mid span no hogging bending moments occur for the middle spans.

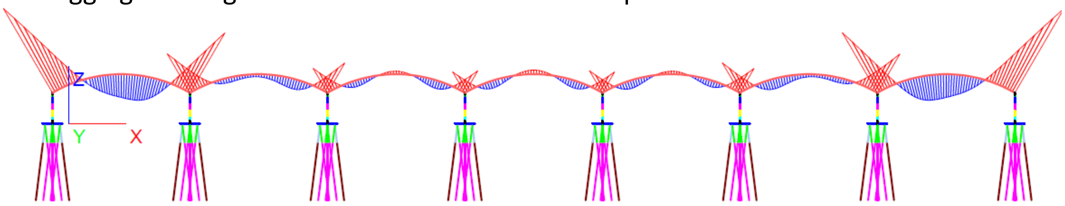

Figure 95: Bending moment distribution piers number 6, Ef

Since the bending moment distributions have similar shapes for the different analysed cases, only the extreme values of the bending moment distributions of the end and middle span are displayed in Table 39 en Table 40.

Table 39: Extreme values bending moment distribution [kNm] - Young's modulus: E_f

Bending moment	**Endspan** *Hog-left*	*Hog-right*	*Sagging*	**Middle span** *Hog-left*	*Sagging*	*Hog-mid*
№ 3 linear	-38,448	-23,955	10,660	-12,268	2,425	725
Nonlinear	-36,432	-28,767	15,740	-11,836	2,458	329
Factor	*0.95*	*1.20*	*1.48*	*0.96*	*1.01*	*0.45*
№ 6 linear	-32,023	-22,860	8,227	-7,982	2,386	-1,359
Nonlinear	-30,493	-25,988	11,809	-8,094	2,804	-2,093
Factor	*0.95*	*1.14*	*1.44*	*1.01*	*1.18*	*1.54*
№ 12 linear	-37,413	-24,795	10,319	-10,815	2,317	-90
Nonlinear	-36,178	-29,694	15,412	-10,029	2,510	-842
Factor	*0.97*	*1.20*	*1.49*	*0.93*	*1.08*	*9.36*

Table 40: Extreme values bending moment distribution [kNm] - Young's modulus: $2 \cdot E_f$

Bending moment	Endspan Hog-left	Hog-right	Sagging	Middle span Hog-left	Sagging	Hog-mid
№ 3 linear	-55,070	-30,276	16,813	-20,106	4,173	4,084
Nonlinear	-54,449	-32,390	20,076	-20,663	4,813	4,921
Factor	0.99	1.07	1.19	1.03	1.15	1.20
№ 6 linear	-45,680	-29,202	13,288	-10,598	2,282	-230
Nonlinear	-45,476	-31,865	15,939	-10,425	2,320	-512
Factor	1.00	1.09	1.20	0.98	1.02	2.23
№ 12 linear	-53,213	-31,243	16,206	-16,976	3,179	2,661
Nonlinear	-53,076	-34,367	19,482	-16,921	3,292	2,943
Factor	*1.00*	*1.10*	*1.20*	*1.00*	*1.04*	*1.11*

20.1.2 Geometrical imperfection

Eurocode EN1992-2 prescribes two geometrical imperfections for arch bridges, based on the first horizontal and the first vertical buckling modes. These buckling modes can be determined via stability analysis, but might be modelled as sine curves too. In the investigation, the imperfection is modelled by three half sine waves, representing the first vertical buckling mode, which is applied to all seven spans. This imperfection is affine with the deformations caused by the distributed load and therefore assumed to yield the governing combination of loads and imperfections, see Table 41.

Only in case the tandem axle system is located asymmetrically, for example at a quarter of the span, the horizontal (antisymmetrical) buckling mode is affine with the largest share of the deformations due to the load. Since the tandem axle system causes high second order bending moments when combined with the distributed load, this situation is investigated as well, see Table 42. For this analysis, the imperfection is modelled by two half sine waves. The imperfect shape of the arches is drawn manually in Scia Engineer, so that it is incorporated in both linear and nonlinear analysis. Using the predefined functions in Scia Engineer will only lead to geometrical imperfections in the nonlinear analysis.

Table 41: Bending moments for arches with symmetrical imperfection – tandem axle at $0.5\ L$

Bending moment	**Endspan** *Hog-left*	*Hog-right*	*Sagging*	**Middle span** *Hog-left*	*Sagging*
Geometrically perfect – substructure pier № 3 – Young's modulus E_f					
Linear	-38,448	-23,955	10,660	-12,268	2,425
Nonlinear	-36,432	-28,767	15,740	-11,836	2,458
Factor	*0.95*	*1.20*	*1.48*	*0.96*	*1.01*
Geometrically imperfect (symmetrical)					
Linear	-38,305	-23,749	11,182	-12,350	2,141
Nonlinear	-36,235	-28,594	16,739	-11,287	2,083
Factor	*0.95*	*1.20*	*1.50*	*0.91*	*0.97*
Geometrically perfect and tandem axle load at middle span 0.5 L					
Linear	-38,103	-23,407	10,521	-16,538	6,305
Nonlinear	-36,007	-28,259	15,544	-18,591	9,934
Factor	*0.94*	*1.21*	*1.48*	*1.12*	*1.58*
Geometrically imperfect (symmetrical) and tandem axle load at 0.5 L					
Linear	-37,955	-23,193	11,104	-16,178	7,295
Nonlinear	-35,645	-27,891	16,434	-17,964	11,282
Factor	*0.94*	*1.20*	*1.48*	*1.11*	*1.55*
Geometrically imperfect (symmetrical) and tandem axle at end span 0.5 L					
Linear	*-41,272*	*-27,152*	*16,129*	*-12,054*	*2,135*
Nonlinear	*-41,358*	*-34,697*	*25,192*	*-10,764*	*2,163*
Factor	1.00	1.28	1.56	0.89	1.01

Table 42: Bending moments for arches with symmetrical imperfection, middle span anti-symmetrical and tandem axle at $0.25\ L$

Bending moment	**Endspan** *Hog-left*	*Hog-right*	*Sagging*	**Middle span** *Hog-left*	*Sagging*
Geometrically perfect – substructure pier № 3 – Young's modulus E_f					
Linear	-38,448	-23,955	10,660	-12,268	2,425
Nonlinear	-36,432	-28,767	15,740	-11,836	2,458
Factor	*0.95*	*1.20*	*1.48*	*0.96*	*1.01*
Geometrically imperfect (antisymmetrical for middle span)					
Linear	-38,353	-23,826	11,205	-13,524	3,027
Nonlinear	-36,331	-28,709	16,788	-12,581	3,425
Factor	*0.95*	*1.20*	*1.50*	*0.93*	*1.13*
Geometrically perfect and tandem axle load at middle span 0.25 L					
Linear	-38,100	-23,402	10,520	-18,957	6,704
Nonlinear	-36,001	-28,252	15,541	-20,940	8,198
Factor	*0.94*	*1.21*	*1.48*	*1.10*	*1.22*
Geometrically imperfect and tandem axle load at 0.25 L					
Linear	-38,236	-23,639	11,149	-19,866	7,414
Nonlinear	-36,182	-28,531	16,711	-21,744	9,339
Factor	*0.95*	*1.21*	*1.50*	*1.09*	*1.26*

21. Approach bridge model

In the previous analyses, the seven span models, three piers were chosen (numbers 3, 6 and 12). Each of these chosen piers were used for a seven span model, leading to symmetrical models and symmetrical results. However, the approach bridge is not symmetrical, as can be seen in Figure 96. The end supports providing the confinement of the arches, are different, the intermediate supports have different pier heights and soil stiffness vary along the $700\ m$ long approach bridge.

Since the seven span models deviate from the approach bridge, a geometrically nonlinear analysis is carried out for the approach bridge model too. The model was made by BAM Infraconsult and is adapted to perform the nonlinear analysis. Since this analysis requires iterative solving for each load combination, the number of load combinations is reduced to fifteen. In these combinations, spans 1-2 to 15-16 are all loaded once by the tandem axle system.

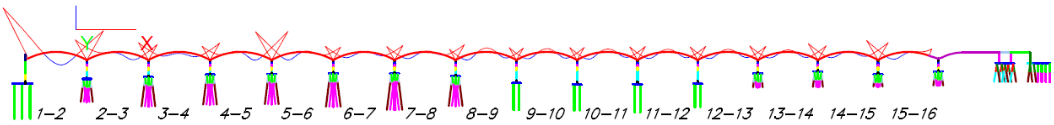

Figure 96: Example bending moment distribution - approach bridge model

21.1.1 Influence Young's modulus

First the influence of the Young's modulus on the bending moment magnification is investigated for permanent and distributed traffic load only.

Table 43: Characteristic values bending moment distribution approach bridge [kNm], Young's modulus $E_f = 12{,}718\ N/mm^2$

	Max. hogging bending moment			Max. sagging bending moment		
Span	Linear	Nonlinear	*Factor*	Linear	Nonlinear	*Factor*
1-2	-34,198	-32,926	*0.96*	5,464	7,832	*1.43*
2-3	-15,544	-12,249	*0.79*	2,925	3,413	*1.17*
3-4	-11,693	-11,330	*0.97*	1,769	1,829	*1.03*
4-5	-19,382	-20,169	*1.04*	3,647	4,159	*1.14*
5-6	-19,159	-19,957	*1.04*	3,574	4,142	*1.16*
6-7	-10,618	-10,033	*0.94*	1,946	2,226	*1.14*
7-8	-11,467	-10,751	*0.94*	2,264	2,723	*1.20*
8-9	-9,193	-8,674	*0.94*	2,508	3,240	*1.29*
9-10	-9,466	-9,368	*0.99*	2,123	2,525	*1.19*
10-11	-10,209	-9,872	*0.97*	2,321	2,728	*1.18*
11-12	-10,166	-9,935	*0.98*	2,092	2,412	*1.15*
12-13	-10,327	-9,916	*0.96*	2,107	2,413	*1.15*
13-14	-10,806	-10,324	*0.96*	1,980	2,158	*1.09*
14-15	-13,059	-12,246	*0.94*	2,162	2,201	*1.02*
15-16	-14,042	-14,201	*1.01*	2,972	3,560	*1.20*

Table 44: Characteristic values bending moment distribution approach bridge [kNm], $2 \cdot E_f = 25.000 N/mm^2$

	Max. hogging bending moment			Max. sagging bending moment		
Span	Linear	Nonlinear	*Factor*	Linear	Nonlinear	*Factor*
1-2	-42,191	-41,043	*0.97*	7,679	9,031	*1.18*
2-3	-22,063	-19,925	*0.90*	4,212	4,822	*1.14*
3-4	-15,454	-15,272	*0.99*	2,216	2,555	*1.15*
4-5	-21,194	-21,855	*1.03*	3,966	4,388	*1.11*
5-6	-21,044	-21,498	*1.02*	3,572	3,842	*1.08*
6-7	-11,724	-11,522	*0.98*	2,008	2,072	*1.03*
7-8	-12,482	-12,060	*0.97*	2,518	2,752	*1.09*
8-9	-9,075	-8,668	*0.96*	2,622	3,093	*1.18*
9-10	-9,012	-8,780	*0.97*	2,165	2,385	*1.10*
10-11	-10,305	-9,848	*0.96*	2,646	2,909	*1.10*
11-12	-10,183	-9,794	*0.95*	2,245	2,420	*1.08*
12-13	-10,653	-10,118	*0.96*	2,311	2,478	*1.07*
13-14	-11,369	-10,877	*0.96*	2,101	2,167	*1.03*
14-15	-14,062	-13,591	*0.97*	2,353	2,343	*1.00*
15-16	-13,897	-13,917	*1.00*	3,235	3,656	*1.13*

21.1.2 Bending moments including tandem axle loading

The tandem axle load leads to high bending moments and relatively low normal forces. Second order bending moments due to the tandem axle load itself are small. However, when combined with the other loads, higher normal forces occur together with relatively large deformations due to the tandem axle load. In the combination of distributed loads and the tandem axle system, higher second order bending moments are to be expected. It is investigated with the same approach bridge model, only now the loads are extended with the tandem axle load at a quarter of the arch span. This load is investigated on each span, thus 15 load combinations are analysed. Furthermore, temperature load (cooling) and shrinkage are added, both leading to downward deformations. The sagging bending moments at the tandem axle loads are displayed in Table 45.

Table 45: Sagging bending moments at tandem axle load [kNm] $E_f = 12.718\ N/mm^2$

	Max. sagging bending moment		
Span	Linear	Nonlinear	*Factor*
1-2	6,892	9,905	*1.44*
2-3	4,060	4,391	*1.08*
3-4	5,076	5,823	*1.15*
4-5	4,053	4,363	*1.08*
5-6	6,756	8,110	*1.20*
6-7	5,255	6,405	*1.22*
7-8	5,556	6,840	*1.23*
8-9	5,397	6,705	*1.24*
9-10	5,145	6,353	*1.23*
10-11	5,341	6,576	*1.23*
11-12	5,157	6,294	*1.22*
12-13	5,139	6,200	*1.21*
13-14	5,081	6,092	*1.20*
14-15	5,415	6,475	*1.20*
15-16	6,672	8,056	*1.21*

Geometrical imperfection

The geometrical imperfection is investigated for the approach bridge model by manually changing the nodal coordinates. Both the two and three half sine wave imperfections are investigated once. The two half wave imperfection applied to span 6-7 is combined with the tandem axle load at a quarter of the span and the three half wave imperfection applied to span 3-4 is combined with the tandem axle load at mid span.

Table 46: Results span 3-4

Analysis	**Perfect**	**Imperfect**	ΔM
Linear	6,640	7,719	1,079
Nonlinear	10,453	12,280	1,827
	1.57	1.59	

Table 47: Results span 6-7

Analysis	**Perfect**	**Imperfect**	ΔM
Linear	5,255	5,711	486
Nonlinear	6,405	7,184	779
	1.22	1.26	

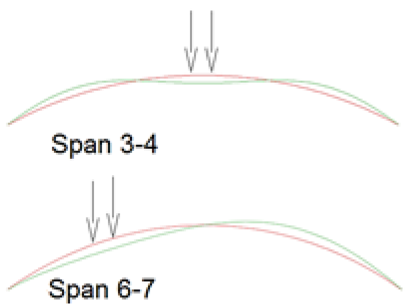

22. Conclusion multiple arch analysis

Geometrical imperfections do not lead to much higher magnification factors, when comparing the perfect shape first and second order with the imperfect first and second order analysis. However, the bending moments are higher for the imperfect model. When considering magnification factors, in which the geometrical imperfection is accounted for much higher bending moment magnification factors are found. Especially when considering the tandem axle loading and the geometrical imperfection at the end span, combined with the internal forces and deformations due to the distributed loads.

Figure 97 illustrates the end span being critical, since the normal force is exited largely, but the deformations are still large due to the relatively low degree of confinement.

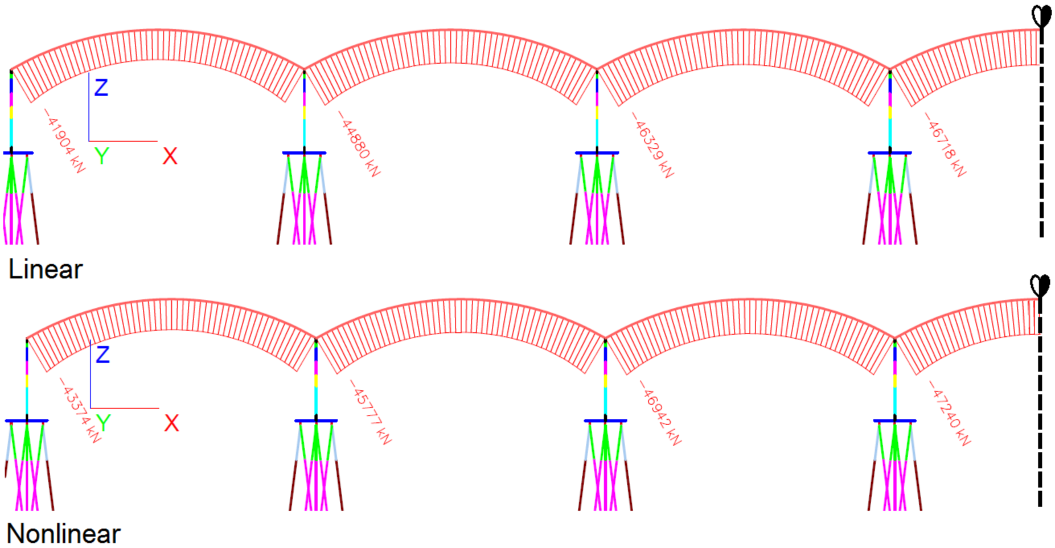

Figure 97: Normal force distribution

Part 4: Introduction to physical nonlinearity and 3D effects

Contents – Part 4: Introduction to physical nonlinearity and 3D

23. Introduction to Part 4

Physically nonlinear behaviour and the transverse load distribution could not be investigated in this thesis thoroughly due to time constraints. However, a brief introduction to both phenomena is provided in this part. It demonstrates the influence of the physical nonlinearity and the transverse load distribution and it provides a first step for future research.

The influence of cracking at the supports is investigated by reducing the Young's modulus of the material. Fictitious Young's moduli are derived with M-N-κ diagrams and implemented in the structural model. Only the support regions are assumed to crack, the rest of the span is modelled by the uncracked stiffness of the cross-section.

The transverse load distribution can only be investigated with a three dimensional finite element model. Point supports or line supports and transverse prestressing determine the transverse load distribution. A single arch is modelled with shell elements and the effect of the support condition and the prestress is displayed. The results are checked with two dimensional beam models.

24. Physically nonlinear analysis

Structural behaviour of arches is determined by stiffnesses. Material stiffness and soil stiffness are the two parameters that have a large impact on the internal forces. In arches, the soil stiffness and axial stiffness determine the normal forces and the translation of the arch. The bending stiffness regulates the deformations and bending moments ensure the compatibility of deformations and boundary conditions.

In the analysis, a high Young's modulus will result in high first order bending moments and small deformations. Small deformations will result in low second order bending moments. When a low Young's modulus is modelled, higher deformations will result in higher second order bending moments, but the first order bending moments are much lower. A lower Young's modulus leads to lower bending moments, even when including the geometrically nonlinear effect.

In design, the cross-sectional stiffness is modelled by a fictitious Young's modulus and a linear elastic cross-section. According to the Dutch national annex to NEN-EN-1992-1-1, the Young's modulus is reduced to include the effects of creep, cracking and axial forces. However, this formula leads to a relatively low Young's modulus, which is a safe approach when checking maximum deformations, but might be too favourable for the computation of the internal forces. Nevertheless, in arched structures, underestimating the Young's modulus and thus underestimating bending moments will lead to cracking. After cracking the Young's modulus decreases and the bending moments will decrease as well. The realistic Young's modulus is thus mainly required to check durability requirements.

A true physically nonlinear analysis is not carried out in this investigation. A physically nonlinear analysis requires time for modelling and computation, in which internal forces and material stiffnesses should converge according to the physically nonlinear relation. Time for the physically nonlinear analysis lacks, but the principles will be demonstrated in this chapter to provide insight into the effect and to serve as a prelude for further investigation.

In the two dimensional approach bridge model, the fictitious Young's modulus is adapted, based on the M-N-κ theory. The high bending moments at the supports are assumed to cause cracking and the fictitious Young's modulus is decreased manually in the support region. The mid part is assumed not to crack and accordingly the high initial stiffness is applied.

24.1 Fictitious Young's modulus via M-N-κ relation

According to the Dutch national annex to Eurocode 2, the fictitious Young's modulus might be approximated by $E_f = \{2.20 + 440\rho + (24.0 + 220\rho) \cdot \alpha_n\} \cdot 10^3 \geq 5{,}000$. This formula provides a good approximation for the Young's modulus, when creep, cracking and axial forces should be accounted for. However, in arch analysis, the lower Young's modulus due to creep leads to underestimation of the bending moments. Furthermore, it only provides information on the combination of axially loaded cracked cross-sections. Uncracked cross-sections combined with an axial load cannot be evaluated with the formula.

24.1.1 M-N-κ theory

The bending moment curvature relation is programmed in a spreadsheet, including the effect of normal force. The diagram is based on four points, which follow the characteristic steps in the nonlinear behaviour of the cross-section. First the curvature is determined for the cracking bending moment of the uncracked cross-section (Figure 98). After cracking two situations are possible, first the compressive yield strain of the concrete is reached or the tensile reinforcement reaches the yield strength. It is assumed that for the arch loaded by axial compression, the concrete compressive yield strain is reached first (Figure 99). For the third point, the steel yield strain is reached in the tensile reinforcement (Figure 100). The last point represents the ultimate bending moment, in which the ultimate yield strain in the concrete is reached (Figure 101).

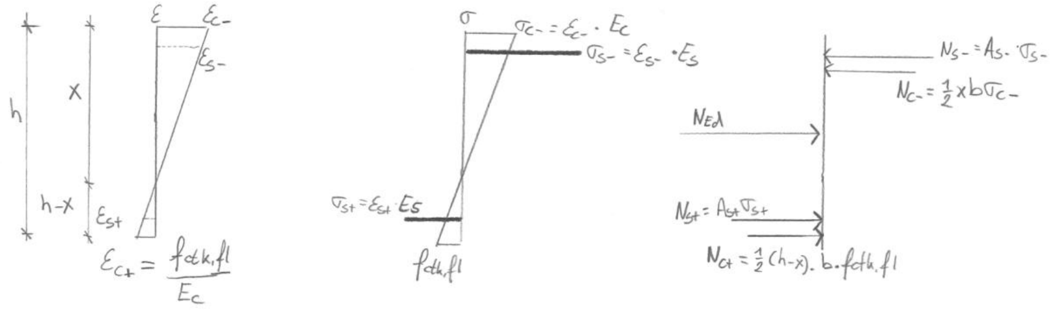

Figure 98: M-N-κ at the cracking bending moment

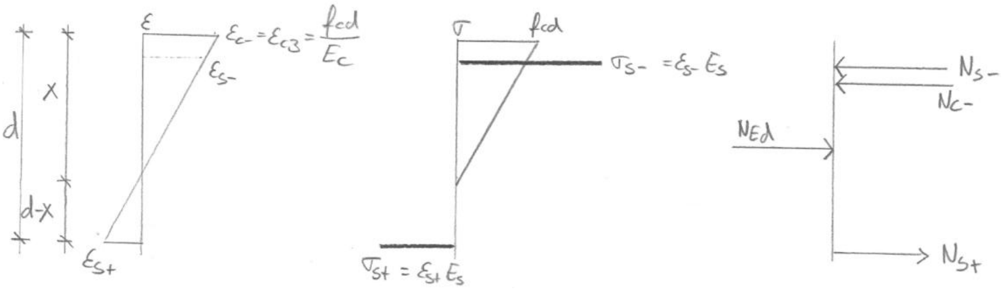

Figure 99: M-N-κ for reaching the compressive yield strain

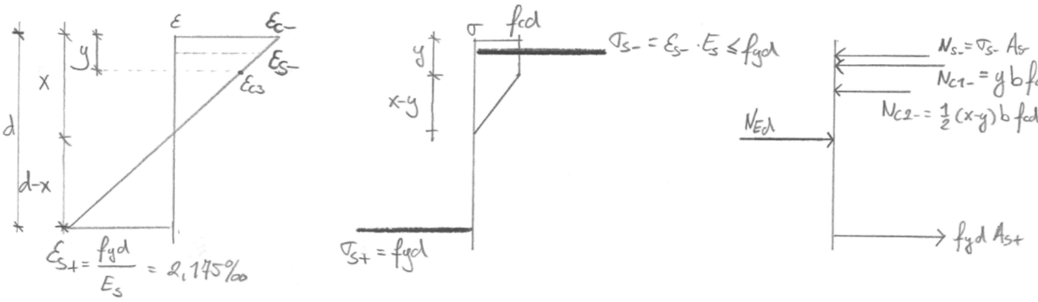

Figure 100: M-N-κ for the elastic bending moment Me (yielding of concrete and reinforcement)

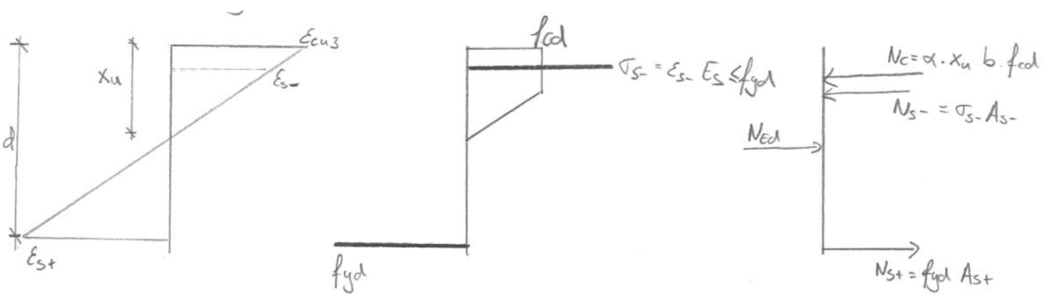

Figure 101: M-N-κ at the ultimate bending moment

The four computations follow the same recipe. Each point on the M-N-κ diagram follows from a characteristic strain. The other strains can be computed by geometrical mathematics, once the position of the neutral axis is known. Then Hooke's law ($\sigma = E \cdot \varepsilon$) is applied to obtain the stress distribution. Based on horizontal equilibrium, which includes the axial force, the position of the neutral axis can be determined. This is iteratively solved in the spreadsheet by using the goal seek function, which performs a Newton-Raphson approximation. Once horizontal equilibrium is satisfied, the accessory bending moment can be computed. Curvature follows from the slope of the strain diagram. Then the fictitious stiffness is computed, based on the area moment of inertia of the uncracked cross-section, $E_f = M/(\kappa \cdot I_{uncracked})$.

The M-N-κ diagram is determined for the two cross-sectional heights, $h = 500$ mm and $h = 1{,}000$ mm. Concrete strength, reinforcement and cover are all applied according to the city bridge design. For the compressive axial force, $N = 50{,}000$ kN is used, leading to upper bound values for the fictitious Young's modulus, which is a safe approximation.

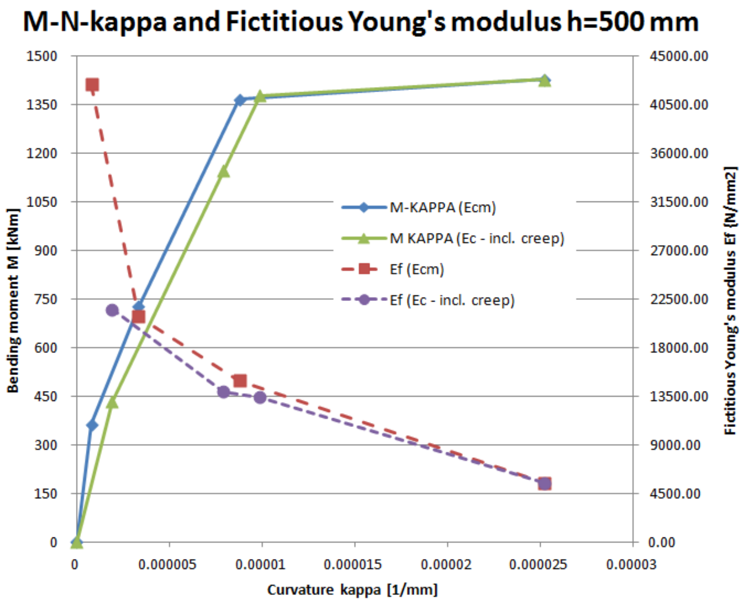

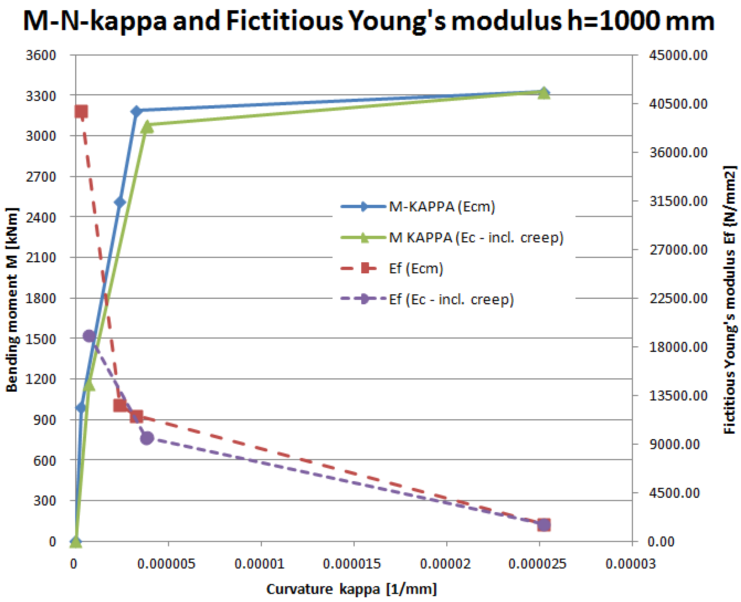

Figure 102: M-N-κ diagrams for h=500 and h=1,000

Creep effect

In the derivation of the M-N-κ formulae, a bi-linear stress-strain relation is used. In Eurocode 2 (1992-1-1), the prescribed concrete compressive yield strain $\varepsilon_{c3} = 1.75‰$ and yield stress f_{cd} imply a reduced Young's modulus $E_c = f_{cd}/\varepsilon_{c3} = 13.333\ \mathrm{N/mm^2}$. This Young's modulus is a rough approximation of the material stiffness including creep reduction, but it is not the most accurate approximation. However, it can be used in linear analysis to check strength criteria. It is not suitable to compute deformations or to use it in geometrically nonlinear analysis. It is better to adapt the bi-linear diagram to the initial stiffness E_{cm} and the reduced stiffness $E_{cm}/(1+\varphi)$ and thus obtaining the strains ε^*_{c3} and $\varepsilon^*_{c3,\ creep}$. The concrete yield stress f_{cd} is kept constant. The two properties of the applied C35/45 concrete are: $f_{cd} = 35/1.5 = 23.33\ \mathrm{N/mm^2}$ and $E_{cm} = 34{,}000\ \mathrm{N/mm^2}$.

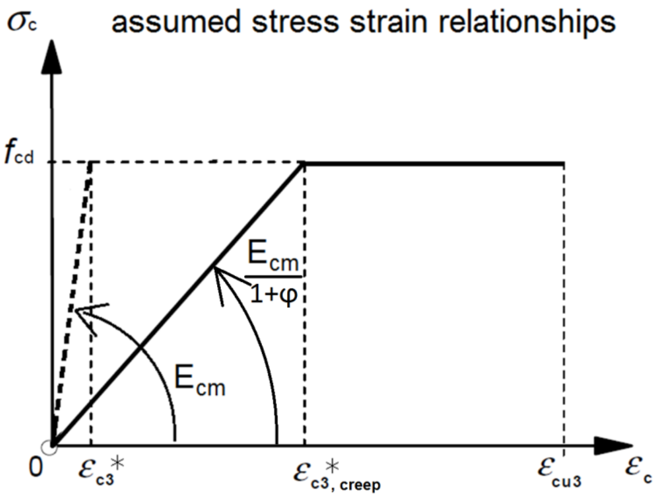

Figure 103: Adapted bi-linear stress-strain diagram

In the diagram, the yield strains are determined via:

$$\varepsilon^*_{c3} = \frac{f_{cd}}{E_{cm}} = \frac{23.33}{34{,}000} = 0.69\ ‰$$

$$\varepsilon^*_{c3,\ creep} = \frac{f_{cd}(1+\varphi(t,t_0))}{E_{cm}} = \frac{23.33 \cdot (1+1.558)}{34{,}000} = 1.76‰$$

In part 1, the creep coefficient is determined, $\varphi(t_{100\,\mathrm{y}}, t_{28\,d}) = 1.558$. For this creep factor, the strains are almost equal, 1.75‰ and 1.76‰. This is a coincidence. In case one of the many creep parameters is changed, the strains will differ. The mean Young's modulus is not reduced to a design value (E_{cd}), since a lower Young's modulus will result in lower bending moments.

24.1.2 Fictitious stiffnesses following from M-N-κ analysis

The results of the analysis are displayed in the graphs of Figure 102. The values of the fictitious stiffnesses are displayed in Table 48. For the uncracked stiffness, the first model is used, see Figure 98. The cracked stiffness is computed according to the model in Figure 100, which represents the lowest secant stiffness before the tensile reinforcement yields.

Table 48: Fictitious stiffnesses

E_f [N/mm²]	UNCRACKED		CRACKED	
	$h = 500$	$h = 1{,}000$	$h = 500$	$h = 1{,}000$
Creep included	21,545	19,074	13,387	9,604
Creep not included	42,323	39,832	14,927	11,623

Due to the increasing height at the support, weighted averages for the fictitious Young's moduli are computed based on the average height of the cross-section.

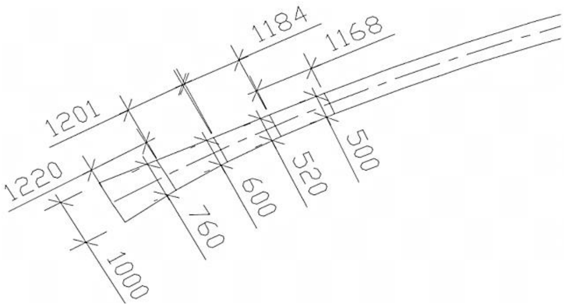

Figure 104: Arch geometry at support

A linearly weighted average height is used to compute the weighted fictitious Young's modulus:

$$h_{average} \approx \frac{500 + 520 + 600 + 760 + 1000}{5} = 676 \text{ mm}$$

$$factor\ 1 = \frac{676 - 500}{1000 - 500} = 0.352$$

$$factor\ 2 = \frac{1000 - 676}{1000 - 500} = 0.648$$

Weighted fictitious Young's moduli – support region

$E_f = 0.648 \cdot 21{,}545 + 0.352 \cdot 19{,}074 = 20{,}675 \text{ N/mm}^2$
$E_f = 0.648 \cdot 42{,}323 + 0.352 \cdot 39{,}832 = 41{,}446 \text{ N/mm}^2$
$E_f = 0.648 \cdot 13{,}387 + 0.352 \cdot 9{,}604 = 12{,}055 \text{ N/mm}^2$
$E_f = 0.648 \cdot 14{,}927 + 0.352 \cdot 11{,}623 = 13{,}764 \text{ N/mm}^2$

These stiffnesses are combined with the uncracked fictitious stiffness in the span, as displayed in Table 49 and

Table 49: Fictitious Young's moduli for FE analysis

E_f [N/mm²]	Span	Support	
	UNCRACKED	UNCRACKED	CRACKED
Creep included	21,545	20,675	12,055
Creep not included	42,323	41,446	13,764

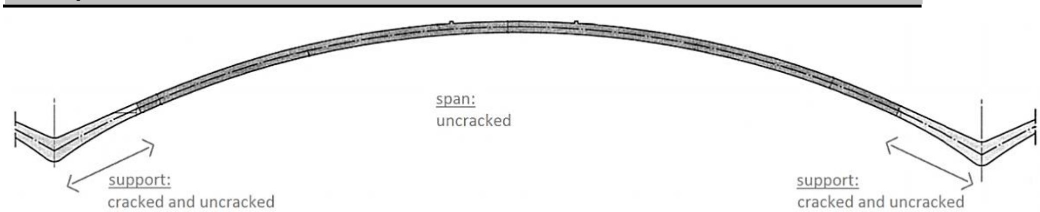

Figure 105: Cracked and uncracked zones

24.2 Results structural analyses

The influence of cracked cross-sections at the supports and the influence of creep is investigated with the approach bridge model. It is loaded by permanent load, temperature load, distributed traffic load and the tandem axle load at mid span of span 3-4. This loading is combined with the three half sine wave imperfection at span 3-4. The results are displayed in Table 50. In this table, the maximum hogging and sagging bending moments are displayed for each span. The hogging bending moments at the supports decrease when cracking is taken into account by 15% when creep is taken into account and over 30% in case the stiffness without the creep effect is investigated. The sagging bending moments increase only little (or even decrease). The increase at mid span is 10% to 20% compared to the decrease at the supports. The lower bending stiffness of the arches due to cracking and creep leads to lower bending moments. The decrease of bending moments is compensated by higher normal forces.

Table 50: Results structural analysis approach bridge model

M [kNm]		**Creep not included**		**Creep included**	
		Uncracked	Cracked	Uncracked	Cracked
1-2	Support	-57,710	-41,299	-42,012	-36,681
	Span	11,972	12,596	8,923	9,190
2-3	Support	-36,233	-21,524	-20,062	-15,309
	Span	7,046	5,885	4,333	4,288
3-4	Support	-34,058	-22,677	-23,560	-19,992
	Span	14,583	13,603	12,126	11,834
4-5	Support	-34,618	-23,080	-25,548	-21,625
	Span	5,525	5,081	3,756	3,933
5-6	Support	-34,823	-22,294	-25,609	-21,459
	Span	4,954	5,350	3,970	4,526
6-7	Support	-23,831	-15,109	-16,237	-13,419
	Span	3,885	2,914	2,259	2,340
7-8	Support	-24,447	-15,977	-16,912	-14,250
	Span	3,562	3,222	2,567	2,711
8-9	Support	-19,991	-12,413	-13,880	-11,488
	Span	1,849	2,392	2,033	2,470
9-10	Support	-19,677	-12,370	-14,162	-11,841
	Span	1,634	2,005	1,567	1,948
10-11	Support	-21,690	-13,717	-15,135	-12,671
	Span	2,412	2,592	2,017	2,316
11-12	Support	-21,691	-13,677	-15,204	-12,707
	Span	2,216	2,302	1,723	2,036
12-13	Support	-23,001	-14,368	-15,639	-12,986
	Span	2,565	2,489	1,838	2,108
13-14	Support	-25,322	-15,832	-16,964	-13,968
	Span	3,198	2,725	1,947	2,096
14-15	Support	-31,079	-20,561	-21,092	-17,652
	Span	5,057	4,293	3,050	2,992
15-16	Support	-28,420	-18,359	21,532	-18,077
	Span	6,790	6,596	5,371	5,540

Tandem axle load

The sagging bending moment in span 3-4 reduces when cracking is taken into account. This is highly advantageous, since it is the bending moment at the tandem axle loading that decreases. The envelope of the sagging bending moments is composed mainly by the bending moments due to these point loads. Reducing the stiffness at the support is thus not only beneficial at the support region, but reduces bending moments in the other areas as well.

25. Three dimensional modelling

The previous analyses, in which the geometrically nonlinear behaviour of the arched structure were investigated, are based on two dimensional models. In these models, the structure is represented by one dimensional beam elements. In two dimensional modelling, the load distribution in transverse direction is neglected. The concrete arches are actually curved plates or shells, in which bending in two direction occurs, due to twisting rigidity and the point supports. The geometry is displayed in Figure 106.

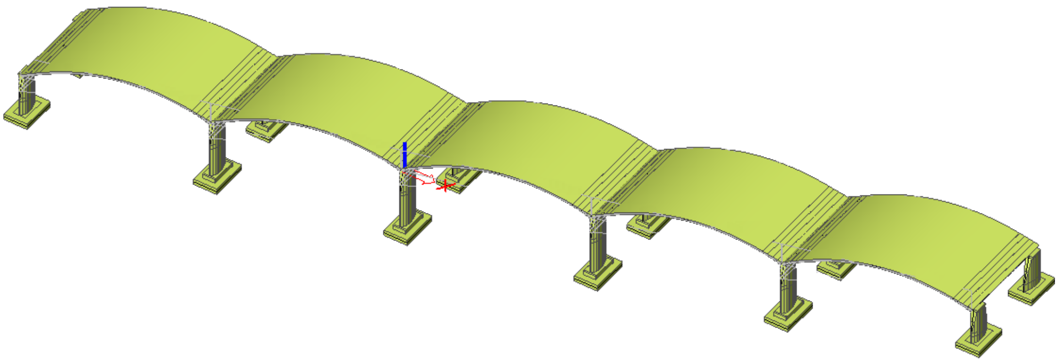

Figure 106: Three dimensional view of approach bridge design

In this chapter there will be a brief overview of the differences between the beam model, a line supported shell model and a point supported shell model. A complete analysis of the approach bridge in three dimensional models has to be left for future research, due to time constraints.

25.1 Models

To provide some insight in the differences between the two dimensional and three dimensional behaviour of the structural concept, the point supported arches, four models are analysed and compared:

- Two dimensional beam model of a single arch
- Three dimensional shell model of a single line supported arch
- Three dimensional shell model of a single point supported arch (Figure 107)
- Three dimensional shell model of a single point supported arch, including the transverse prestressing (Figure 108)

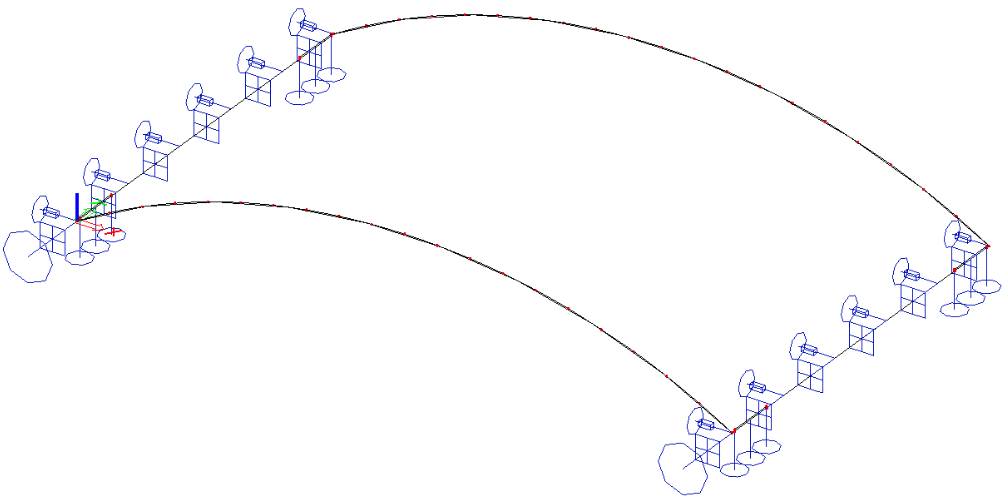

Figure 107: Point supported arch model

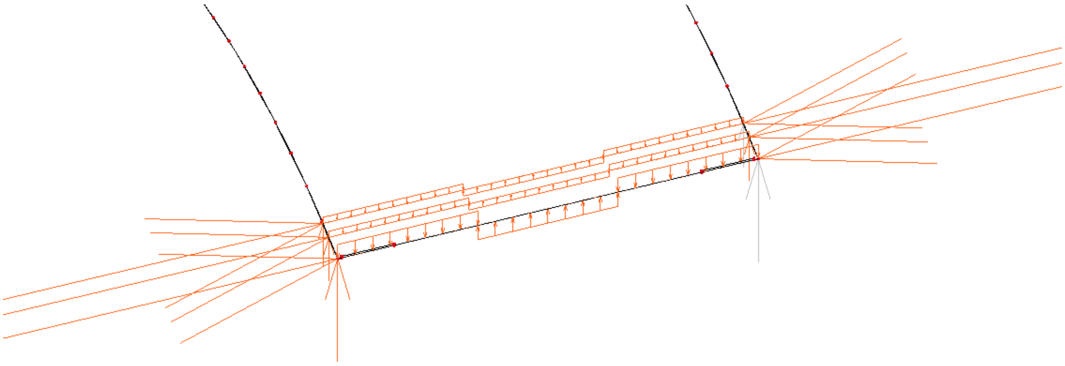

Figure 108: Prestress loading at hidden transverse beam

To obtain insight in the structural differences, the loads, the Young's modulus, the cross-section and the geometrical imperfection should be similar for the different models. The loads are applied as stated in part 1, including permanent load (self-weight, dead weight and shrinkage), traffic load LM1, temperature differences and prestress load, see chapter 7. Since the loads are represented as realistic as possible, there will occur a difference between the two and three dimensional models. Parapets, barriers, mixed aggregates, traffic load and prestress cause uneven loading over the width of the bridge.

The geometrical imperfection is included in the shape of the model. The three wave sine imperfection with a $22\ \mathrm{mm}$ amplitude is applied. The fictitious Young's modulus is applied based on the uncracked cross-section and including creep, leading to $E_f = 21.545\ \mathrm{N/mm^2}$. The increasing cross-sectional height near the support is not modelled.

For the supports, translational and rotational springs are implemented in the models, see Figure 107. In the two dimensional model, translational stiffness $k = 1{,}000\ \mathrm{MN/m}$ and rotational stiffness $C = 3{,}000\ \mathrm{MNm/rad}$ are applied. In the three dimensional models, these stiffnesses are adapted to line stiffnesses $k = 40\ \mathrm{MN/m^2}$ and $C = 120\ \mathrm{MNm/m/rad}$.

25.2 Results

In this paragraph, the results of the analyses are shown. Note that the internal forces are shown in the directions of the local axis system, while the global axis system is displayed in the figures.

25.2.1 Normal forces in global x-direction

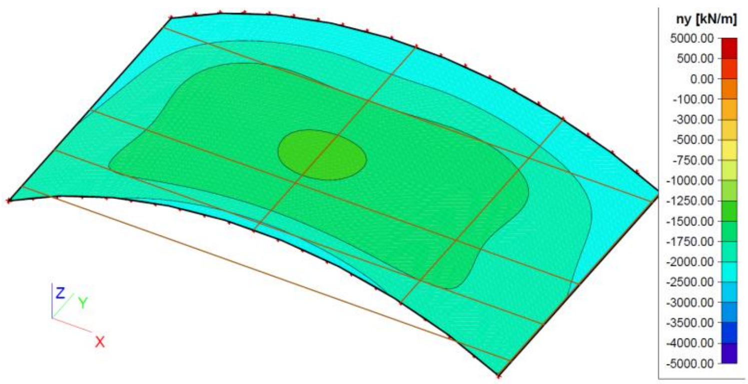

Figure 109: Normal forces - line support

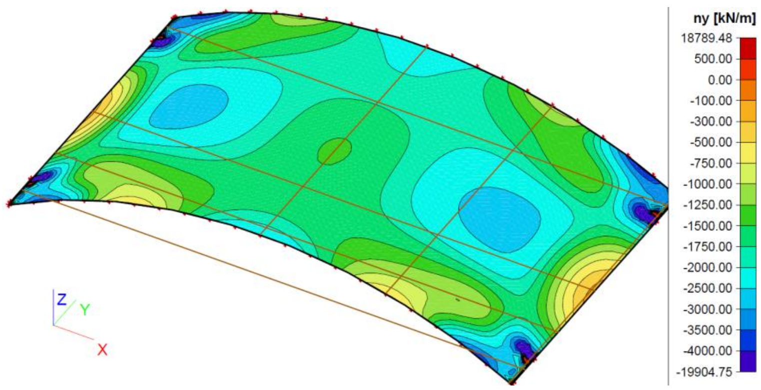

Figure 110: Normal forces - point support

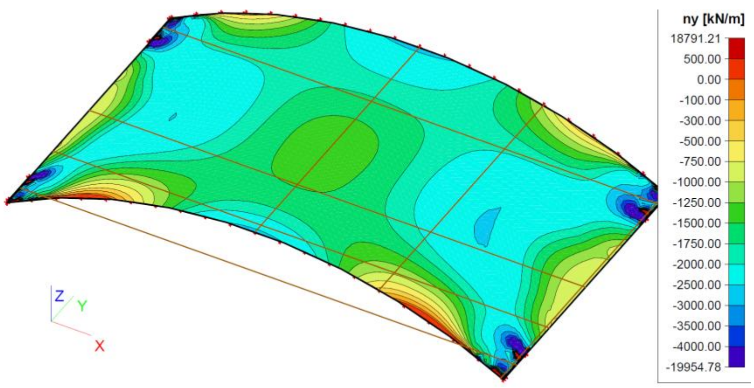

Figure 111: Normal forces - point support including transverse prestress

In Figure 111, the tensile forces in longitudinal direction near the edges are caused by the prestress load in transverse direction. In construction phasing, the hidden transverse beams are cast and prestressed first. Afterwards the arches are cast to these prestressed beams. Due to creep, some of these tensile forces will occur, but the force will be much smaller than computed in this model.

25.2.2 Bending moments – around global y-axis

Line Support

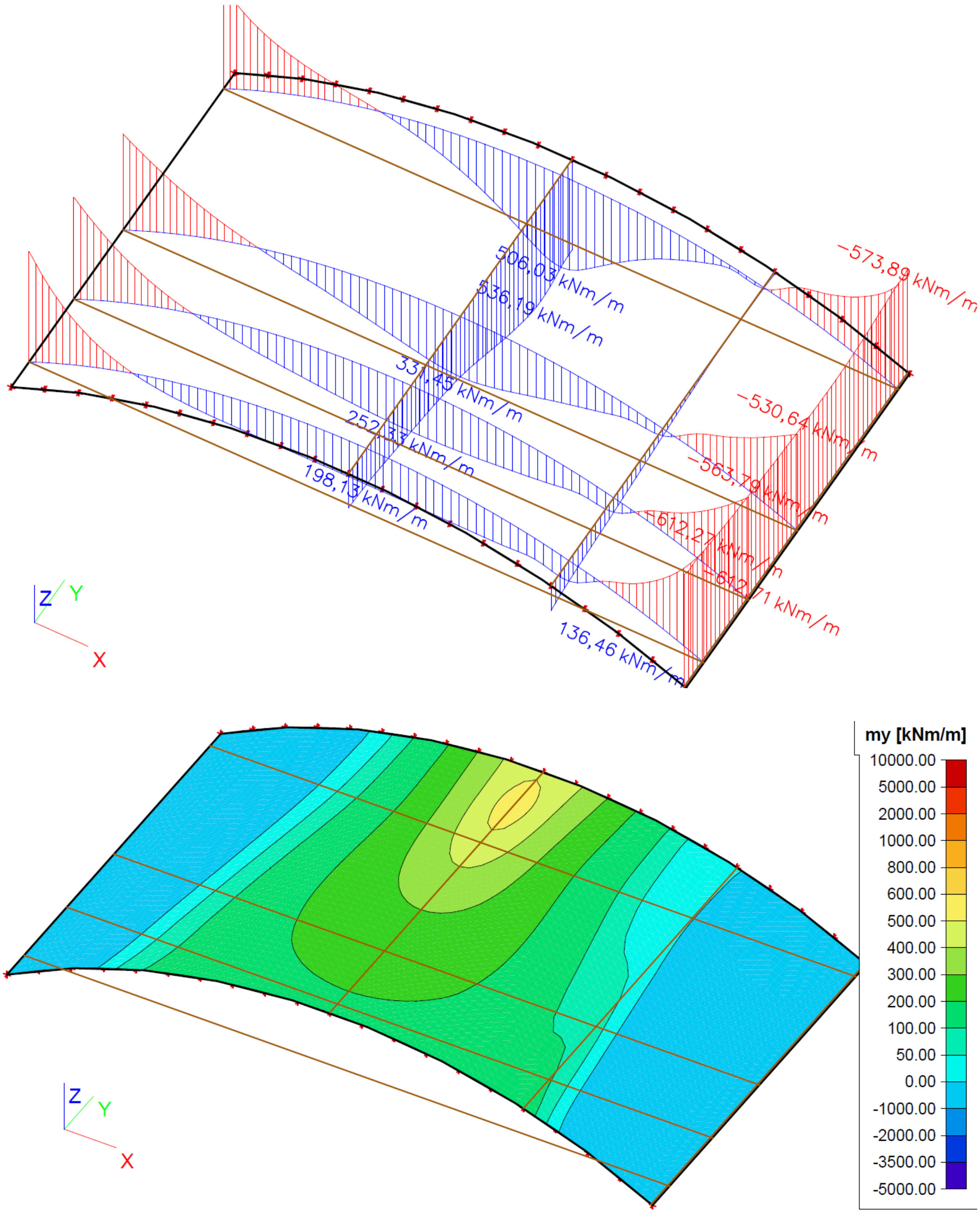

Figure 112: Bending moments - line support

The arches with line supports only benefit a transverse load spread of the tandem axle loads. These loads are applied eccentrically at the arch crown, to display the effect. For line supported arches, there are no large benefits in modelling the structure in three dimensions.

Point support

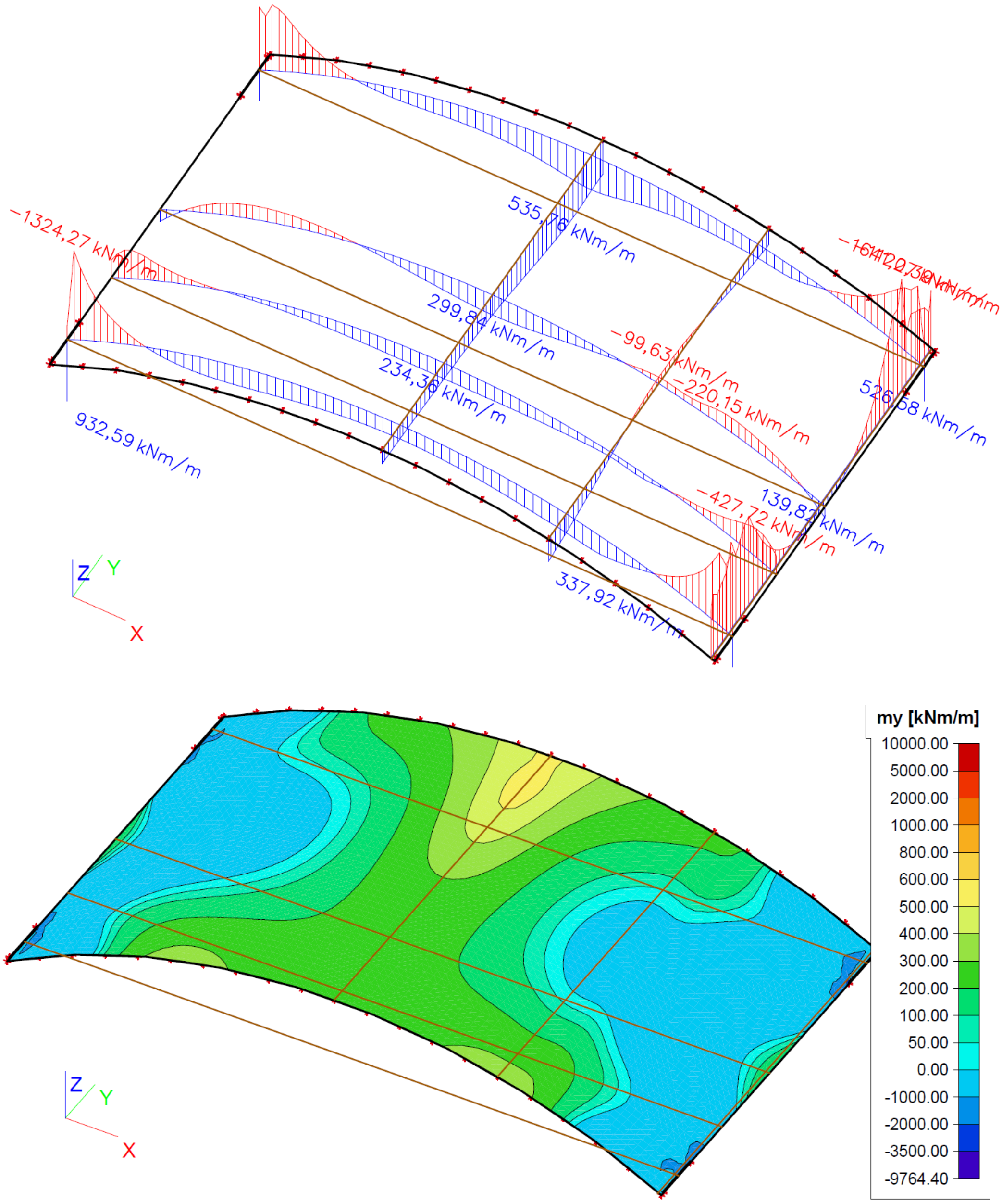

Figure 113: Bending moments - point support

Point support including transverse prestress

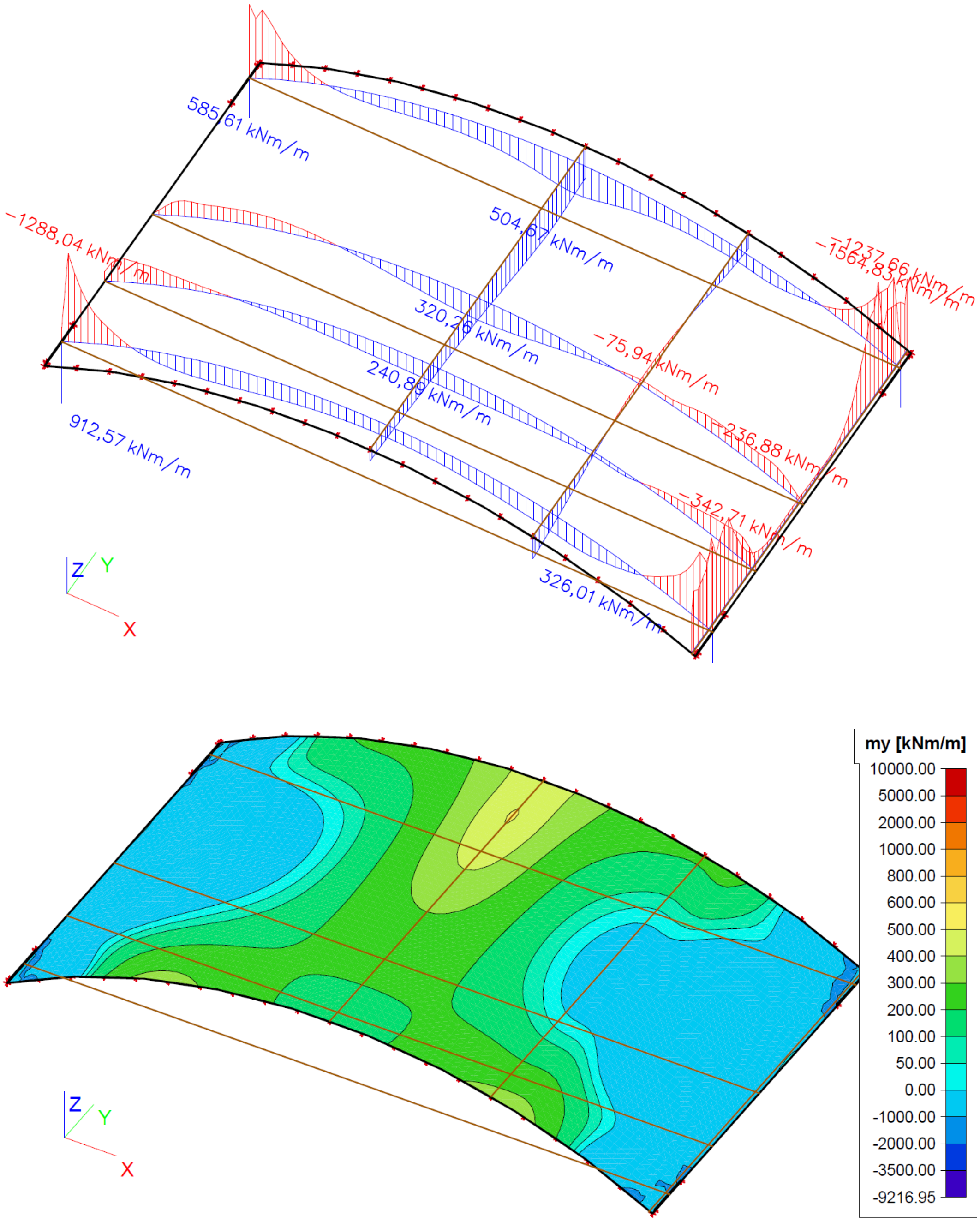

Figure 114: Bending moments - point support including transverse prestress

25.3 Check two dimensional analysis

In the finite element program, the internal forces on plates and shells can be displayed along internal lines. One of the options is to display the average value of the internal forces. In the figures, the average bending moment per unit width is displayed for the bending moments around the global y-axis.

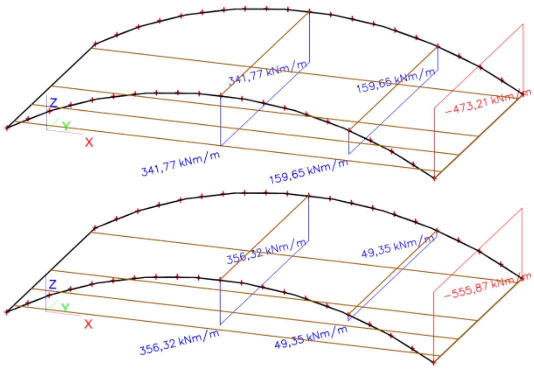

Figure 115: Average bending moments - line support - linear (l) and geometrically nonlinear (r)

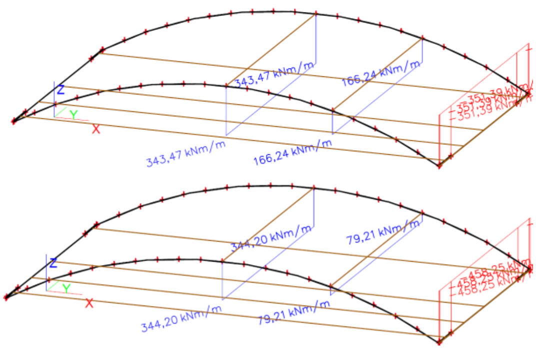

Figure 116: Average bending moments - point support - linear (l) and geometrically nonlinear (r)

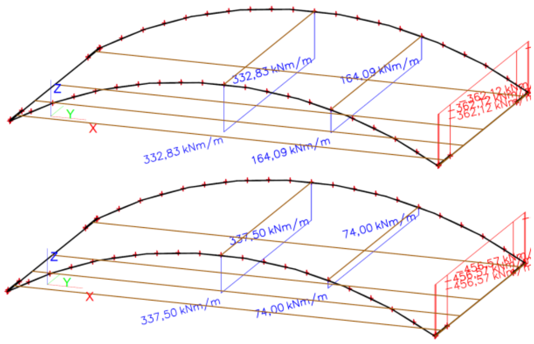

Figure 117: Average bending moments – including transverse prestress – linear (l) and geometrically nonlinear (r)

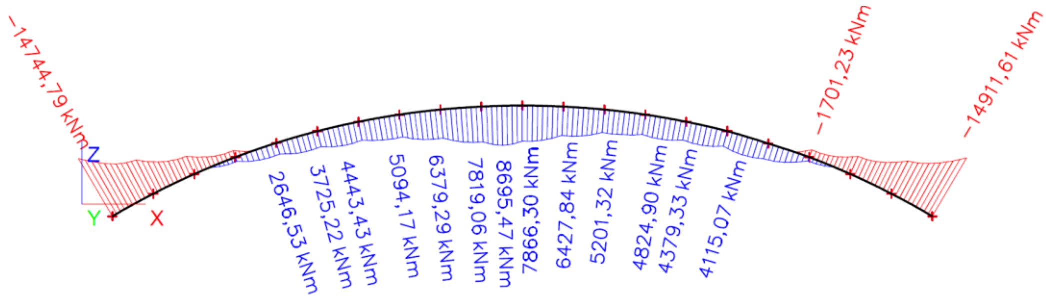

Figure 118: Bending moments two dimensional beam model - linear

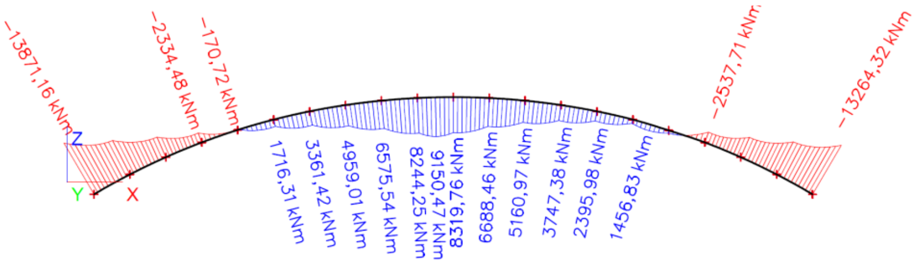

Figure 119: Bending moments two dimensional beam model - geometrically nonlinear

Table 51: Overview bending moments

Bending moments M [kNm]		**Line support**	**Point supp.**	**Point supp. & prestress**	**2D model**
Support	Linear	-11.830	-8.785	-9.053	-14.912
	Geometrically nonlinear	-13.897	-11.456	-11.414	-13.264
Span	Linear	8.544	8.587	8.321	8.696
	Geometrically nonlinear	8.908	8.605	8.438	9.151

In Table 51, the average bending moments that are displayed in Figure 115, Figure 116 and Figure 117 are multiplied by the bridge width of $25\,\mathrm{m}$, to obtain the resulting bending moment over de bridge width. These values can be compared with the results of the two dimensional beam model. The results have the same order of magnitude. Only the bending moments at the support are a little lower for the point shaped supports. When comparing the line supported arch with the point supported arch, transverse load distribution between the piers via beam action is present. Due to the hammock shaped deformation in this region (Figure 121), the material curves only little. Support bending moments in the zone between the support are small, resulting in slightly lower average bending moment in the point supported case. Note that this deflection depends on the applied loading. In this case, the backfill is thicker and thus heavier in the support region.

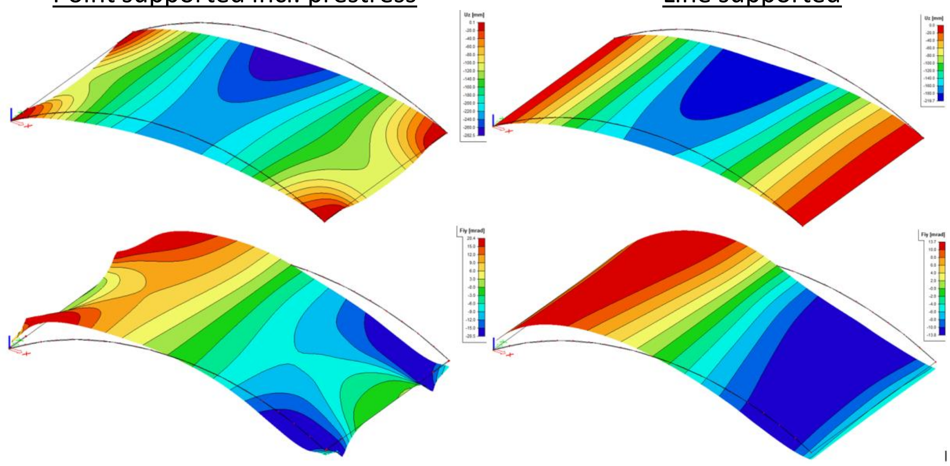

Figure 120: Deformations u_z (upper) and rotations φ_y (lower)

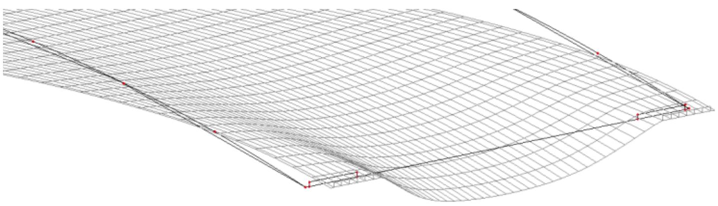

Figure 121: Detail of deformed shape at support

26. Conclusion and recommendation for further research

The research showed that there is only a poor relation between second order bending moment magnification via Euler buckling and the actual geometrically nonlinear behaviour of arches. The better approach for the second order effect is to think of additional bending moments caused by imperfections and by the imaginary second order loading. The additional bending moments due to the second order effect are determined by the deformations and the horizontal thrust.

The amplitude of the geometrical imperfection in the analyses is applied conform eurocode 2. Analysis showed the high sensitivity of arches to imperfections. The amplitude of the imperfection is a fictitious value to use in structural analysis. It incorporates deviations due to execution tolerances and material non-homogeneity. Due to time constraints, the derivation of the formula could not be investigated. However, it has a large influence on bending moments.

Accounting for physical nonlinear behaviour is realistic and beneficial. The stiffness of concrete cross-sections varies depending on the internal forces it is exposed to. Bending moment peaks will lead to cracking. The resulting lower bending stiffness reduces the peak value. In this introducing analysis, the stiffness is applied according to M-N-κ theory in which the initial uncracked stiffness and the lowest elastic stiffness (just before yielding is reached). A full physical nonlinear analysis, including the reinforcement and nonlinear stress-strain relations, will provide more detailed results.

The three dimensional model, including the physical and geometrical nonlinear behaviour, is the best representation of the point supported structure. It can be optimized by modelling the spreading of the tandem axle load through the foamed concrete more accurately. The most accurate and elaborate model will lead to the most detailed results, when modelled well. However, these models require much time. Computational time increases as equilibrium between loading, deformations and stiffnesses has to be found iteratively for each load combination separately. Furthermore, judging the large amount of output data in an elaborate model is time consuming as well.

In practice, modelling all physical mechanisms as detailed as possible is considered with respect to uncertainties like the spread in soil data, accuracy of loads and deviations of material properties. These considerations might lead to the use of far more straightforward models in engineering. Nevertheless, for further research, it is good to know whether the three dimensional, physically and geometrically nonlinear model will lead to lower or higher internal forces compared to the more elementary models.

Literature Part 1

[GeoDR] Internal report: Geotechnical Design Report
number: SN-2.1.1.4-C—TM-RA-2234-A1-1

[Har07] Hartsuijker, C., Welleman, J.W., *Constructiemechanica 3 – Module: Stabiliteit van het evenwicht – Deel 1: Theorie* (lecture notes), Delft University of Technology, Civil Engineering Faculty; 2007

[Tim61] Timoshenko, S.P., Gere, J.M. *Theory of elastic stability.* 2nd edition McGraw-Hill Book Co, Inc.; 1961

[Kar12] Karnovsky, I.A., *Theory of arched structures: Strength, Stability, Vibration.* Springer Science+Business Media, LLC; 2012

[Far92] Farshad, M., *Design and Analysis of Shell Structures,* Kluwer; 1992

[BPe08] Peerdemans, B., *Analysis of thin concrete shells revisited,* MSc report, Delft University of Technology, Civil Engineering Faculty; 2008

[Moo07] Moon, J. et al, *In-plane elastic buckling of pin-ended shallow parabolic arches (article),* Elsevier Ltd, 2007-10

[VisAB] Internal report: “Visualisering ambitie Beeldkwaliteit”
number: SN-PM-2RA-T-0003

Literature Part 2

[Bla10] Blaauwendraad, J., *Plates and FEM – Surprises and pitfalls,* Springer Science+Business Media, 2010

[Bou89] Bouma, A.L., *Mechanica van Constructies, Elasto-statica van slanke structuren,* Delftse Uitgevers maatschappij, Delft; 1989

[Cem73-3] Tuit, A., Suurmond, P., *Voorbeelden van stabiliteitsonderzoek met de computer,* Cement XXV № 3, 1973

[Fer99] Fertis, D.G., *Nonlinear Mechanics, 2nd ed.* CRC Press LLC; 1999

[Har01] Hartsuijker, C., *Toegepaste mechanica, Deel 2 – Spanningen, rekken, vervormingen,* Academic Services, Schoonhoven; 2001

[Har04] Hartsuijker, C., Welleman, J.W., *Toegepaste mechanica, Deel 3 – Statisch onbepaalde constructies en bezwijkanalyse,* Academic Services, Schoonhoven, 2004

[Har07] Hartsuijker, C., Welleman, J.W., *Constructiemechanica 3 – Module: Stabiliteit van het evenwicht – Deel 1: Theorie* (lecture notes), Delft University of Technology, Civil Engineering Faculty; 2007

[Kar12] Karnovsky, I.A., *Theory of arched structures: Strength, Stability, Vibration.* Springer Science+Business Media, LLC; 2012

[Kur08] Kurrer, K-E., *The history of the theory of structures, from arch analysis to computational mechanics,* Ernst & Sohn Verlag für Architectur, Berlin; 2008

[Sci10] Scia Engineer version: 2010.1 – Reference manual and advanced manual

[Sme07] Smet, O. de, *Vorken in bruggen met centrale boogstukken,* paragraph 1.7, MSc Thesis, Gent University, Civil Engineering Faculty, 2006-2007

[Tim61] Timoshenko, S.P., Gere, J.M. *Theory of elastic stability.* 2nd edition McGraw-Hill Book Co, Inc.; 1961

[Wel12] Welleman, J.W., *Notities over kabels en bogen, parametrisch modelleren met MAPLE,* Betonvereniging; 2012

[Yon96] Yong-Lin Pi, N.S. Trahair, *Three dimensional nonlinear analysis of elastic arches*, article: “Engineering Structures”, Vol. 18, No. 1, pp 49-63 , Elsevier Science Ltd; 1996